

UNIVERSITÀ DEGLI STUDI DI NAPOLI
FEDERICO II



Department of Chemical, Materials and
Production Engineering (DICMaPI)

XXXIV Cycle – PhD Program
Industrial Product and Process Engineering

Sorption Enhanced Methanation in fluidized bed reactors

Supervisor:

Prof. Fabrizio Scala

Co-supervisor:

Dr. Antonio Coppola

Candidate:

Fiorella Massa

Acknowledgements

I would like to express my gratitude to those who have guided me along this challenging and inspiring path, being for me the best possible example.

I am grateful to my tutor, Prof. Fabrizio Scala, for believing in me and for his continuous encouragement throughout the PhD program. His in-depth knowledge and expertise, along with his enthusiasm, have always pushed me to be motivated, trying to achieve better and better results.

I would also extend my gratitude to Dr. Antonio Coppola, for his patience, support, and valuable contribution at every stage of this study. His help has been fundamental for the completion of this work.

Abstract

Although fossil resources are the current largest source of natural gas, the production of renewable methane (synthetic or substitute natural gas) is gaining increasing interest due to the efforts made to achieve the energy transition. Methane is a fundamental energy vector that benefits of a well-developed infrastructure and social acceptance worldwide. The pathways for renewable methane production are numerous and, among them, processes also combining carbon-capture and utilization (CCU) techniques are very interesting. This pathway would enable the chemical storage of the surplus of renewable electric energy, providing concurrently the utilization of captured CO₂ as reactant. Although with greatly different purposes, the methanation process is historically consolidated, showing as one of the main drawbacks the complex process control due to the high exothermicity of the reactions. For renewable methane production, being the reactants fed to the process not present in traces like in other established methanation applications, the issue of the temperature control becomes even more sensitive. Therefore, the use of fluidized bed reactors, known to be suitable for large-scale application especially in the case of highly exothermic reactions, is attractive. Lastly, in recent studies the concept of sorption-enhanced reaction has been investigated applied to methanation. In this case, the performance of the process would increase by simultaneously absorbing a methanation product, water vapor. Synthesizing these concepts, in this work, the use of dual interconnected fluidized beds is applied to sorption-enhanced methanation (SEM), achieving a chemical looping system where continuously the hydration and regeneration of a water sorbent takes place. Precisely for this reason, the first part of the experimental campaign concerned the choice of a proper sorbent to perform SEM. In particular, CaO and commercial zeolites were tested. The former gives a chemical absorption in the range of interest, but it can be consumed by the undesired carbonation reaction in an environment containing CO₂. The latter, interested by a physisorption process, can act as a molecular sieve allowing only the water molecules to be captured. CaO showed a lower average asymptotic H₂O capture capacity, being subject to deactivation along the cycles. However, the cost of the material is in favor of CaO. Still, if considering the effect of carbonation, the decrease in the capture capacity was less significant than expected, presenting comparable values of capture capacity for test with both high and low CO₂ concentrations. Further scientific advances towards better performing and less expensive materials appear to be necessary to perform SEM on industrial scale.

Focusing specifically on methanation from renewable H₂ and captured CO₂, the thermodynamics of CO₂ sorption enhanced methanation was analyzed. Calculations involved low pressure levels that are of interest to achieve a decrease of the energy duty for the gas compression work: one of the main reasons why SEM is attractive. The results pointed out that SEM conditions enhance methanation performance at all temperatures and pressures, but they can result in easier carbon generation, that must be avoided to prevent catalyst deactivation. Optimal SEM conditions with stoichiometric feed imply only a partial steam removal: these more flexible operations can be ensured by fluidized bed reactors rather than fixed bed ones. In these latter, in fact, until steam breakthrough from the bed, the whole H₂O produced is captured by the sorbent. This makes the proposed dual interconnected fluidized beds application, a promising concept. Besides the carbon deposition issue, one of the main aspects analyzed in the literature is the suitability of the methanation outlet gas for a direct injection in the natural gas grid. The H₂ concentration resulted to be the critical one whereas limitations regarding the maximum CO and CO₂ content in the gas for grid injection could be reasonably overcome.

CO₂ SEM in the chemical looping configuration was also simulated with Aspen Plus software using calcium oxide as sorbent for the water. Considering again one of the main aspects analyzed by the thermodynamic analysis, the goal was to obtain final synthetic natural gas streams matching the network specifications. To produce such suitable methane streams, the amount of input sorbent was varied for different feed conditions. The analysis showed that the undesired sorbent carbonation has a significant influence on the unconverted amount of hydrogen at the outlet, which increases with the amount of CaO fed. However, it was found that optimal operating conditions in terms of sorbent, using a sub-stoichiometric gas supply with respect to H₂, may lead to obtaining directly injectable streams. Unfortunately, in such conditions the possible carbon generation was not prevented: however, a fluidized bed process may, again, offer a significant advantage ensuring an efficient temperature control and, in such way, limiting the rate of carbon generation.

Finally, real SEM was experimentally tested using the sorbents previously evaluated, in a lab-scale dual interconnected fluidized bed system, providing the proof of concept of the process during methanation/hydration and dehydration cycles at different operating conditions. The chosen catalyst for the reaction was a purposely prepared 10%_wt nickel-based catalyst on alumina support, which showed to be active starting from 250°C, in accordance with literature. A narrow range of temperatures (300-350°C) was investigated, since such range was compatible with the physical and chemical constraints imposed by water adsorption and methanation kinetics. As expected, for the calcium oxide sorbent, CO₂ capture strongly affected the CaO sorbent performance, but with the undesired effect vanishing along the cycles. Therefore, a clear SEM effect occurred in the last cycles, with a sensible increase in the produced CH₄ with respect to traditional methanation. The same qualitative enhanced effect was experienced with the commercial zeolites 3A. This latter confirmed a stable sorption behavior along the cycles, presenting, however, a quantitative enhancement effect on methane productivity lower than CaO. This result highlighted even more the need of further research towards highly active catalytic materials at lower temperatures to aid the adsorption efficiency of performing materials such as zeolites.

List of international journal publications

Coppola, A., Massa, F., Salatino, P., Scala, F., “Fluidized bed CaO hydration-dehydration cycles for application to sorption-enhanced methanation”, *Combustion Science and Technology* 191: 1724–1733 (2019).

Massa, F., Coppola, A., Scala, F., “A thermodynamic study of sorption-enhanced CO₂ methanation at low pressure”, *Journal of CO₂ Utilization* 35: 176-184 (2020).

Coppola, A., Massa, F., Salatino, P., Scala, F., “Evaluation of two sorbents for the sorption-enhanced methanation in a dual fluidized bed system”, *Biomass Conversion and Biorefinery* 11: 111–119 (2021).

Coppola, A., Massa, F., Scala, F., “Simulation of a sorption-enhanced methanation process with CaO in a dual interconnected fluidized bed system”, submitted for publication (2022).

List of conference publications

Massa, F., Coppola, A., Scala, F., “A thermodynamic study of sorption-enhanced CO₂ methanation at low pressure”, Poster presented at Convegno GRICU 2019 “*Il contributo dell’Ingegneria Chimica Italiana alla sostenibilità globale*”, Palermo (2019).

Coppola, A., Massa, F., Salatino, P., Scala, F., “Sorption-enhanced methanation in a dual fluidized bed system: evaluation of two sorbents”, Proc. of 9th European Combustion Meeting, Paper S5_AIII_35, Lisbon, Portugal (2019).

Coppola, A., Esposito, A., Massa, F., Scala, F., Salatino, P., “Fluidized bed sorption-enhanced methanation: a comparison between CaO and zeolite sorbents”, Proc. of 11th Mediterranean Combustion Symposium, Paper CC-06, Tenerife, Spain (2019).

Massa, F., Coppola, A., Scala, F., “Sorption-enhanced CO₂ methanation: a thermodynamic study”, Proc. of 42nd Meeting of the Italian Section of The Combustion Institute, Ravenna, Paper IV7 (2019).

Coppola, A., Massa, F., Salatino, P., Scala, F., “Evaluation of Two Sorbents for the Sorption-Enhanced Methanation in a Dual Fluidized Bed System”, Proc. of ICPS 19 International Conference on Polygeneration Strategies, Vienna, Austria (2019).

Coppola, A., Ferraro, G., Massa, F., Scala, F., “Simulation of fluidized bed sorption-enhanced methanation”, Proc. of 43rd Meeting of the Italian Section of The Combustion Institute, Ischia, Paper V-10 (2021).

Coppola, A., Massa, F., Salatino, P., Scala, F., “Performance of different H₂O sorbents for fluidized bed sorption-enhanced methanation”, Proc. of 13th International Conference on Fluidized Bed Technology (CFB-13), Vancouver, Canada (2021).

Coppola, A., Massa, F., Scala, F., “Sorption-enhanced methanation in a lab-scale twin fluidized bed system”, Proc. of 24th Fluidized Bed Conversion Conference (FBC-24), Göteborg, Sweden (2022).

Coppola, A., Massa, F., Scala, F., “Sorption-enhanced reaction concept applied to CO₂-methanation in a fluidized bed chemical looping system” Proc. of 44th Meeting of the Italian Section of The Combustion Institute, Napoli, Paper II-1 (2022).

Coppola, A., Massa, F., Scala, F., “Simulation of sorption-enhanced methanation in a chemical looping system using CaO as sorbent” Proc. of 44th Meeting of the Italian Section of The Combustion Institute, Napoli, Paper II-4 (2022).

Massa, F., Coppola, A., Scala, F., “Experimental study of sorption-enhanced methanation in a lab-scale fluidized bed system” accepted at Convegno GRICU 2022 “*Centralità dell’ingegneria chimica in un mondo che cambia*”, Ischia (2022).

Massa, F., Coppola, A., Scala, F., “Performance comparison between two sorbents for the sorption-enhanced methanation in a lab-scale twin fluidized bed system”, accepted at 6th International Conference on Chemical Looping, Zaragoza, Spain (2022).

Coppola, A., Massa, F., Scala, F., “Modelling investigation of the sorption enhanced methanation process under chemical looping configuration in fluidized beds” accepted at 6th International Conference on Chemical Looping, Zaragoza, Spain (2022).

Table of Contents

1	Introduction	1
2	State of the art	9
2.1	Synthetic methane production from different pathways	9
2.1.1	SNG from biological pathway	10
2.1.2	Catalytic methanation overview: history, catalysts and kinetics	11
2.2	SNG production processes from coal and biomass	20
2.3	SNG production projects in Power-to-Gas technology	32
2.4	Comparison between economics of the SNG production pathways	33
2.5	CO ₂ methanation in Power-to-Gas chain: concepts involved	34
2.5.1	Energy storage systems	34
2.5.2	Carbon capture and storage and carbon capture and utilization technologies	39
2.5.3	Hydrogen production	47
3	Sorption Enhanced Methanation	52
3.1	Sorption Enhanced concept applied to methanation reactions	52
3.2	SEM as a SNG upgrading process	53
3.3	State of the art of the materials to perform SEM	55
4	CO₂ SEM: Thermodynamic analysis	58
4.1	Thermodynamics of conventional CO ₂ methanation	58
4.2	Present analysis methodology	60
4.3	Results and discussion	64
5	CO₂ SEM: Aspen simulation	73
5.1	CO ₂ SEM using CaO as sorbent: Aspen model	73
5.2	CO ₂ SEM using CaO as sorbent: results	83
6	Experimental investigations: materials, apparatus and procedures	93
6.1	Sorbents evaluated to perform SEM	93

6.2	Catalysts to perform SEM	96
6.3	Twin Beds apparatus	97
6.4	Sorbents testing procedure	100
6.5	SEM experimental procedure	102
7	Twin Beds experimental campaign results	106
7.1	Performance of CaO sorbent hydration	106
7.2	Performance of zeolite sorbent hydration	112
7.3	Traditional methanation	117
7.4	SEM with CaO as sorbent	121
7.5	SEM with zeolite as sorbent	126
8	Conclusions	128
	References	131

1 Introduction

The term “*Global warming*” indicates the long-term heating of the Earth’s climate system observed since the pre-industrial period, at the end of 19th century, due to human activities, primarily fossil fuel combustion, with the consequent expansion of the “greenhouse effect”. The expressions *global warming* and *climate change* are often used without distinction, but, the latter refers to both human and naturally produced warming. Many climate changes, mostly attributed to the change in the amount of solar energy received by the earth due to orbit variations, occurred throughout history: in the last 650000 years there have been seven cycles of glacial advance and retreat. However, around 97% of climate scientists agree that climate-warming trends over the past century are extremely likely due to human activities. The Intergovernmental Panel on Climate Change, an organization of 195 members and a group of more than 100 independent experts from all over the world, under the guidance of the United Nations, concluded that the “scientific evidence for warming of the climate system is unequivocal”. The evidence that solar energy variability is not the leading cause of the current warming, lie in the fact that since 1750, the average amount of energy remained approximately constant and the warming has been observed at the surface and in the lower parts of the atmosphere, while a higher solar energy would cause warmer temperatures in all atmosphere layers. Moreover, all the climate models are unable to reproduce the observed temperature trend if considering exclusively the solar energy changes and leaving aside the rise of greenhouse gases. The IPCC concluded that there is 95% probability that human-produced greenhouse gases are mainly responsible of the observed increase in the earth's temperatures over the past century.

Greenhouse gases are naturally present in relatively low concentrations in the atmosphere with a fundamental task: promoting the passage of solar radiation and hindering the reverse passage of infrared radiation from the earth's surface. The greenhouse effect regulates the earth's temperature and the main gases involved in such natural phenomenon are:

- water vapor, the most abundant greenhouse gas. It acts as a feedback mechanism to the greenhouse effect, increasing with warming, but enhancing clouds and precipitation.
- carbon dioxide, the most important long-lived "forcing" of climate change. It is released both through natural processes and human activities such as deforestation, land use changes, and mostly, combustion of fossil fuels.
- methane: this hydrocarbon gas, from natural sources and human activities, including the decomposition of wastes in landfills, agriculture, and livestock, is on a molecular basis a far more active greenhouse gas than carbon dioxide, but is much less abundant in the atmosphere.
- nitrous oxide, which is a powerful greenhouse gas whose emissions are especially due to the use of fertilizers, fossil fuels and biomass, and the nitric acid production.
- chlorofluorocarbons (CFCs), synthetic compounds of industrial origin whose production is currently largely regulated at international level mainly because they contribute to the destruction of the ozone layer.

The use of fossil fuels such as coal, oil and natural gas, are responsible for 85% of the anthropogenic CO₂ emissions. Humans have increased atmospheric CO₂ concentration by 47% since the Industrial Revolution: atmospheric carbon dioxide levels rose from 280 parts per million to 414 parts per million in the last 150 years. In a 20000 year period the natural increase has been lower. Carbon dioxide levels in the air are the highest in 650000 years [1]. Figure 1.1 shows the CO₂ levels in the last 15 years.

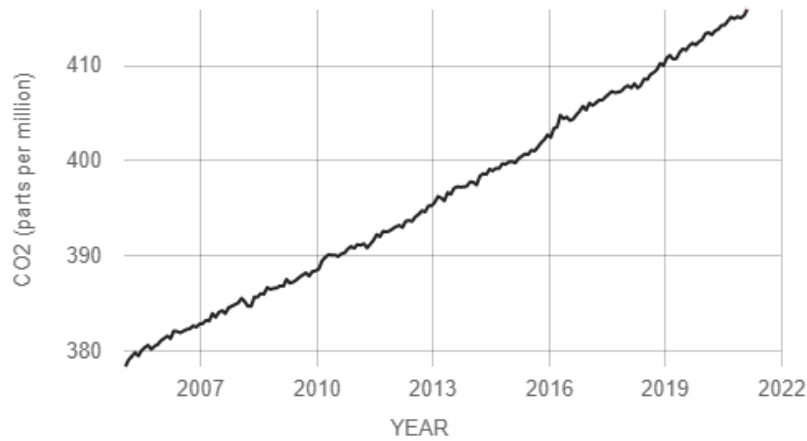


Figure 1.1 CO₂ levels measured at Mauna Loa Observatory, Hawaii [1]

The amount of released carbon dioxide, compared to the total amount of carbon dioxide cyclically emitted and absorbed by nature, represents a small percentage but it can upset the natural balance. Only 50% of annual anthropogenic carbon dioxide emissions are stored naturally, with an inevitable accumulation in the atmosphere. The graphs below show atmospheric CO₂ levels and its levels during the last three glacial cycles, as reconstructed from ice cores (figure 1.2).

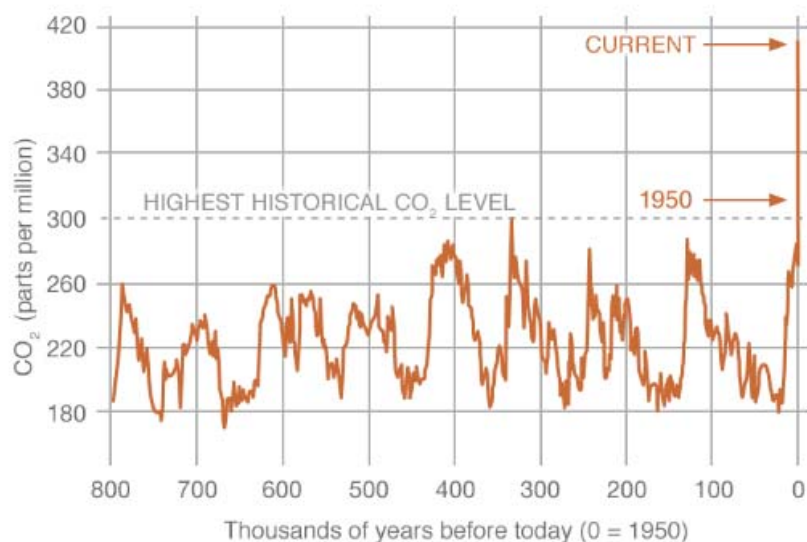


Figure 1.2 CO₂ levels during the last three glacial cycles [1]

Besides CO₂, the concentration of some other greenhouse gases, N₂O and CH₄, shown in figure 1.3, has increased almost exponentially since the industrial revolution.

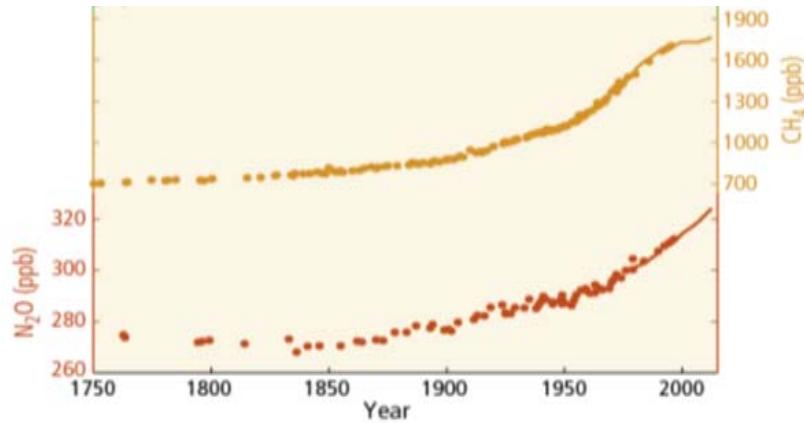


Figure 1.3 N₂O and CH₄ levels during the last 170 years [2]

The commonly used benchmark to measure the global warming is the average increase in planet’s global surface temperature. Since the late 19th century, the earth’s average surface temperature has increased by about 1.18 degrees Celsius, with an increase by 0.2 degrees Celsius per decade, a trend likely due, as already mentioned, to human activity, primarily carbon dioxide emissions, and proceeding at an unprecedented rate. Since 2005, there have been the 10 warmest years in the 141-year record. According to NASA [1], 2016 and 2020 were the warmest years since 1880. The graph of figure 1.4 reports the change in global surface temperature relative to 1951-1980 average temperature: the four different researches give consistent results.

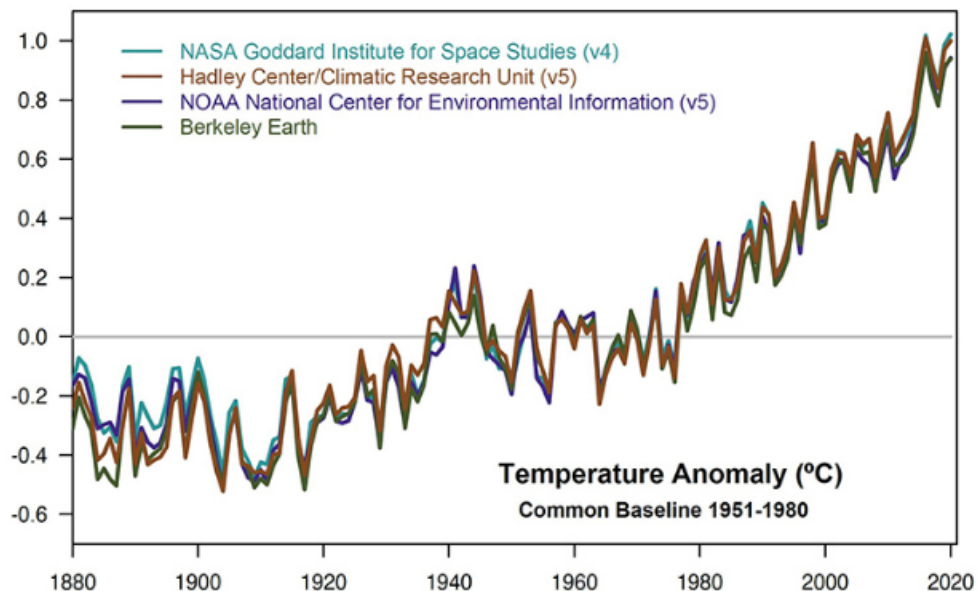


Figure 1.4 Change of global surface temperature [1]

The global temperature rise does not concern only the land: 90% of the extra energy is stored in the oceans, whose top 100 meters showed a warming of more than 0.33 degrees Celsius since 1969. Besides, since the pre-Industrial period, the acidity of the ocean surface has increased by about 30% as result of more carbon dioxide absorbed. Numerous other evidence are manifest: the declining of the extent and thickness of Arctic Sea Ice, the shrinking of the ice sheets, the glacial retreats worldwide. Arctic sea ice in September, when it reaches its minimum, is declining at a rate of 13.1% per decade as reported below (figure 1.5).

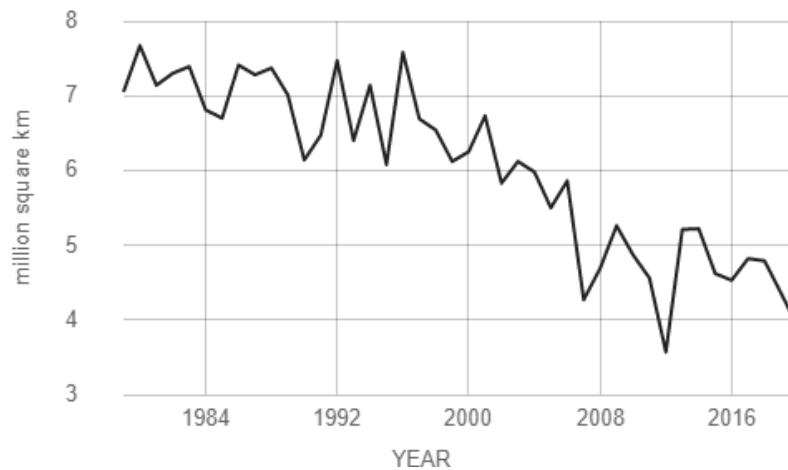


Figure 1.5 Average monthly Arctic sea ice extent each September since 1979 from satellite observations [1]

The land ice sheets in both Antarctica and Greenland have been losing mass since 2002 (figure 1.6).

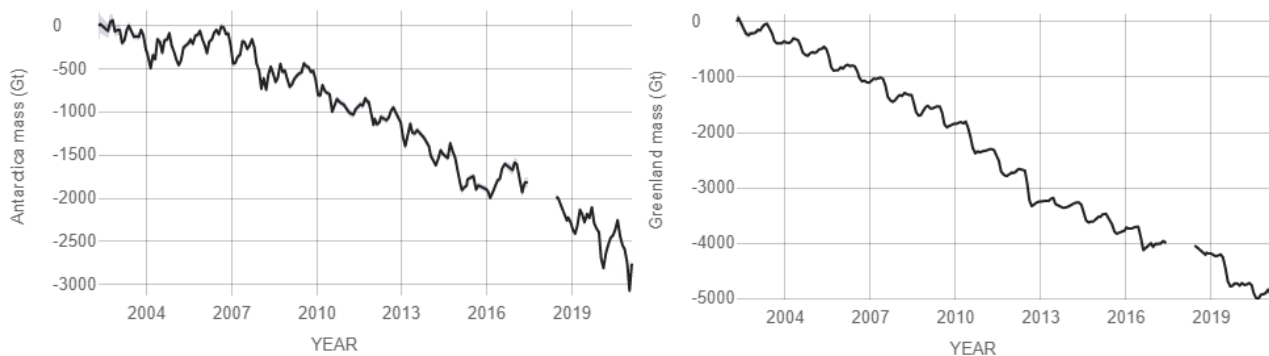


Figure 1.6 Greenland (right chart) and Antarctica (left chart) ice sheets losses: an average of 279 billion tons and 148 billion tons of ice per year between 1993 and 2019, respectively [1]

Global sea level rose about 20 centimeters in the last century, but in the last two decades twice as fast as in the last century. The number of extreme events has been increasing since 1950 all over the world. Scientists have high confidence that these events and effects will continue to increase due to human related GHG emissions: the IPCC forecasts a temperature rise of 1.4 to 5.5 °C over the next century. In particular, climate change is projected to continue over this century and beyond, with a magnitude depending primarily on the amount of heat-trapping gases emitted globally. The change will concern precipitation patterns, climate extremes such as droughts, heat waves, hurricanes and floods that will become more intense and frequent. Global sea level will likely rise 0.3 to 2 meters by 2100 because of water from melting land ice and the expansion of the warming seawater: the Arctic Ocean is projected to be essentially ice free in summer before mid-century. Moreover, the oceans respond slowly to earth's surface warming: seawater will therefore keep warming and sea level will continue to rise for many centuries. The IPCC concludes that the whole range of publications shows "that the net damage costs of climate change are likely to be significant and to increase over time". This theme, one of the most complex issues facing us today, involves science, economics, society, politics and ethical questions. Responding to such an epochal change is urgent: the approaches include mitigation and adaptation strategies. The former is aimed at reducing greenhouse gas emissions by cutting their sources and enhancing all the solutions that may store these gases, such as forests. The adaptation involves reducing vulnerability to the effects of climate change as throughout history people and societies have often done. A variety of plans have been developing, mainly at a local scale, to manage the increasingly extreme events such as, for example, protecting coastlines, land and forests, dealing with water availability and developing resilient crop varieties. However, since the global energy demand will potentially increase by more than 45% by 2030, it is thus necessary to adopt sustainability policies to contain the effects of the ongoing economic development and population growth that are the main causes of the GHG increased emissions. The main sustainability objectives are essentially: increasing energy efficiency, using renewable energy, promoting recycling, and protecting all sort of resources through reuse. At the Paris Climate Conference (COP21) in December 2015, the first legally binding agreement on climate change was adopted: the Paris Agreement counted 190 parties. Governments agreed to keep the global temperature rise below 2°C above pre-industrial levels as a long-term goal and to limit this increase to 1.5°C. In 2020, the involved nations had to submit to UN new targets to reduce global temperature growth by 1.5 degrees Celsius by mid-century: the EU, for example, presented its updated contributions, i.e. reducing emissions by 55% by 2030 compared to 1990 levels. For the European Union, this commitment, defined by 2030, was initially, under the Paris agreement: 40% less emissions, 27% more renewables and 27% more energy efficiency. However, as the UN's analysis shows, the targets set are too weak and even if fulfilled, the global temperature growth could not be kept below 2 degrees Celsius. One hundred sixty-four countries have not submitted any updated plan to achieve by 2030 or 2050 the global warming reduction to within 1.5 degrees Celsius, leading to strong pessimism about the possibility of achieving the objectives set by the Paris Conference. The UN warning is clear and not optimistic: global warming outlook is still above 3 degrees Celsius. In 2019, a growth of 1.1% in global greenhouse gas emissions has been recorded, reaching 52.4 gigatons of CO₂ equivalent excluding those from land-use change, in line with the average annual growth rate of 1.1% since 2012. Figure 1.7 reports these contributions in terms of gigatons of CO₂ equivalent [3].

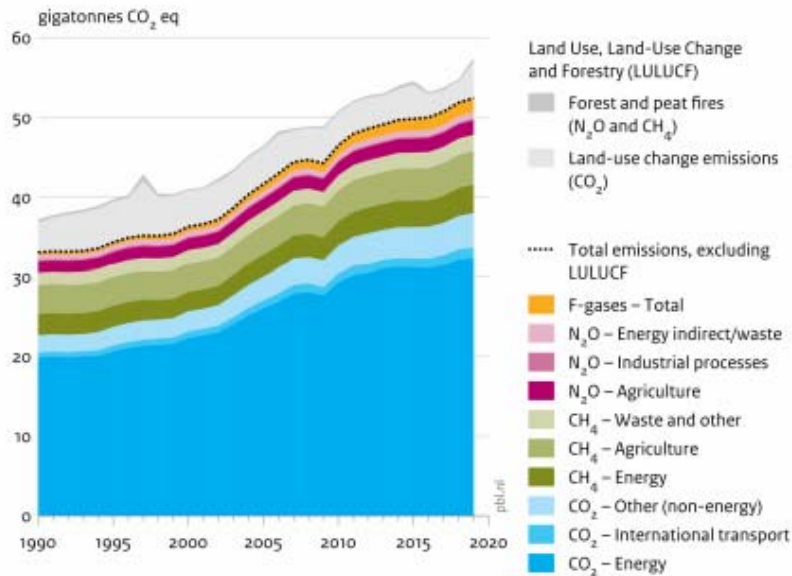


Figure 1.7 Global greenhouse emissions, per type and source, including LULUCF [3]

Other greenhouse gas emissions, CH₄, N₂O and fluorinated gases (F-gases), increased in 2019 by 1.3%, 0.8% and 3.8%, respectively. GHG emissions are distributed as follows: CO₂ about 74%, methane 17%, nitrous oxide 5% and F-gases 3% (see figure 1.8 left). In figure 1.8 (right) it is reported the contribution of the states that mostly are responsible for the global emissions increase since 1970. The six main emitters together account for 62%, three of which decreased their emissions in 2019, namely the European Union, the United States and Japan.

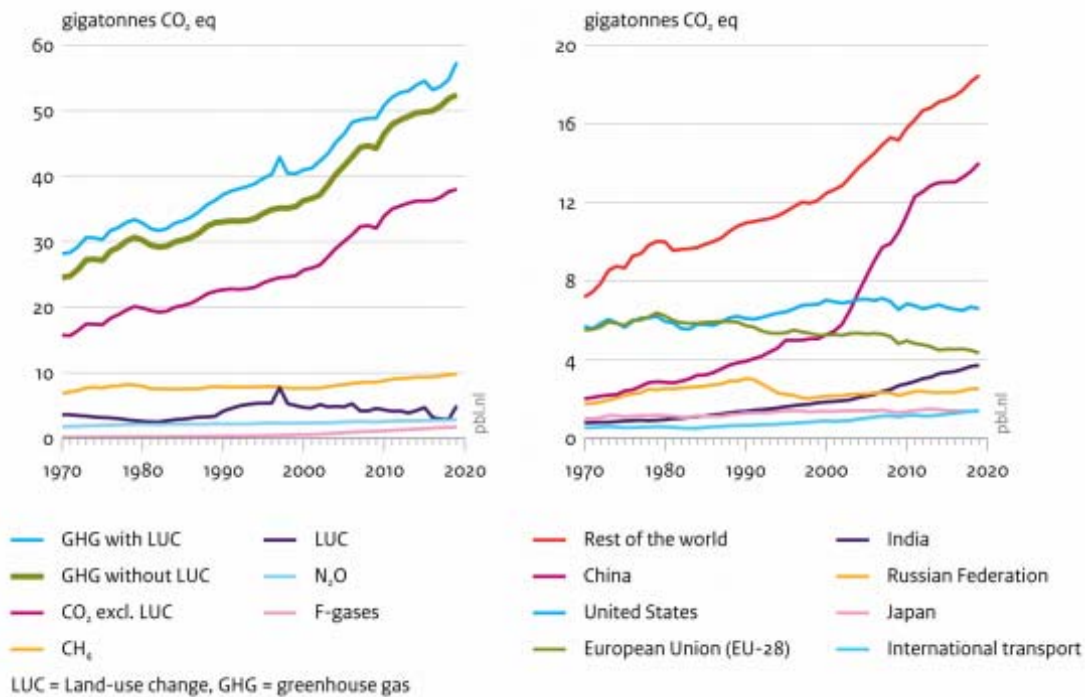


Figure 1.8 Global GHG emissions: per type of gas (left) and top emitting countries and EU (right) [3]

The year 2020 marked the largest-ever decline in global CO₂ emissions (almost 2000 million tons of CO₂) due to the Covid-19 pandemic, but a rapid energy demand resumption suggests that CO₂ emissions will keep increasing significantly in the next future. So that believing that 2019 will mark the definitive peak in global CO₂ emissions is quite risky. However, 2020 offered valuable insights looking ahead: fossil fuels demand, especially oil and coal, dropped, meanwhile, low-carbon technologies, in particular solar PV and wind, reached their highest annual share of the global energy mix of all time. The future of energy demand and emissions in the next years will depend on the efforts that governments will make towards clean energy transition. The International Energy Agency (IEA) Sustainable Recovery report in 2020, provided a pathway to avoid a rebound in emissions, recommending a rapid structural change in how energy is used and produced. Figure 9 reports the projections for total energy-related CO₂ emissions with and without a sustainable recovery [4]. The report from International Renewable Energy Agency showed how countries could effectively strengthen their green energy components: G20 states, responsible for 80% of the global energy-related CO₂ emission reductions needed by 2050, should target an installed renewable capacity of 4.6 TW by 2030.

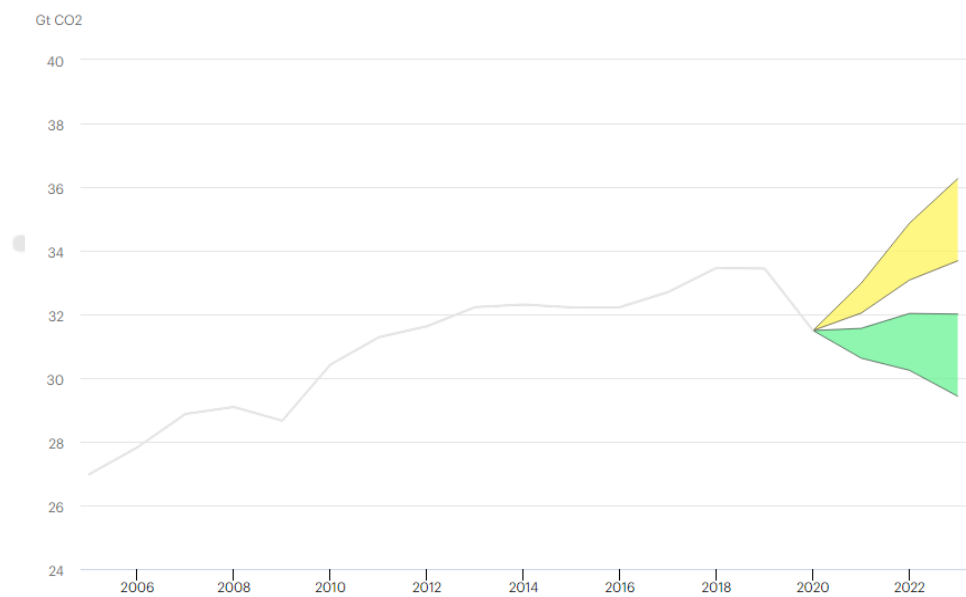


Figure 1.9 Total energy-related CO₂ emissions [4]

The motivation driving this study lies in the concern for climate change and in all the efforts that the scientific community is carrying out in various directions to face this epochal change by means of different technological solutions to achieve a proper paradigm shift. One solution is, clearly, the replacement of fossil energy. Among these sources, natural gas is one of the most versatile and therefore, exploited. It is of interest to study the replacement of natural gas by its synthesized alternative, through renewable sources. Still, as already widely outlined, the reduction of CO₂ emissions is one of the key agendas stated by world leaders and experts in the field, since they are considered the main cause of this global alteration. The direct reduction of the emissions appears to be challenging in the short term, due to the established industrial technologies, based mainly on fossil fuels exploitation. The concepts of Carbon Capture have emerged as an attractive suggestion. Among the different technologies, both the storage and the utilization of CO₂ have been proposed. The latter would even enable to obtain a benefit using CO₂. The renewable synthetic natural gas production, also in the framework of Carbon Capture and Utilization (CCU) techniques, is the key concept around which this work is developed.

2 State of the art

2.1 Synthetic methane production from different pathways

Generally, the process of synthetic methane production (methanation) can proceed via two different routes:

- biological, involving low temperatures (<70 °C) and stirred tank reactors;
- catalytic, exploiting thermochemical processes at temperatures above 250°C.

Moreover, the catalytic pathway includes two main groups of processes:

- methanation from coal or biomass using CO or CO/CO₂ mixtures of raw or conditioned syngas containing carbon oxides and hydrogen deriving from gasification;
- methanation in the framework of Power-to-Gas technologies that convert the surplus of renewable electric energy into a grid-compatible gaseous fuel.

In particular, two different options belong to the Power-to-Gas technology:

- methanation of CO₂, using hydrogen from water electrolysis and CO₂ present in biogas from digestion of organic feedstock (biogas upgrading);
- methanation of CO₂ with hydrogen obtained by water electrolysis and waste (pure) CO₂ streams captured from power plant flue gas or from other industrial processes (Carbon Capture and Utilization-CCU).

Figures 2.5 and 2.6 report the plant setup for synthetic natural gas (SNG) production given the two main sources: biomass/coal or CO₂ in the PtG.

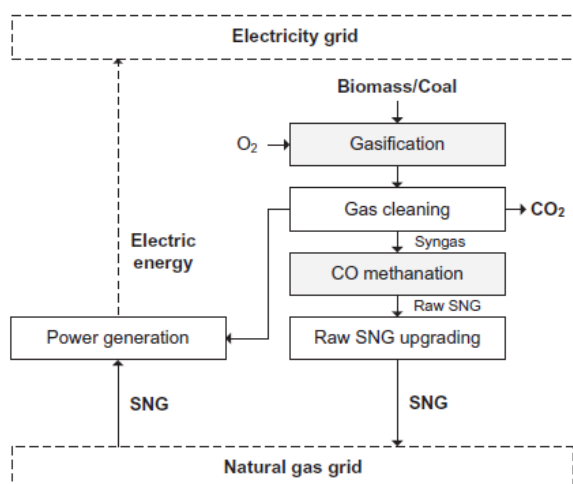


Figure 2.5 Biomass/coal-to-SNG plant setup [5]

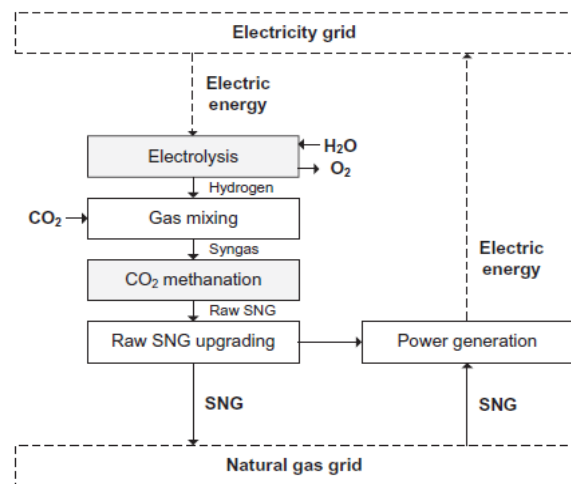


Figure 2.6 PtG plant setup with CO₂ methanation [5]

2.1.1 SNG from biological pathway

Considering the biological pathway, the main steps from wet biomass to SNG are fermentation, raw biogas upgrading, including CO₂ and water removal, and final grid injection. The biogas contains about 50-75% methane together with a fraction of carbon dioxide, which is separated so that the resulting gas can be fed into the natural gas grid. This is a well consolidated technology (back to around 1919) with a first plant built only in 2006, in Germany, where still nowadays almost the totality of plants is located.

Anaerobic digestion by means of microorganisms in an oxygen-free atmosphere, leading to the formation of raw-biogas and a solid residue, is made of four key steps: hydrolysis, acidogenesis, acetogenesis, and methanogenesis. The overall simplified reaction could be indicated as:



Since the feedstock is widely heterogeneous, very different gas compositions can be obtained. Numerous parameters such as pH, temperature, retention times, affect the results and also the chosen configurations are multiple but, generally, the digesters are mesophilic and multi-stage (at least two vessels). After fermentation, water is condensed, and an adsorption process is used when fine removal is required. In the digester, H₂S can be oxidated by microorganisms or iron chloride can be added to form FeS removable particles. However, generally, downstream removal is applied: adsorption, membrane separation and biological filtration are, essentially, the options. As for CO₂, the percentage allowed in the SNG is typically in the range 1-3%. CO₂ separation is achieved basically by the means of three methods: pressurized water scrubbing (PWS), chemical scrubbing and pressure swing adsorption (PSA). PWS works at 10-20 bar using a packed counter-flow column at the bottom of which water with dissolved gas is stripped and recycled. This method allows efficiencies around 97% and CH₄ losses below 2%; to obtain higher performance the chemical absorption is carried out using polyethylene glycol or amines as sorbents. PSA techniques use molecular sieves to perform reversible adsorption followed by regeneration at a lower pressure level. The impurities in these processes are removed upstream to prevent irreversible deactivation of the sieve. These latter techniques present high efficiencies (<99%) and low CH₄ losses (<1.5%). Lastly, polymeric membranes are recently intensively studied to separate selectively different fractions of materials using pressures up to 36 bar. A multitude of equipment and facilities need to be considered for grid injection: storage tanks, connecting pipes, controllers. The pressure levels vary due to the kind of distribution, from 0.1 to 16 bar.

Figure 2.7 schematizes the biological process.

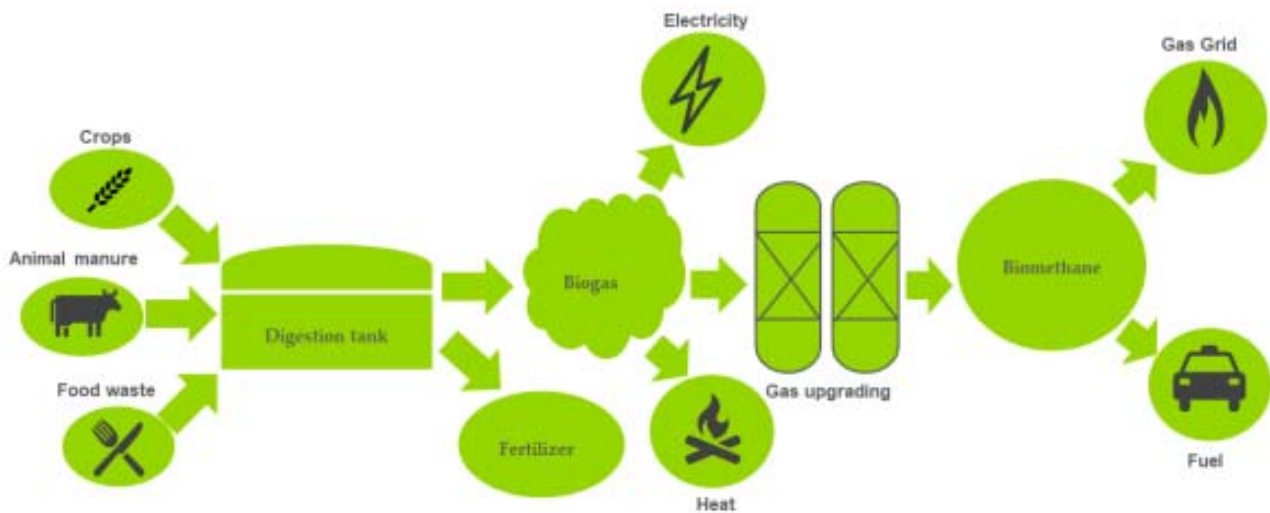
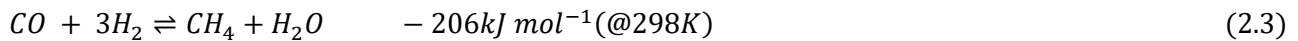
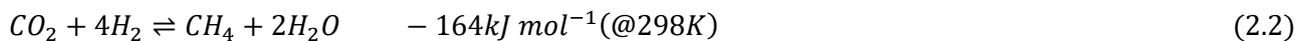


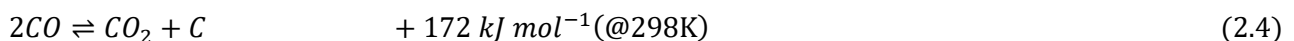
Figure 2.7 Schematic overview of the anaerobic digestion process [6]

2.1.2 Catalytic methanation overview: history, catalysts, and kinetics

Catalytic methanation was discovered by Sabatier and Senderens in 1902 [7] as a reaction path occurring exothermically with a net reduction of gaseous moles:



The process is therefore a well-established technology with traditional commercial methanation applications typically found in ammonia synthesis plants to remove carbon monoxide. These solutions rely generally on a cascade of adiabatic catalytic fixed bed reactors operated at temperatures between 250 and 600°C with intermediate cooling steps and recycles, and at high operational pressure [8]. Among the typical metals that catalyze methanation (Ru, Ni, Co, Fe, and Mo), Ni is the most used for commercial application based on cost-related considerations [8]. It should be underlined, however, that the commercial catalyst choice is a sensitive issue: these materials are subject to different chemical, thermal and mechanical deactivation mechanisms [9]. For example, the main chemical deactivation of commercial Ni-based catalysts is represented by carbon (coke) deposition on the catalyst surface [10], this phenomenon essentially derives by the Boudouard reaction:

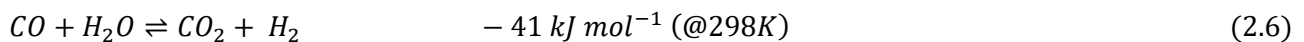
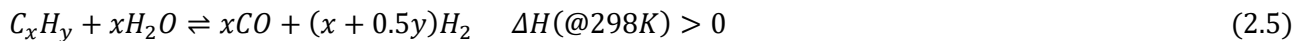


Apart from the original methanation application (the removal of CO from syngas in ammonia production plants), studies for the innovative synthetic natural gas (SNG) production started in the US in the 1960s. These studies involved coal conversion because the so-called “golden age” in natural gas use, led industry and government to concern of a possible shortage due to the increasing demand. Then, in the late 1970s, during the oil crisis, the idea of synthesizing methane by CO methanation following coal gasification received attention again: United States, Germany and Great Britain were

mainly involved. Eventually, only one commercial SNG plant was built: the Great Plains Synfuels Plant by the Dakota Gasification Company (North Dakota, United States) [11].

This kind of proposed technologies rely on the gasification of the solid carbon source with steam and/or oxygen and the subsequent methanation of a mixture, whose cleaning and conditioning are crucial and sensitive processes to achieve a suitable composition.

The product gas mixture contains H_2 , CO , CO_2 , H_2O , CH_4 , some higher hydrocarbons and catalyst poisons such as sulphur and chlorine species. The most common conditioning steps are steam reforming and water gas shift reaction as shown below:



Water gas shift reaction increases the H_2/CO ratio (usually between 0.3 and 2 at the gasifier outlet) in order to improve CO conversion and catalyst lifetime.

On the other hand, studies on CO_2 methanation started in the 1980s with the aim of using coke oven gas or blast furnace gas for downstream methanation. The studies to apply these concepts on a commercial scale were discontinued essentially due to the efforts required for the cleaning processes of these gases. Research resumed with the growing concern about the anthropogenic greenhouse gas emissions. In the 1980-1990s Hashimoto et al. [12] suggested electrolysis of seawater and methanation, for recycling of CO_2 . Over the last 20 years CO_2 methanation processes research, carried out by institutions and industry, has increased, pushed by the rising environmental consciousness and the growth of demand for renewable electricity storage. The same reasons have led to develop novel concepts to produce renewable methane from biomass through CO methanation [11]. Figure 2.8 gives an overview of synthetic natural gas studies.

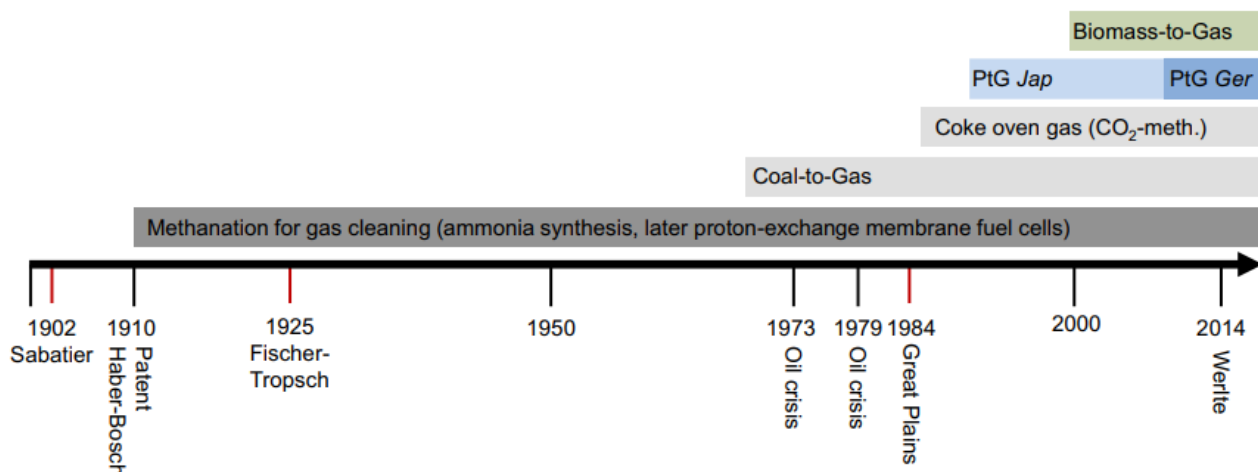


Figure 2.8 History of methanation (abbreviations: Jap-Japan, Ger-Germany) [5]

As for the catalytic methanation, active phase, supports, promoters and preparation conditions of the catalytic materials influence the activity and the yield of the whole process. Metals in groups 8-10 of the periodic table are active for these reactions with this order of activity and selectivity to CH₄ [8]:

Activity: Ru > Fe > Ni > Co > Mo

Selectivity: Ni > Co > Fe > Ru

Ruthenium is about 120 times more expensive than Ni, hence it is not used for industrial-scale production, however this metal must be chosen for low temperature processes. Nickel is the most selective catalyst with a good activity and a quite low price: for these reasons, as already mentioned, it is the most applied for commercial methanation. Iron catalysts have a good reactivity but better selectivity towards hydrocarbons with higher molecular weight than methane, in fact, they are used in the Fischer-Tropsch process [13]. Lastly, molybdenum has the lowest activity among the methanation catalysts and a high selectivity towards C₂₊ hydrocarbons [14]: however, it exhibits the highest sulfur tolerance [8].

Although there are also unsupported catalysts, generally oxides with large surface area are applied as supports, e.g. Al₂O₃ (alumina), SiO₂ (silica), or TiO₂ (titania).

Considering the mostly used Ni/Al₂O₃ catalysts, different promoters can improve methanation: MgO, V₂O₃, La₂O₃, CeO₂. V₂O₃ is used to improve activity, thermal stability, and coke resistance, MgO also increases carbon resistance and thermal stability. La₂O₃ is found to increase Ni dispersion and H₂ uptake while CeO₂ can be used to dope Ni/Al₂O₃ catalysts to obtain a higher reducibility and long-term stability [15-17]. Among the possible negative effects of additional materials, potassium is found to increase the selectivity of Ni towards higher hydrocarbons. All the methanation catalysts have to be reduced from the oxidized to the metallic form before their application: the reduction process usually takes place in hydrogen atmosphere and temperature in the range 300-600 °C. Considering in particular Ni/Al₂O₃ catalysts, low reduction temperatures favor the formation of higher hydrocarbons in subsequent applications, however, a high reduction temperature, although determines a higher selectivity towards methane, may cause sintering of metal particles and deactivation of the catalyst [18].

The deactivation of nickel-based methanation catalysts can be a chemical, thermal or mechanical deactivation [9]. Methanation catalysts can react with numerous impurities as sulphur and chlorine compounds, tars, particles, ammonia, alkalis. Plants operating with syngas or carbon dioxide streams from anaerobic biogas production need sulfur removal systems: nickel requires sulfur contents in the range of several parts per billion. These systems mainly consist of low-temperature methanol washing and adsorption with zinc oxide. Sulfur poisoning reaction involves hydrogen sulfide and nickel oxide going to nickel sulfide and water. Other important vapor-solid reactions deactivating the nickel catalysts are due to solid nickel entering the vapor phase by forming nickel tetracarbonyl, at temperatures below 230 °C. In any case, these temperatures are avoided during operation (excluding start-up and shutdown) due to the low activity of commercial catalysts below 250 °C. The main issue for methanation with regard to chemical deactivation is, as mentioned before, the carbon formation and deposition: steam is often added, or H₂/CO ratio increased in commercial applications to inhibit the fouling of catalyst.

Thermal deactivation is a problem especially in adiabatic fixed bed methanation reactors due to their high temperature hot spots: temperatures above 500 °C have to be avoided because of nickel sintering

which leads to a loss of surface area. However, catalysts for high temperature methanation (600-700 °C) have been developed and are available on the market.

Regarding the mechanical deactivation, thermal stresses or pressure fluctuations can lead to the crushing of particles: the reactors more subject to these phenomena are moving-beds, fluidized-beds and slurry-beds where the attrition of active material causes increased costs for make-up of catalysts and the removal of the abraded catalyst to protect the equipment.

Most of the kinetic studies have been carried out on CO methanation, only few studies have proposed rate expressions for the methanation of CO₂ [19]. Besides, it does not exist only one accepted kinetic model in literature. Simple power law models describe the reaction without the assumption of a rate-determining step: this approach is not suitable to describe widely different conditions, though. To better describe different ranges, the more complex Langmuir–Hinshelwood–Hougen–Watson models, with many kinetic parameters such as rate and adsorption constants for all reactions and all species, are often applied. In general, literature sources suggest for methanation mechanisms involving the formation of surface carbon instead of adsorbed oxygenated species (e.g. CHO, HCOH and HCOO⁻) as reaction intermediates. Surface carbon is typically generated on industrial catalyst, reacting very slowly with hydrogen [20]. The first hydrogenation (formation of a C-H bond) seems to be slower than the hydrogenation of CH_i species: this first step might be the rate-determining step at temperatures <300°C while CO dissociation could be the RDS for higher temperatures [21]. The detailed state of art of the CO₂ and CO methanation kinetics is discussed below. Xu and Froment [22] published the most influential work examining specifically steam-methane reforming, CO/CO₂ methanation and water-gas shift kinetics. The authors used a catalyst containing 15.2% nickel supported on magnesium spinel. The reference conditions for the reverse water-gas shift and methanation were T = 673 K, p = 3 bar, H₂/CO₂ molar ratio = 1, W/F⁰_{CO₂}=0.25 g_{cat}/mol_{CO₂}. Experiments were carried out with different catalyst sizes: there were no significant internal diffusion limitations for the size 0.17-0.25 mm. It was also shown that external mass and heat transfer resistances were negligible. Among all the possible reactions that may occur during methanation and reverse water-gas shift, a thermodynamic analysis allowed to identify the reactions sufficient to describe the entire process. Three main reactions were considered: CO methanation, reverse water gas shift and CO₂ methanation; the corresponding three reaction rates found are:

$$r_{COMeth} = \frac{k_{CO} \left(\frac{p_{H_2}^{0.5} p_{CO}}{K_1} - p_{CH_4} p_{H_2O} p_{H_2}^{-2.5} \right)}{\left(1 + K_{CO} p_{CO} + K_{CH_4} p_{CH_4} + K_{H_2} p_{H_2} + K_{H_2O} p_{H_2O} p_{H_2}^{-1} \right)^2} \quad \left[\frac{kmol}{kg_{cat}h} \right] \quad (2.7)$$

$$r_{RWGS} = \frac{k_{RWGS} \left(\frac{p_{CO_2}}{K_2} - p_{CO} p_{H_2O} \right)}{\left(1 + K_{CO} p_{CO} + K_{CH_4} p_{CH_4} + K_{H_2} p_{H_2} + K_{H_2O} p_{H_2O} p_{H_2}^{-1} \right)^2} \quad \left[\frac{kmol}{kg_{cat}h} \right] \quad (2.8)$$

$$r_{CO_2Meth} = \frac{k_{CO_2} \left(\frac{p_{H_2}^{0.5} p_{CO_2}}{K_3} - p_{CH_4} p_{H_2O}^2 p_{H_2}^{-3.5} \right)}{\left(1 + K_{CO} p_{CO} + K_{CH_4} p_{CH_4} + K_{H_2} p_{H_2} + K_{H_2O} p_{H_2O} p_{H_2}^{-1} \right)^2} \quad \left[\frac{kmol}{kg_{cat}h} \right] \quad (2.9)$$

In the equations (2.7), (2.8) and (2.9):

$$k_i = k_{0i} \exp \left[-\frac{E_i}{R} \left(\frac{1}{T} - \frac{1}{T_r} \right) \right] \quad i = CO, RWGS, CO_2 \quad T_r = 648K \quad (2.10)$$

$$K_j = K_{0j} \exp \left[-\frac{\Delta H_j}{R} \left(\frac{1}{T} - \frac{1}{T_r} \right) \right] \quad j = CO, H_2, H_2O, CH_4 \quad T_r = 648K(CO, H_2), 823K(H_2O, CH_4) \quad (2.11)$$

K_1 [bar^2], K_2 [bar^2] and K_3 [] are the equilibrium constants of the reverse reactions.

The parameters are reported in table 2.1 and 2.2.

k_{0CO} [$\frac{\text{kmolbar}^{0.5}}{\text{kg}_{cat}h}$]	k_{0RWGS} [$\frac{\text{kmol}}{\text{kg}_{cat}hbar}$]	k_{0CO_2} [$\frac{\text{kmolbar}^{0.5}}{\text{kg}_{cat}h}$]	K_{0CO} [bar^{-1}]	K_{0H_2} [bar^{-1}]	K_{0H_2O} []	K_{0CH_4} [bar^{-1}]
4.225 10^{15}	1.955 10^6	1.02 10^{15}	8.23 10^{-5}	6.19 10^{-9}	1.77 10^5	6.65 10^{-4}

Table 2.1 Preexponential factors of the Xu and Froment model

E_{CO}	E_{RWGS}	E_{CO_2}	ΔH_{CO} (KJ/mol)	ΔH_{H_2}	ΔH_{H_2O}	ΔH_{CH_4}
240.1	67.13	243.9	-70.65	-82.9	88.68	38.28

Table 2.2 Parameter estimates of the Xu and Froment model

Regarding CO methanation, specifically, the following pictures (figure 2.9 and 2.10) summarize the reaction pathways for two different theories proposed in the literature (the associative and dissociative mechanism), with possible rate-determining steps (RDS) and reported in the work of Kopyscinsky [23]. Most of the experimental setups are made of flow reactors with or without gas recycle. Two different methods are used to avoid an uncontrolled temperature increase during experiments due to the exothermicity of the reaction: differential reactors or highly diluted catalyst beds and gas mixtures (>90% inert gas). In literature, in the experiments the exit gas composition was measured; Kopyscinsky [23] applied spatially resolved measurements of gas concentrations and temperature to gather more detailed information along the axis of a catalytic plate reactor. They used a Ni-alumina commercial catalyst, (50%_{wt} Ni/Al₂O₃, BET = 183 m²/g).

H_2	$+ 2^*$	$\leftrightarrow 2H^*$		dissociative adsorption of H_2
CO	$+ ^*$	$\leftrightarrow CO^*$	RDS	CO – adsorption
CO^*	$+ H^*$	$\leftrightarrow COH^*$	$+ ^*$	RDS COH – formation
COH^*	$+ ^*$	$\leftrightarrow CH^*$	$+ O^*$	RDS dissociation of COH complex
COH^*	$+ ^*$	$\leftrightarrow C^*$	$+ OH^*$	RDS dissociation of COH complex
COH^*	$+ H^*$	$\leftrightarrow COH_2^*$	$+ ^*$	RDS COH_2 – formation
COH^*	$+ H^*$	$\leftrightarrow CH^*$	$+ OH^*$	RDS dissociation of COH with H
COH_2^*	$+ H^*$	$\leftrightarrow CH^*$	$+ H_2O^*$	RDS dissociation of COH_2 with H
COH_2^*	$+ H^*$	$\leftrightarrow COH_3^*$	$+ ^*$	RDS COH_3 – formation
COH_3^*	$+ H^*$	$\leftrightarrow CH_2^*$	$+ H_2O^*$	RDS dissociation of COH_3 with H
CO^*	$+ OH^*$	$\leftrightarrow CO_2^*$	$+ H^*$	CO_2 – formation
CO^*	$+ H_2O^*$	$\leftrightarrow CO_2^*$	$+ 2H^*$	CO_2 – formation
CO_2^*		$\leftrightarrow CO_2$	$+ ^*$	CO_2 – desorption
O^*	$+ H^*$	$\leftrightarrow OH^*$	$+ ^*$	OH – formation
OH^*	$+ H^*$	$\leftrightarrow H_2O^*$	$+ ^*$	H_2O – formation
H_2O^*		$\leftrightarrow H_2O$	$+ ^*$	H_2O – desorption
C^*	$+ H^*$	$\leftrightarrow CH^*$	$+ ^*$	RDS hydrogenation of C
CH^*	$+ H^*$	$\leftrightarrow CH_2^*$	$+ ^*$	RDS hydrogenation of CH
CH_2^*	$+ H^*$	$\leftrightarrow CH_3^*$	$+ ^*$	RDS hydrogenation of CH_2
CH_3^*	$+ H^*$	$\leftrightarrow CH_4^*$	$+ ^*$	hydrogenation of CH_3
CH_4^*		$\leftrightarrow CH_4$	$+ ^*$	CH_4 – desorption

* empty active site
 C^* adsorbed species (e.g., adsorbed carbon)
RDS rate-determining step (proposed RDS from the literature)

Figure 2.9 Reaction pathways for dissociative mechanism [23]

H_2	$+ 2^*$	$\leftrightarrow 2H^*$		dissociative adsorption of H_2
CO	$+ ^*$	$\leftrightarrow CO^*$	RDS	CO – adsorption
CO^*	$+ ^*$	$\leftrightarrow C^*$	$+ O^*$	RDS dissociation of CO
C^*	$+ H^*$	$\leftrightarrow CH^*$	$+ ^*$	RDS hydrogenation of C
CH^*	$+ H^*$	$\leftrightarrow CH_2^*$	$+ ^*$	RDS hydrogenation of CH
CH_2^*	$+ H^*$	$\leftrightarrow CH_3^*$	$+ ^*$	RDS hydrogenation of CH_2
CH_3^*	$+ H^*$	$\leftrightarrow CH_4^*$	$+ ^*$	hydrogenation of CH_3
CH_4^*		$\leftrightarrow CH_4$	$+ ^*$	CH_4 – desorption
CO^*	$+ O^*$	$\leftrightarrow CO_2$	$+ ^*$	CO_2 – formation
CO_2^*		$\leftrightarrow CO_2$	$+ ^*$	CO_2 – desorption
O^*	$+ H^*$	$\leftrightarrow OH^*$	$+ ^*$	OH – formation
OH^*	$+ H^*$	$\leftrightarrow H_2O^*$	$+ ^*$	H_2O – formation
H_2O^*		$\leftrightarrow H_2O$	$+ ^*$	H_2O – desorption
CO^*	$+ OH^*$	$\leftrightarrow CO_2^*$	$+ H^*$	CO_2 – formation via OH
CO^*	$+ H_2O^*$	$\leftrightarrow CO_2^*$	$+ 2H^*$	CO_2 – formation via H_2O

* empty active site
 C^* adsorbed species (e.g., adsorbed carbon)
RDS rate-determining step (proposed RDS from the literature)

Figure 2.10 Reaction pathways for associative mechanism [23]

As for the dissociative mechanism proposed, CO would present a stronger adsorption compared to H₂ so that CO is thought to dissociate to C* and O* at first and then react with H*. Considering the other mechanism, the associative one, COH_x intermediate would be present because adsorbed CO reacts with hydrogen to give a COH_x complex, which has a lower activation barrier energy for the C-O bond dissociation. COH_x intermediate can either dissociate or react to CH_y: x, y and their values depend strongly on the experimental conditions and nature of the catalyst. The kinetic parameters estimation was performed by Kopyscinski developing a one-dimensional reactor model including a generalized Langmuir-Hinshelwood rate expression. The models developed depend on the RDS considered and hydrogen, carbon monoxide, water or hydroxyl and an intermediate carbon species (C*, CH_x*, or COH_x*) are the species assumed to be adsorbed on the surface. Three kinetic approaches, considering the dissociative mechanism, fit the data equally well. The equations derived are presented below with the related RDS. All these models considered OH instead of H₂O as adsorbed species and are reported below as Model 1, 2 and 3. All these models assume as RDS the reaction of the surface carbon species C*, CH* or COH* with an adsorbed hydrogen H* and an adsorbed hydroxyl species OH*. Experiments indicated that, considering methanation, H₂O inhibits the reaction rate whereas CH₄ and CO₂ do not show this effect. In the rate equation for the methanation, the reverse reaction can be neglected (equilibrium strongly shifted towards the products below 380 °C, K_{pMeth} = 7.8·10⁷ bar⁻² at 280°C and 5.6·10⁴ bar⁻² at 380°C). Methanation and water gas shift are thought to take place on the same sites so that the denominator of the rate equations is the same. The activation energy of the methanation reaction for Model 2 is 74 kJ·mol⁻¹: this value is consistent with others reported in the literature determined under similar conditions. The parameters of the three models are reported in table 2.3.

$$r_{COMeth} = \frac{k_1 K_C p_{CO}^{0.5} p_{H_2}^{0.5}}{(1 + K_C p_{CO} + K_{OH} p_{H_2O} p_{H_2}^{-0.5})^2} \quad \text{Model 1 RDS } (C^* + H^* \leftrightarrow CH^* + *) \quad (2.12)$$

$$r_{WGS} = \frac{k_2 (K_a p_{CO} p_{H_2O} - p_{H_2} p_{CO_2} / K_{eq})}{p_{H_2}^{0.5} (1 + K_C p_{CO} + K_{OH} p_{H_2O} p_{H_2}^{-0.5})^2} \quad (2.13)$$

$$r_{COMeth} = \frac{k_1 K_{CH} p_{CO}^{0.5} p_{H_2}}{(1 + K_{CH} p_{CO}^{0.5} p_{H_2}^{0.5} + K_{OH} p_{H_2O} p_{H_2}^{-0.5})^2} \quad \text{Model 2 RDS } (CH^* + H^* \leftrightarrow CH_2^* + *) \quad (2.14)$$

$$r_{WGS} = \frac{k_2 (K_a p_{CO} p_{H_2O} - p_{H_2} p_{CO_2} / K_{eq})}{p_{H_2}^{0.5} (1 + K_{CH} p_{CO}^{0.5} p_{H_2}^{0.5} + K_{OH} p_{H_2O} p_{H_2}^{-0.5})^2} \quad (2.15)$$

$$r_{COMeth} = \frac{k_1 K_{COH} p_{CO} p_{H_2}}{(1 + K_{COH} p_{CO} p_{H_2}^{0.5} + K_{OH} p_{H_2O} p_{H_2}^{-0.5})^2} \quad \text{Model 3 RDS } (COH^* + H^* \leftrightarrow CH^* + OH^*) \quad (2.16)$$

$$r_{WGS} = \frac{k_2 (K_a p_{CO} p_{H_2O} - p_{H_2} p_{CO_2} / K_{eq})}{p_{H_2}^{0.5} (1 + K_{COH} p_{CO} p_{H_2}^{0.5} + K_{OH} p_{H_2O} p_{H_2}^{-0.5})^2} \quad (2.17)$$

	Model 1	Model 2	Model 3
$\ln k_1(T_{ref})$	0.15	0.08	0.042
$\ln K_{OH}(T_{ref})$	-0.41	-0.40	-0.53
$\ln K_C(T_{ref})$	0.57	-	-
$\ln K_{CH}(T_{ref})$	-	0.93	-
$\ln K_{COH}(T_{ref})$	-	-	2.58
$\ln k_2(T_{ref})$	2	2.12	2.46
$E_{A1}/(RT_{ref})$	14.9	12.7	11.8
$\Delta H_{OH}/(RT_{ref})$	-14.6	-17.6	-19.8
$\Delta H_C/(RT_{ref})$	-12.3	-	-
$\Delta H_{CH}/(RT_{ref})$	-	-10.2	-
$\Delta H_{COH}/(RT_{ref})$	-	-	1.3
$E_{A2}/(RT_{ref})$	32.5	31.3	33
$\ln K_a(T_{ref})$	-1.07	-1.02	-1.04
$\Delta H_a/(RT_{ref})$	-1.3	-0.35	3

Table 2.3 Parameters of the Kopyscinsky models

As for CO₂ methanation instead, since methane is produced during Fisher-Tropsch synthesis, some experiments have been performed using mainly Co and Fe catalysts, as a result of the study of this process applied to convert CO₂ to long chain paraffins or olefins [24]. Ru and Rh based catalysts have also been studied during CO₂ methanation: the former due to the high reactivity and selectivity [25], the latter because of the ability to catalyze methanation at very low temperatures (below 100 °C) [26]. Clearly, though, Nickel is the most widely studied material: Gao et al. [27] reviewed the whole subject. Two mechanisms are mainly proposed for the methanation of CO₂ on Nickel based catalysts: the most popular scheme considers the dissociative adsorption of CO₂ to form CO and O on the surface of the catalyst. The second path includes the conversion of CO₂ to methane via carbonate or formate intermediates, which does not involve CO [28] (fig. 2.11).

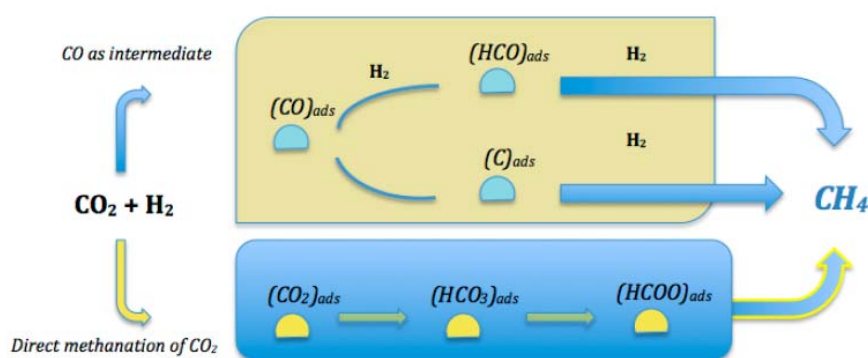


Figure 2.11 Simplified reaction mechanisms of CO₂ methanation [28]

The reaction pathway seems to depend on the nature of the support so that rate expressions may vary for different catalysts, with important implications in reactor operation and design.

Several types of supported nickel catalysts have been used and characterized to study CO₂ methanation but only a few works have analyzed rigorous kinetic aspects at different temperatures, overall and partial pressures.

Considering CO₂ methanation over nickel, it is generically reported that small amounts of CO may suppress CO₂ methanation as the Ni surface is preferably covered by CO rather than by CO₂ and recent experimental studies have pointed out that also H₂O has a significant inhibitory effect on the rate of CO₂ methanation. Hubble et al. [29] investigated the kinetics of CO₂ methanation over a wide range of partial and overall (up to 20 bar) pressures, using a 12%_{wt} Ni/ γ -Al₂O₃ catalyst and temperatures between 445 and 497 K. They found out that the rate increased with increasing partial pressures of H₂ and CO₂ at low partial pressures. However, the rate of reaction was found to be insensitive to partial pressures at higher partial pressures. Their model assumes a dissociative mechanism in which the rate-limiting step is the dissociation of adsorbed CO and the most abundant species are CO, O and H₂O.

The kinetic expression and the related parameters (table 2.4) providing the best agreement with previous literature data and the best fit to the experimental results, are reported:

$$r = \frac{ap_{CO_2}^{0.5}p_{H_2}^{0.5}}{\left[1 + b\left(\frac{p_{CO_2}}{p_{H_2}}\right)^{0.5} + cp_{CO_2}^{0.5}p_{H_2}^{0.5} + dp_{H_2O}\right]^2} \quad (2.18)$$

A	2652	[molbar ⁻¹ g ⁻¹ s ⁻¹]
B	0.055	[]
C	0.0251	[bar ⁻¹]
D	0.0958	[bar ⁻¹]
E_A	85.4	[kJmol ⁻¹]
ΔH_B	-9.20	[kJmol ⁻¹]
ΔH_C	-8.10	[kJmol ⁻¹]
ΔH_D	-1.14	[kJmol ⁻¹]

Table 2.4 Values of the activation energy, heat of adsorption and the corresponding pre-exponential factors for the parameters

2.2 SNG production processes from coal and biomass

Kopyscinski et al [11] reviewed the production of SNG from coal and biomass. Historically, the first applications of thermochemical catalytic SNG production involved carbon sources and in particular coal. Established gasification processes were applied to this pathway to synthesize methane from syngas. For example, *Lurgi's* coal gasification process (figure 2.12) was developed in the 1930s in Germany and in the 1960s and 1970s the technology was applied to produce synthetic natural gas. The unit included two adiabatic fixed bed reactors with internal recycle; two pilot plants were built in Austria and South Africa. The plant in Austria converted syngas from naphtha to methane. In the second plant, the synthesis gas came from a commercial coal gasification plant, which included a shift conversion and a Rectisol scrubber, which is a commercial process (by Linde and Lurgi) using cold methanol as a physical solvent to separate acid gases from the synthesis gas.

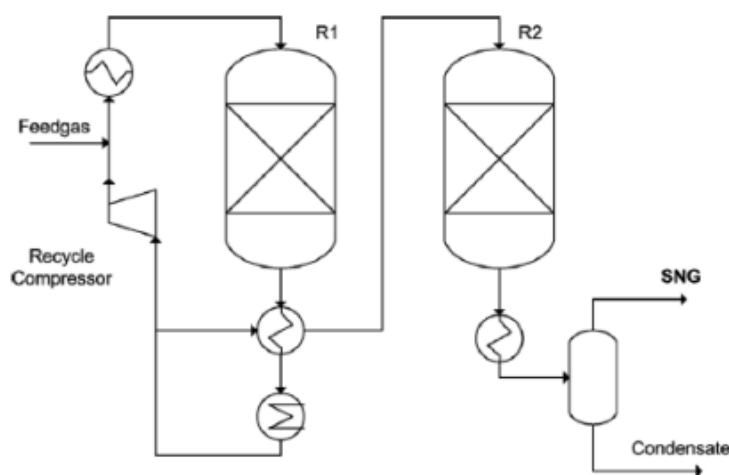


Figure 2.12 Lurgi process scheme [11]

The pilot plants worked for 1.5 years with two different catalysts: a commercial catalyst with 20 %_wt Ni/Al₂O₃ that showed a fast deactivation and a special catalyst developed by BASF with a high nickel loading. Temperature, pressure, the influence of H₂/CO ratio and CO₂, H₂O, higher hydrocarbons, and sulphur content were investigated. The technology itself is still commercially available from Air Liquide. The results of these studies led to the design of the Great Plains synfuel plant in North Dakota which began operating in 1984. This plant is the only commercial-scale coal gasification plant in the US which produces natural gas, with the capacity of an average daily production of 153 million standard cubic feet of SNG [30].

The process consists of 14 fixed-bed gasifiers followed by a shift conversion unit. An updraft gasification of lignite (18000 tons per day) with oxygen and steam takes place in a pressurized reactor. An air separation unit, combining molecular sieves and a cryogenic separation, provides the oxygen. Water is condensed from the resulting gas to raise process steam and hydrocarbons and sulphur are removed by Rectisol scrubbing. The product gas is compressed and dried after methanation and, following the CO₂ removal, the SNG is injected in the national gas grid. The separated CO₂, supplied to the world's largest carbon capture and storage project in the world, is used for enhanced oil

recovery. The methanation catalyst lifetime is about four years. Simplified process flow diagram is showed in figure 2.13.

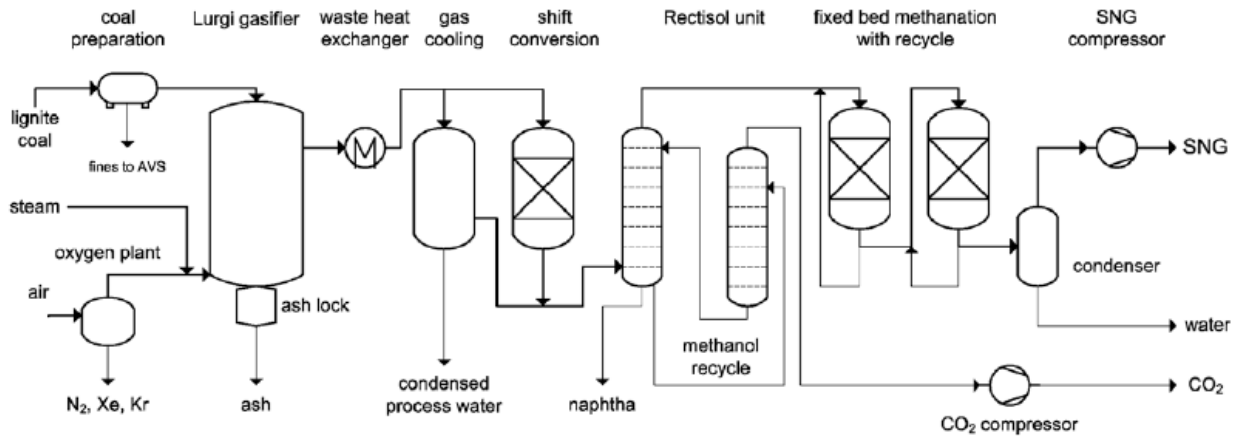


Figure 2.13 Simplified process flow diagram of the GreatPlains synfuel plant [11]

In the 1970 and 1980s, Haldor Topsøe investigated steam reforming of methane and its reverse reaction, methanation, to exploit the high reaction enthalpy of the reactions: steam reforming was carried out using nuclear energy and then the synthesis gas was transported to a heat-consuming site and reconverted in a cyclic process to produce heat. *TREMP* stands for Topsøe’s Recycle Energy efficient Methanation Process and it is based on a heat recovery concept. The recovery ensured is very effective: up to 85% of the heat from the methanation reactions is recovered as high pressure superheated steam using the exit gas from the first reactor. The plant is made of three adiabatic fixed bed reactors, including a recycle to the first reactor, operating in a range of temperature from 250 to 700 °C, pressure up to 30 bar and with a near stoichiometric ratio of hydrogen to carbon oxides at the inlet. In 1986 the original project terminated but the TREMP process is still used to produce SNG from synthesis gas. The technology relies on the unique Topsøe MCR methanation catalysts presenting high and stable activity in a wide temperature range [31]. The process has been demonstrated in plants of semi-commercial scale producing between 200 and 2000 Nm³ /h of SNG under realistic industrial conditions [32].

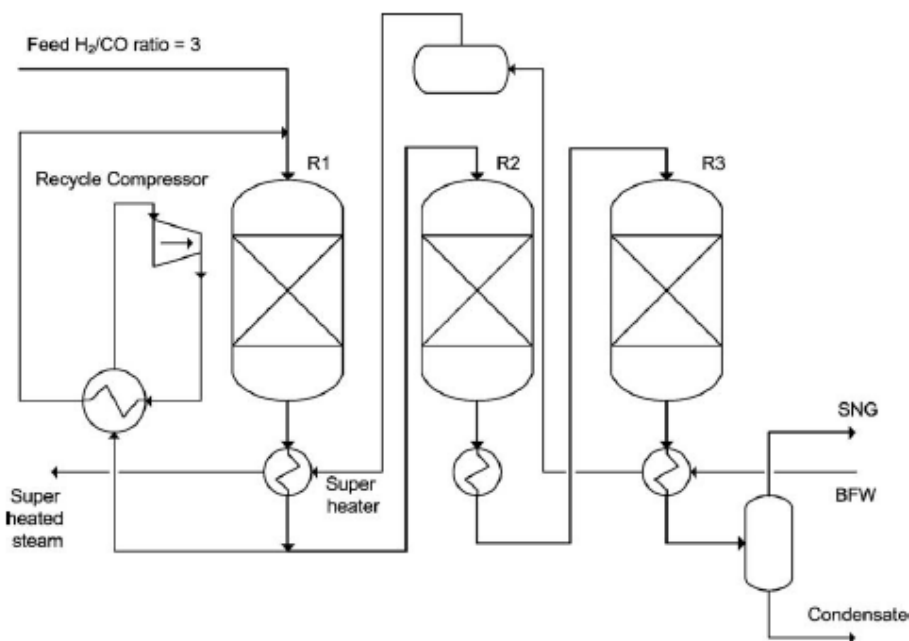


Figure 2.14 TREMP process scheme [11]

Another technology based on multiple adiabatic fixed bed reactors is the *RMP* (Ralph M. Parsons process), which is a high temperature methanation with no gas recycle. The process, depicted in figure 2.15, relies on a series of 4-6 adiabatic fixed bed reactors with intermediate gas cooling. The steam is added to the first reactor whereas the syngas could be fed into the first four reactors with different distribution ratios. The process parameters can vary as follow: pressure between 4.5 and 77 bar, the inlet temperatures between 315 and 538 °C and the H₂/CO ratio between 1 and 3. In the first reactor, CO was basically converted to CO₂ via water gas shift and, to a lesser extent, to CH₄. In this scheme, water and carbon dioxide are removed at the end of the series and the product gas is fed to a final dry methanation stage that reduces the hydrogen and carbon monoxide content below 3 and 0.1 %_{vol}, respectively.

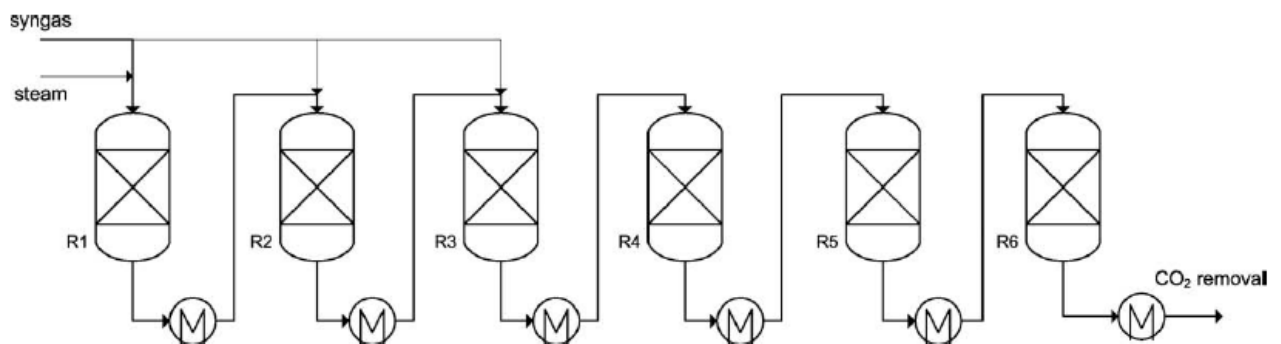


Figure 2.15 RMP process [11]

A further high temperature methanation process, similar to the RMP one, was designed by the *ICI* (Imperial Chemical Industries, Great Britain) to generate SNG from the syngas produced by a coal gasifier. The series of three adiabatic fixed bed reactors with intermediate gas cooling is reported in figure 2.16. The first inlet temperature was set to 400 °C and steam was added in order to keep the temperature below 750 °C. The ICI developed a catalyst suitable for the process, with a high nickel load (nickel oxide 60%). However, no large-scale plant has been built.

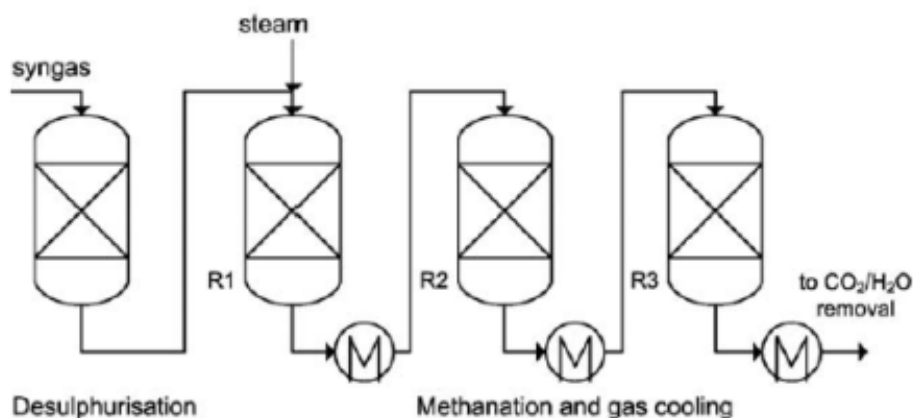


Figure 2.16 ICI process [11]

A last, well-known project regarding adiabatic fixed bed methanation, with intermediate gas-cooling and recycles, is that developed by the British Gas Corporation: the *HICOM* process. The scheme of the shift/methanation unit is shown in figure 2.17. In the first reactor, to contrast carbon formation, steam is fed although it enhances catalyst sintering and decreases the thermal efficiency. After the first reactor, there is a further low temperature fixed bed methanation reactor where the not recycled part of the product gas from the main reactor, is fed: here, the unconverted CO and H₂ are transformed to CH₄ and CO₂. The heat of the reaction is mostly used to generate high-pressure steam. No data for *RPM*, *ICI* and *HICOM* experiments and projects, in contrast to the other technologies presented above, are available to date.

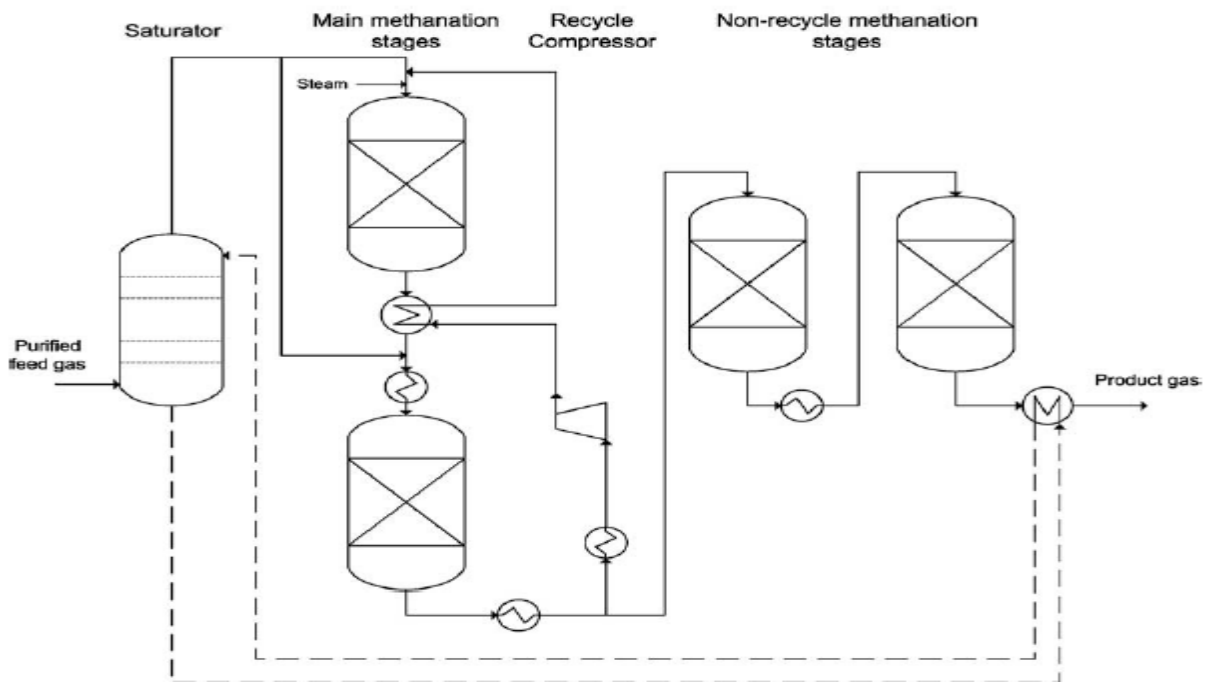


Figure 2.17 HICOM process: simplified process flow diagram [11]

In addition to the most widely applied fixed bed reactors, also the isothermal fixed bed reactor solution was designed to carry out methanation: the German company *Linde AG* according to the concept, achieved the isothermicity by means of an indirect heat exchange realized by cooling tube bundles incorporated in the bed. In this process (figure 2.18), the heat of the reaction is used to produce steam, which is partially added to the syngas to avoid carbon deposition. The reactant mixture is fed to the isothermal bed and to a second adiabatic methanation reactor. Part of the product gas from the isothermal reactor can be fed to the adiabatic one to increase the methane yield. Nowadays, the *Linde* technology is known to be applied in methanol synthesis plants.

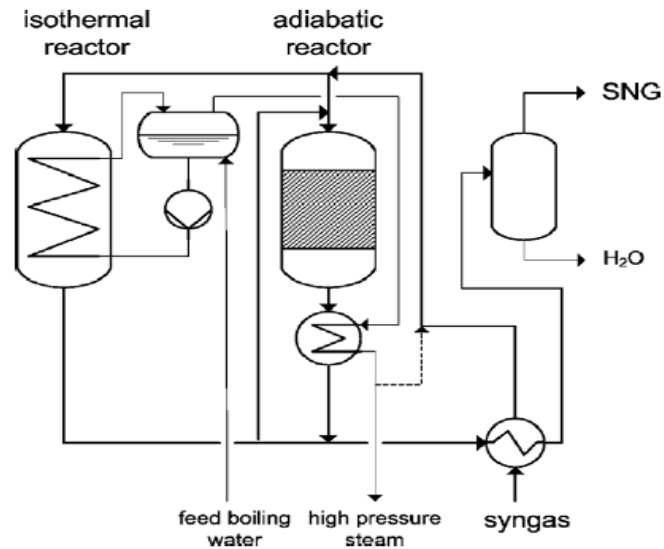


Figure 2.18 Linde SNG process [11]

Different projects were started also exploiting the fluidized bed technology: in 1952, the *Bureau of Mines* (United States Department of the Interior) started a research project to produce SNG from coal. They developed three methanation reactors: one fixed bed and two different fluidized beds. The fluidized reactors had a length of 180 cm and a diameter of 19 mm and 25.4 mm ID and were multiple-feed fluidized beds to achieve a good temperature control. The reactors operated in a temperature range of 200-400 °C with pressure up to 20.7 bar and a recycle (with a ratio up to four). The H₂/CO ratio varied between 1 and 3 and the superficial gas velocity was around 0.3-0.43 m/s. The catalysts investigated were an iron and a Raney-nickel based catalyst (d_p 63-180 micron) with nickel, predictably, being better than iron, i.e. more active and selective.

In 1963 Bituminous Coal Research Inc. (*BCR*, United States) started the *Bi-Gas project* (fig.2.19). The aim was to convert the coal using two stages: in the upper one (temperature of about 927 °C) coal reacted with steam and hot gas from the lower stage (1540 °C) to synthesis gas and char, this latter completely converted with oxygen and steam in the lower stage, generating the heat for the upper endothermic zone. After CO₂ and H₂S removal, the syngas was fed into the catalytic methanation reactor. More in detail, the methanation reactor (150 mm ID and 2.5 m the height of the reaction zone) included two feed inlets and two in tube heat exchanger bundles. In the reactor, a cooling jacket with a mineral oil wrapped the cone-shaped gas inlet zone. The process operated at high pressure (69-87 bar) and at relatively low temperatures (430-530 °C). Approximately, 23-27 kg of catalyst were charged, and the ratio H₂/CO was between 1.4 and 3. The experiments showed a conversion between 70 and 95%, for that reason, the product gas had to be fed to a last fixed bed methanation reactor. The industrial catalysts used contained nickel, copper, and molybdenum supported on alumina. The catalyst reached an almost constant size distribution during 160 h after the first few hours of fluidization during which the fines increased. As for the conversion, it was shown that about 96% of the CO was converted in the first part of the bed.

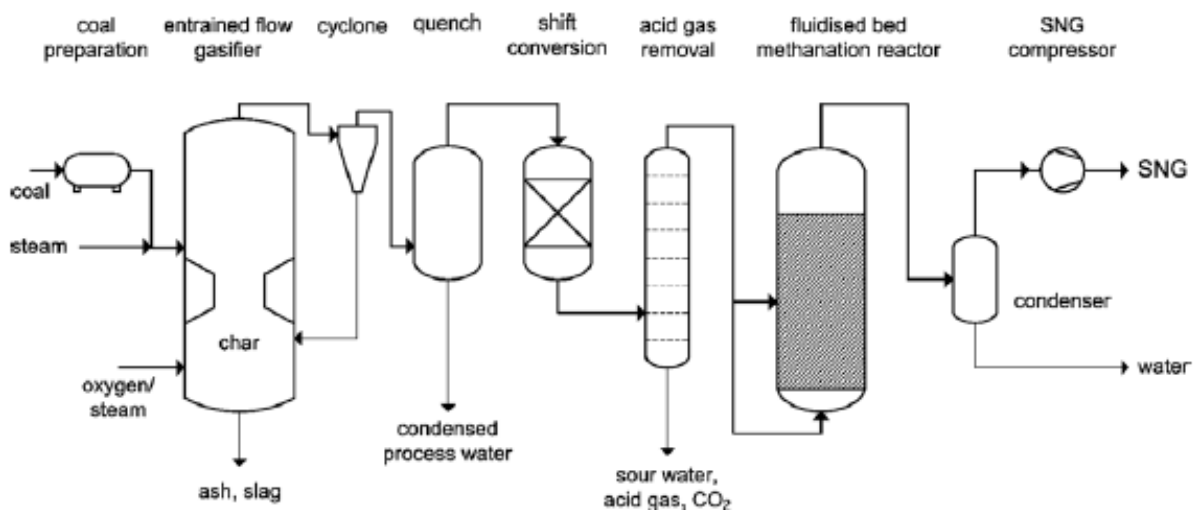


Figure 2.19 Bi-gas process flow diagram[11]

Following the above-mentioned projects, in Germany, the so-called *Comflux* process (the scheme is reported in figure 2.20) was designed and a pilot plant reactor was built. In 1981, also a pre-commercial plant was built (with about 2000 kg of catalyst, 2000 m³ SNG/h, up to 20 MW_{SNG}). The fluidized bed based process seemed to guarantee costs 10% lower than from a fixed bed process.

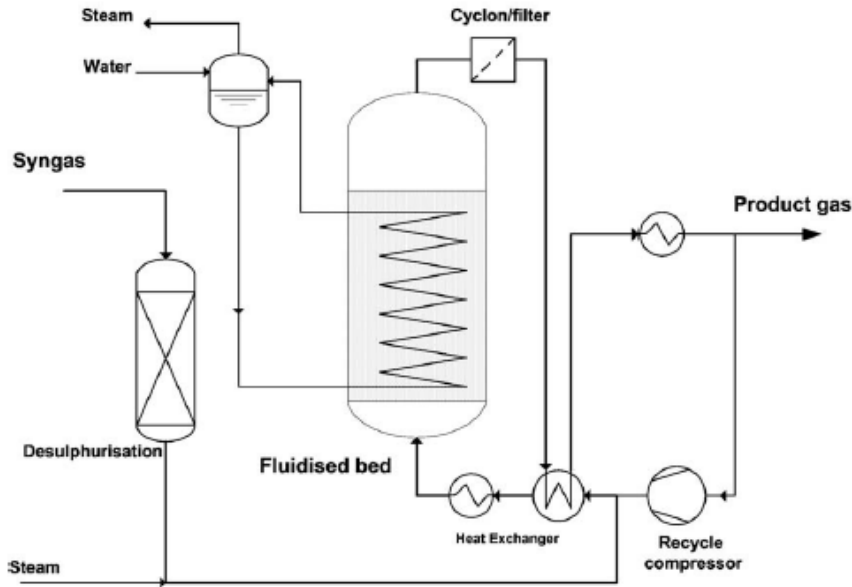


Figure 2.20 Comflux process scheme [11]

Still, *Exxon* Research and Engineering Company (US) studied a direct production of SNG via catalytic coal gasification (CCG) (figure 2.21). The reactor was a low temperature fluidized bed gasifier with water and recycled hydrogen and carbon monoxide as gasification agent. The catalyst utilized was an acidic salt of potassium. To separate products (methane, CO₂, water, ammonia, H₂S) and unconverted reactants, the process scheme is completed by an amine scrubber and cryogenic distillation. After a bench-scale reactor, a unit was erected in the early 80s in which 1 ton of coal per day was converted to SNG.

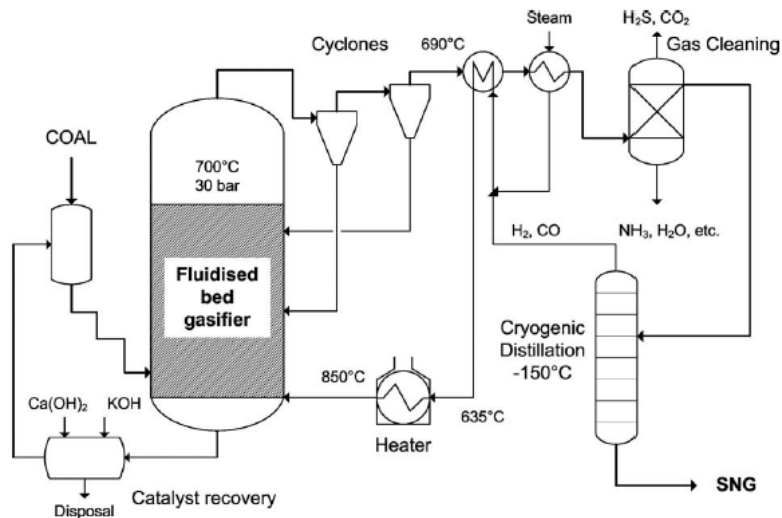


Figure 2.21 Exxon process scheme [11]

Lastly, a third different technology to be mentioned is the liquid phase methanation (*LPM*) proposed to produce SNG in a three-phase fluidized bed methanation reactor. The process (depicted in figure 2.22) consisted of a catalytic liquid phase methanation with a circulating mineral oil absorbing the heat of reaction, where a syngas from a coal gasifier was fed. Different nickel catalysts, process liquids and operational conditions (260-360 °C, 20.7-69 bar, H₂/CO ratio 1-10, with or without water addition) were set. However, the results pointed out low conversion and high catalyst loss from the fluidized bed reactor and the project was discontinued in 1981. Almost all these researches on fluidized bed reactors, over the years, especially when the oil price decreased, were interrupted and often no reports and information can be found in the literature.

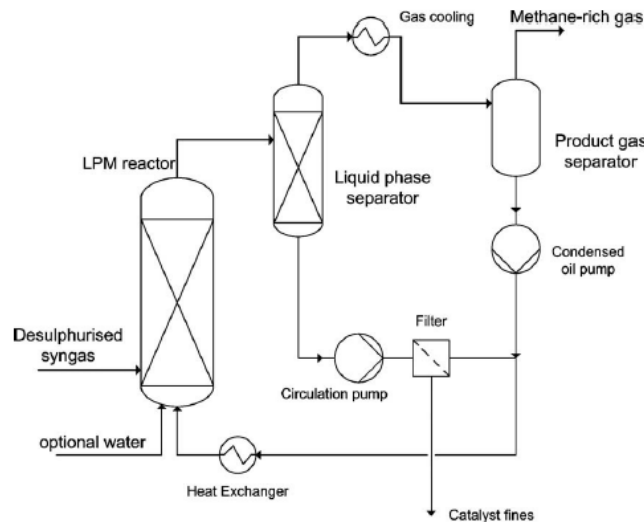


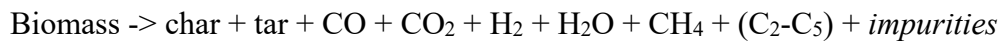
Figure 2.22 LPM concept [11]

However, in the last decades, SNG production from coal, especially in the United States, which have abundant coal resources, has gained interest again, due to the rise of natural gas price and dependency from its import.

The following processes have been proposed:

- the so-called hydro-methanation process has been studied by *Great point energy* with the aim of carrying out gasification and methanation in one apparatus at temperatures between 600 and 700 °C;
- the Arizona Public Service has made research on the so-called hydrogasification process: the coal gasification with hydrogen at quite low temperatures (around 870°C) and high pressure (70 bar). In the gasifier, a syngas containing methane is produced, with no catalyst: the syngas is then cleaned and compressed and the SNG injected into the natural gas pipeline.

Although there are no industrial applications so far, the most recent and promising studies on thermochemical SNG production from carbon sources, involve the use of dry, lignocellulosic biomass. This more recent concept of using biomass instead of coal to produce SNG is interesting but presents many challenges. Among them, biomasses are extremely heterogeneous in terms of chemical composition and kind of impurities, for example. The main steps of this process can be classified as follows: pretreatment, gasification, gas cleaning, methanation, upgrading and grid injection. The pretreatments are various: a biomass needs to be dried, pelletized, homogenized, and sieved. The gasification process is, extremely simplified, reported below:



Gasifiers can operate in a wide range of configurations: there may be allothermal or autothermal, pressurized or atmospheric reactors with air, oxygen, steam or carbon dioxide as gasification agent. Among the reactors, all the different types can be applied: fixed beds, fluidized beds or entrained flow reactors (EFG). In figure 2.23, the different reactor types are schematized.

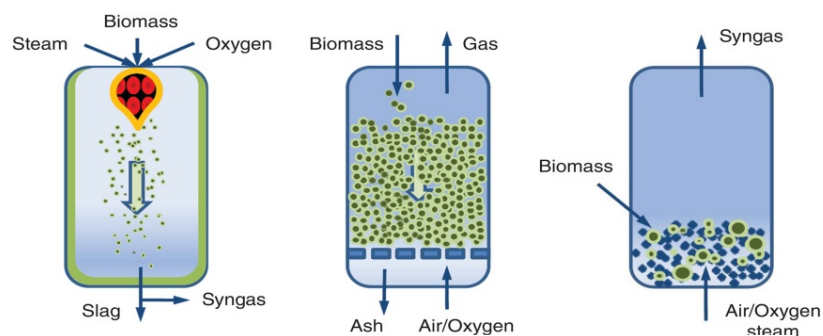


Figure 2.23 Scheme of the main reactor types applied for gasification (from the left: fluidized, entrained and fixed bed) [6]

Avoiding nitrogen dilution of the product gas is preferable so that oxygen gasification is generally preferred for subsequent SNG production. The most suitable reactors for these applications appear to be the indirect steam-blown fluidized bed and the pressurized oxygen-blown EFG. However, in a fluidized bed, the ash softening limits the temperature between 700-1000°C resulting in high tar contents needing to be removed, whereas the EFG technology, which still must be well developed for this application, requires high operation pressures (up to 60 bar). Contaminants from biomass gasification have to be removed for SNG production. Table 2.5 shows the allowed range for most of them.

Tars	2-20 g/Nm ³
Particles	10-100 g/Nm ³
Alkali Metals	0.5-5 ppm
H₂S	50-100 ppm
COS	2-10 ppm
NH₃	200-2000 ppm
Halogens	0-300 ppm

Table 2.5 Range of contaminants allowed for SNG production [6]

Essentially, the gas cleaning can be a cold or hot process, below 80°C or up to 1000°C, respectively. The former is mainly a process in liquid phase, i.e. scrubbing. Cyclones, filters, activated carbon, constitute the dry-cleaning techniques. Several hot gas-cleaning processes are still under development with few industrial applications; they present the significant advantage of minimizing downstream maintenance and increasing efficiencies. Typically, a raw-gas from gasification is separated by cyclones removing particles down to the μm -range with an efficiency up to 99.6%; downstream are often applied filters, enhanced using different techniques as for example the pre-coating of the particles with CaO. Alkali components are removed through condensation, tars not removed during gasification are eliminated by reforming/cracking and sulfur and chlorine components, generally, by adsorption. Mostly the H_2/CO ratio is adjusted by a CO-shift before methanation. After methanation, the final upgrade is achieved via technologies already mentioned for the biochemical process. The scheme is represented in figure 2.24.

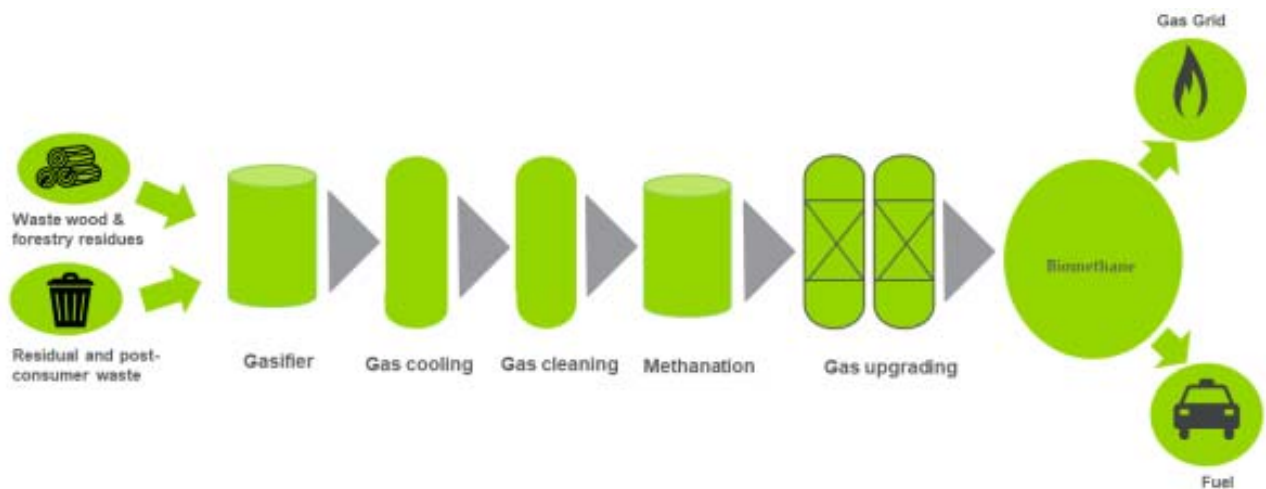


Figure 2.24 Schematic overview of the thermal gasification process [6]

The first important biomass-based projects date back to the early 2000s. The Energy Research Centre of the Netherlands (ECN) proposed a scheme of biomass gasification in a dual fluidized bed gasifier (*MILENA*), gas cleaning, methanation and SNG upgrading. The producer gas came from a wood gasifier and was purified by means of different steps [33]. *MILENA* gasification involves a temperature level of 850 °C with a complete conversion of the fuel, no carbon in the ash and a product gas containing methane, ethylene, benzene, and tars. The system is characterized by high efficiency, compact design and fuel flexibility. The tar removal is the ECN *OLGA* process, a multiple stage scrubber using a scrubbing oil. More stages are necessary to separate, first heavy and then light tars, in a series of absorbers/strippers. All tars can be recycled to the gasifier where they are consumed contributing to the energy efficiency. The methanation proposed by ECN within the project is a traditional multi-stage fixed bed methanation with Bio-Methane production concept, proven only on lab-scale so far. The process is depicted in figure 2.25.

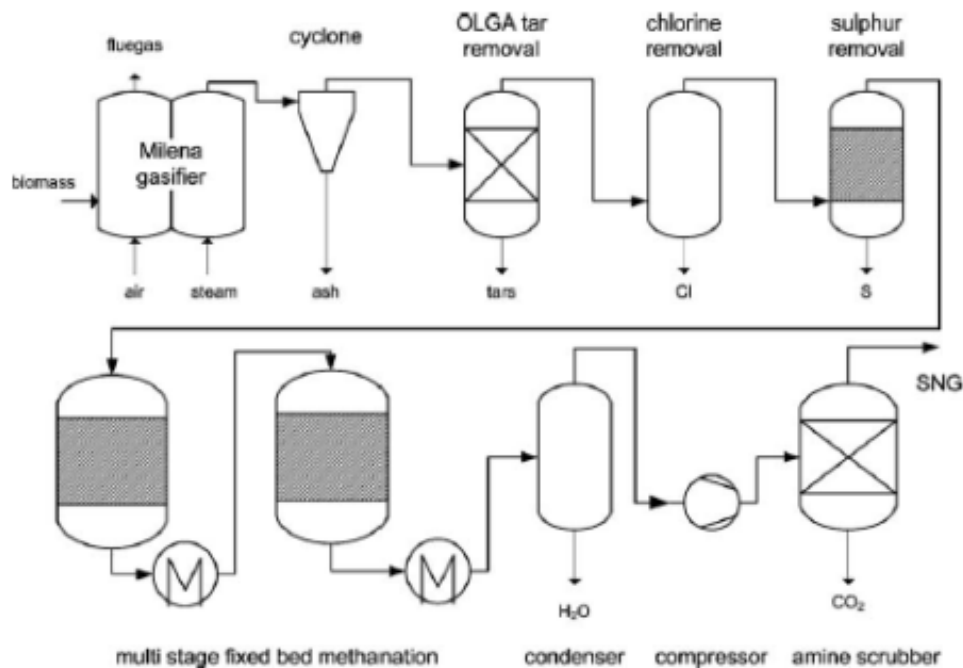


Figure 2.25 ECN methanation scheme [11]

ZSW in Germany investigated the fixed bed methanation with commercial Ni-catalysts downstream of an Adsorption Enhanced Reformer (AER). AER is an enhancement of the indirect gasification with a chemical looping involving CaO, which contains energy for the process as chemical latent heat, released when, absorbing CO₂, it turns into CaCO₃. The main result of this process is a producer gas with a high content of hydrogen (hydrogen from 37 % to 50 % at the expense of CO₂), which is directly convertible to CH₄ without a shift reaction. The methanation unit, tested with 50 kW production of SNG, consists of one reactor whose temperature is controlled with a molten-salt-cooled multi-zone heat exchanger.

The Paul-Scherrer Institut (PSI, Switzerland) studied how to convert wood to SNG using for gasification the Fast Internally Circulating Fluidized Bed (FICFB): this process has operated under commercial conditions in Güssing (Austria) since 2002 as a combined heat and power (CHP) plant. The producer gas is nearly nitrogen-free and methane-rich but, containing about 3 %_{vol} of ethylene and unsaturated hydrocarbons, can cause massive carbon formation at high temperatures. For this reason, the *Comflux* fluidized bed methanation was proposed due to its good temperature control. A 10 kW_{SNG} scale reactor, built at PSI, was connected to the gasifier in Güssing (Austria) [34]. Carbon deposition due to the presence of olefins and organic sulphur species was the cause of the deactivation of the catalyst so that catalyst stability was investigated as the crucial aspect to improve, achieving in 2007 a catalyst lifetime of more than 1000 h with a methanation step leading to a high methane content (about 40%). Based on these results, the project *Bio-SNG* led to the development of a 1MW_{SNG} unit in Güssing that was a demonstration of the whole process chain from wood to SNG in half-commercial scale. The process converted wood-derived producer gas to SNG applying PSI/CTU fluidized bed methanation. In 2009, the unit was operated during 250 h producing 100 m³/h of SNG. Figure 2.26 reports the scheme of the entire process designed for the Güssing plant.

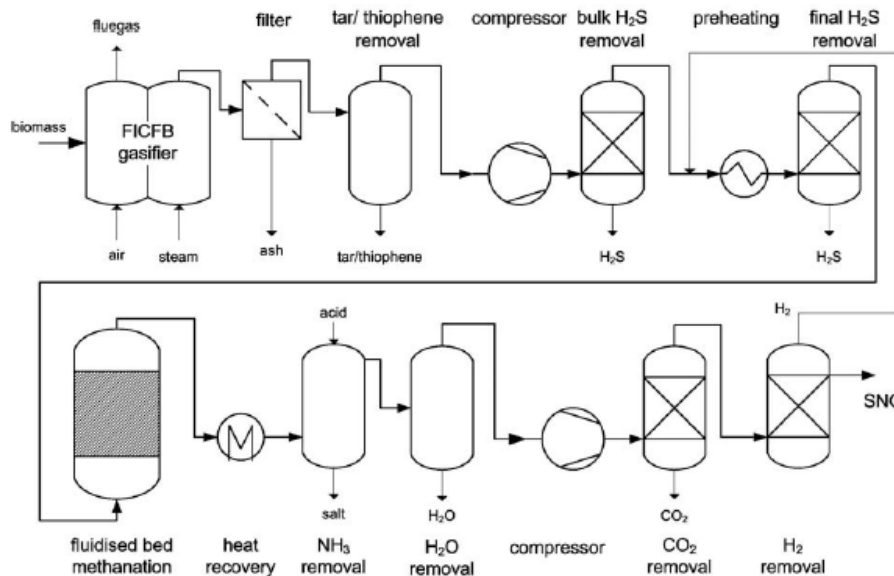


Figure 2.26 Process development unit in Güssing, adapted from [11].

During the last decades, several commercial international SNG projects have been announced: mostly in the US and China. US projects proposed mainly the *TREMP* process using coal but including carbon capture and separation (CCS) technology. The Gothenburg Biomass Gasification Project (*GoBiGas*) was proposed in Sweden to produce Bio-SNG by thermal gasification of forest residues. The plant was inaugurated in 2014 but financial considerations led to the interruption of the commercial scale project the following year.

2.3 SNG production projects in Power-to-Gas technology

Among the methanation processes, those related to CO₂ methanation still need to be mentioned, which are examples of Power-to-Gas (P2G) technologies. Most of the P2G projects are in Germany, Denmark, the United States of America and Canada. From 1993, 153 projects were developed, from research level up to pilot and industrial scale, in 22 countries. About 43% of all projects focused on CO₂ methanation, half of which covered biological methanation and the other half the thermochemical one. Carbon sources investigated were essentially biogas or sewage gas from wastewater treatment plants, bioethanol/alcoholic fermentation plants (two projects), syngas from biomass and fossil power plants. Nearly 45% of the projects inject their product gases, mainly methane, into the gas network. In 2019, 95 of the suggested projects were active globally with an electrical power of 38.6 MW_{el}. The trend of the average plant size grew over the years. Hydrogen and methane systems efficiency reached the middle of the theoretical ones. It could be due to the fact that only few projects include off-heat usage, and, in conclusion, auxiliary systems significantly influence overall efficiency. Two important examples of German plants are in Falkenhaghen, producing hydrogen (2MW, 360 Nm³ of H₂ per hour from wind energy) and in Werlte, producing synthetic methane, both feed the produced gas into the natural gas infrastructure [35]. The latter, the Audi e-gas plant, is the largest industrial P2G plant in the world with 3 alkaline electrolyzers each of 2 MW_{el}, powered by a wind farm located in the North Sea including 4 turbines of 3.6 MW_{el}. The CO₂ comes from a nearby biomethane production plant. The unit is made of a single refrigerated fixed bed reactor with a production around 1000 t/year: this plant dynamically follows the availability of electricity supplied by the wind farm (approx. 4000 h/year) with an overall efficiency of 54%, without taking into account the reuse of the thermal energy produced. As for Italy, interest in the PtG is gradually growing. The two main operators of the high-pressure gas network, Snam Rete Gas and Società Gasdotti Italia, are committed to study the implementation of the technology to promote the energy transition and the decarbonization of the gas sector. A demonstration plant was built in Troia (FG): it produces 3.6 kg/h of H₂ using a 200 kW_{el} alkaline electrolyzer (AEL) whereas CO₂ is captured from the air by adsorption on porous materials. The feed stream, mixed with a recycle gas flow rate, is in a stoichiometric ratio H₂/CO₂ = 4. The stream leaving the methanator is purified and the methane is liquefied. Figure 2.27 is the conceptual scheme of the reactor configuration applied in CO₂ methanation projects.

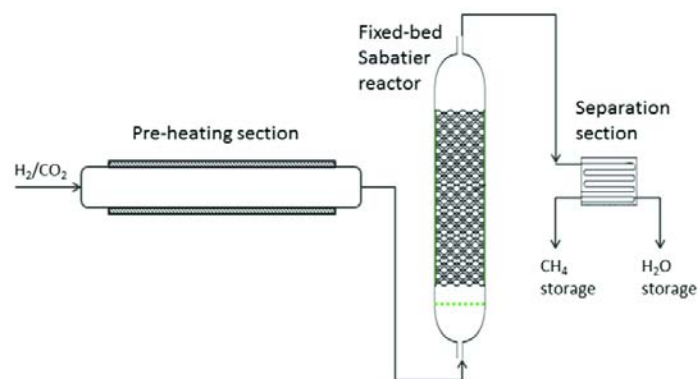


Figure 2.27 Scheme of a classical CO₂ methanation process in a PtG application [36]

2.4 Comparison between economics of the SNG production pathways

To perform a comparison about economics and market maturity of the different described pathways to produce SNG, the concept of Technology Readiness Levels (TRLs, from 0 to 9) should be introduced: it estimates the maturity of the developing technologies.

Biochemical SNG production is found at the highest TRL, 9: “full commercial application, technology available for consumers”. The production of SNG from biogas reached interest mainly within the last 20 years with the upgrading technologies presenting market maturity in small-scale applications.

The thermochemical production follows two trends: the Chinese and European ones. The former is focused on exploiting the huge coal resource by using the high capacities of TRL 9 type applications. On the other hand, European research is aimed mainly at studying the pathway from biomass, which stays at an overall TRL level of 4-7 (i.e. “small-scale prototype built in a laboratory environment”- “demonstration system operating at pre-commercial scale”).

The most recent concept as SNG production route is the electrochemical pathway that involves both the electrochemical synthesis of H₂ or syngas followed by a thermochemical methanation, and the purely electrochemical in situ methane synthesis [37]. This last concept, however, needs substantial advancements in developing a cathode electrocatalyst active for both steam electrolysis and methanation reactions.

The TRL for the former electrochemical concept introduced can be estimated in the range of 4-6 (“small-scale prototype built in a laboratory environment”- “prototype system tested in intended environment close to expected performance”).

As far as efficiency is concerned, different aspects influence them: design and scale, considered products, heat and power, injection pressure and time horizon.

Biogas plants currently achieve efficiencies in the range of 55-57%, but they are thought to increase in the mid-term due to the utilization of the energy of the fermentation residues and more efficient enzymes. The efficiencies of thermochemical process are in the range of 52-54% for EFG, higher for FBG, 64-70% for cold gas cleaning and up to 71-75% for fluidized bed with hot gas cleaning. The lower EFG efficiencies are due to the energy intensive feed preparation. The electrochemical technology currently reaches the range of 54-60%.

A comparison of SNG production technologies from an economical point of view is not straightforward, firstly because of different levels of development. Considering the three discussed technologies, the order of specific production costs is BIO < THC < ELE.

As for biochemical SNG production, the average value is 8 €/kWh_{SNG}, this specific production costs decrease with increasing plant scale and time horizon.

There are only a few economic data published for the thermochemical pathway, given the lower TRL compared to the biochemical one. For this pathway, production costs are calculated mostly by means of simulation-based economic considerations and the range extends from 5.6 to 37 €/kWh_{SNG} over widely different scales. It is important to point out that the thermochemical process offers a great cost reduction potential because, unlike the biochemical pathway characterized by the low energy density of the feedstock, favors large-scale operations (scale may exceed 100 MW_{SNG}).

Lastly, the electrochemical SNG production presents costs in a range of 8.2-93 €/kWh_{SNG}. According to published data, the mean investment costs for biochemical, thermochemical and electrochemical pathway are about 1300, 2600 and 3300 €/kW_{SNG}, respectively.

Currently, they are not competitive solutions when compared to the present natural gas prices, but all these concepts need to be necessarily investigated for the required energy system transition.

As for carbon dioxide methanation, several authors analyzed cost development giving a projection until 2030 with an outlook to 2050: for thermochemical methanation a cost reduction of about 67% up to 2050, while for biological methanation, a cost reduction of 75% [38]. The projections move towards an alignment of costs in the future considering the two processes and the cost reductions would depend on economy of scale. Recalling that cost for methanation does not include electrolysis costs, to reach this situation, electrolyzers, responsible today to make hydrogen production more expensive than methanation, should cost 75% less than at the present.

2.5 CO₂ methanation in Power-to-gas chain: concepts involved

CO₂ methanation to produce substitute natural gas involves more concepts, all of them in the context of the climate change mitigation strategies. In the most recent period, the renewable energies witness an ongoing growth: *“Renewables remain the success story of the Covid-19 era”*. The renewable energy demand grew by 3% in 2020, primarily driven by an almost 7% growth in renewable electricity in each sector: power, heating, industry and transport with solar PV and wind contributing two-thirds of this growth. China is likely going to contribute for half the global increase followed by the United States, the European Union and India. Regarding EU, the last climate directive dates to 2018 when a target of 32% share of renewable energy was set by 2030. In 2021, this goal was raised to 38-40% that would mean doubling the share of renewables, currently matching about 20% of the EU's energy needs. Moreover, EU countries reached an agreement on a new European law that makes the 2050 climate neutrality objectives a legal obligation [39]. The efforts to promote the renewable energy penetration in all the strategic areas meet the necessity to overcome a series of issues: among these challenges, one of the most important is the development of long-term and large-scale storage systems. The Power to gas process has the potential to solve these problems. The whole technology involves different issues: future energy systems architecture, technological aspects, social acceptance, marketing and political discussions [40]. Several literature sources point out that with the growth of the renewable power generation, PtG will be not only crucial but even cost-efficient [41]. So far, the technology is still characterized by high costs and losses during conversion. CO₂ methanation process is able to face also other aspects, such as the CO₂ emissions reduction via a CCU technology implementation. In this framework, the first methanation reactant, H₂, is renewable H₂ provided by using renewable electric energy surplus and the other one, CO₂ can be captured and utilized from different sources. In the following paragraphs, the topics involved by the CO₂ methanation in the PtG chain are discussed.

2.5.1 Energy Storage Systems

All the recent trends in the electric field are leading to the challenging shift towards distributed generation (DG): a decentralized generation model in small-scale self-generating electrical units located in multiple places and connected directly to the electricity distribution grid. This model is conceived as incorporating renewable energy resources (RERs) with a growth which is expected to continue, as indicated in figure 2.31.

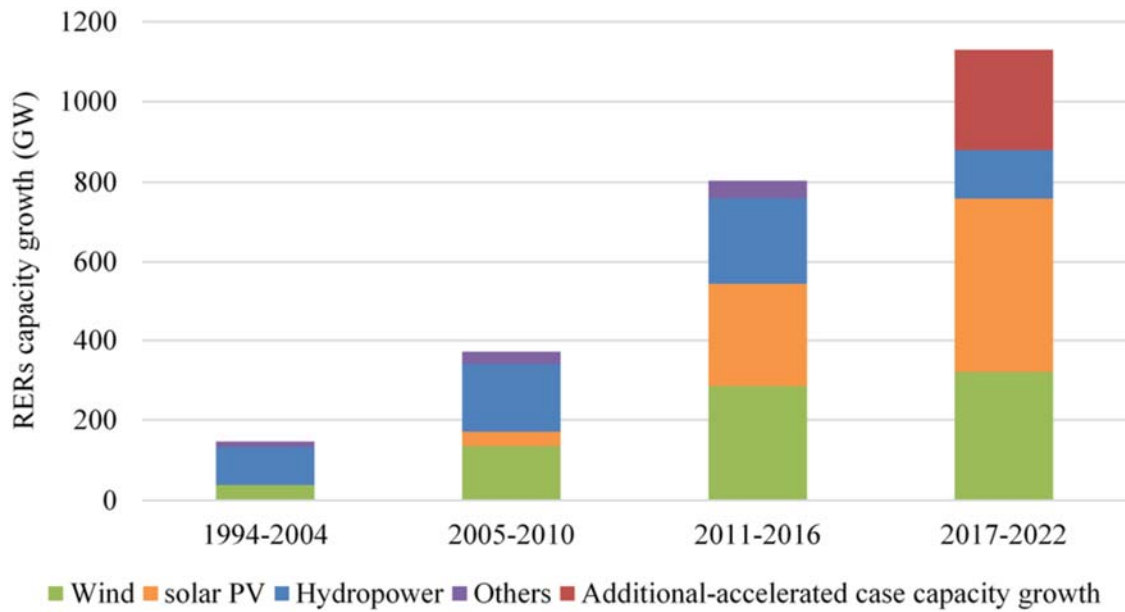


Figure 2.31 Growth of RER-based electricity generation worldwide [42]

The associated challenges consist mainly in the unpredictable, stochastic, and intermittent nature of these resources with a consequent difficult immediate response to demand variations. The energy storage systems (ESSs) are needed to compensate these deficiencies but can also improve the grid stability, reliability, and efficiency. Electrical energy can be stored only if converted into other forms: mechanical, chemical, electrochemical, thermal, or electromagnetic energy. Different ESSs are used, and others are currently under development. The range of storage technologies is wide and the parameters governing these systems operation are numerous: power-storing capacity, energy and power densities, response time, cost and economy scale, operating life, monitoring and control mechanisms, efficiency. The scheme in figure 2.32 depicts the classification of these systems whereas figure 2.33 gives a picture of the maturity of such systems.

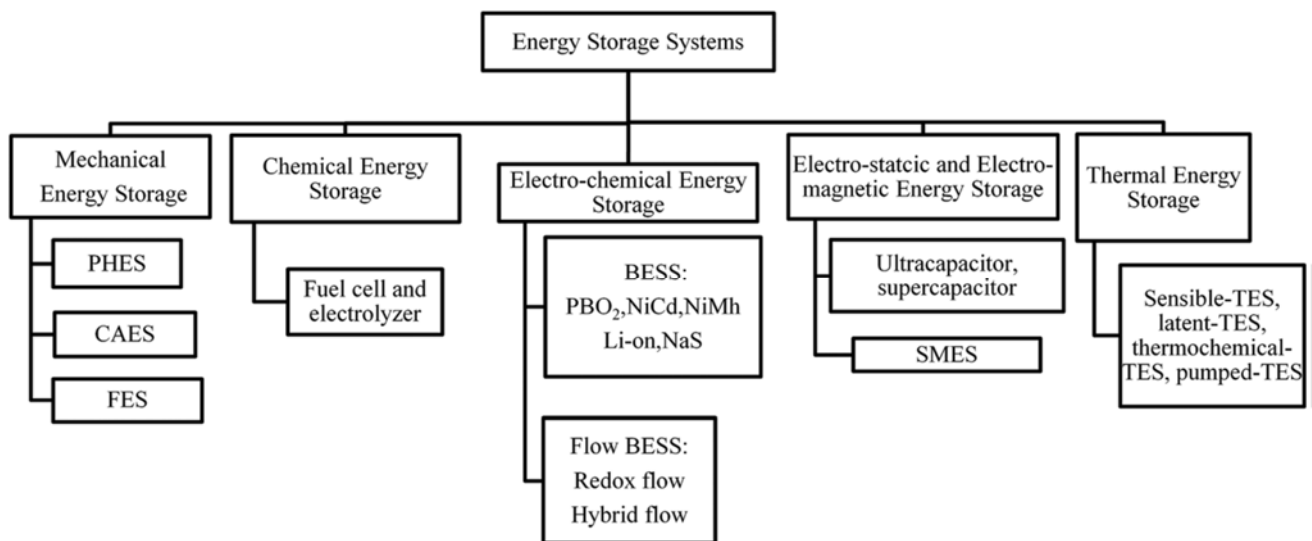


Figure 2.32 Energy storage systems classification [42]

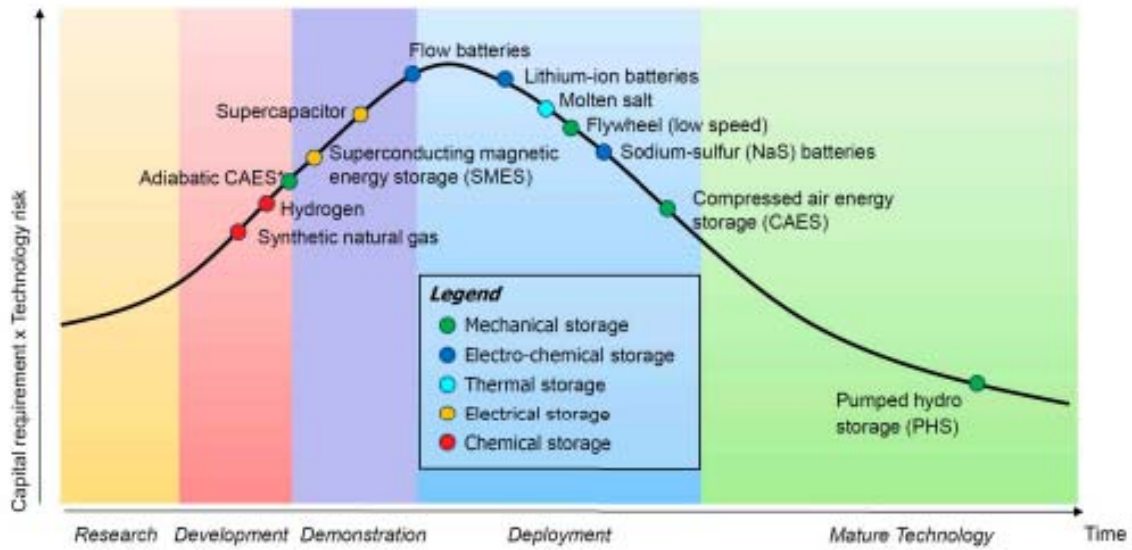


Figure 2.33 Maturity of energy storage technologies [43]

The most mature type of these storage methods, among the mechanical solutions, is the pumped hydro energy storage (PHES): nearly 96% of the total installed electrical energy storage capacity is in this form with a total installed ESS capacity of 183 GW worldwide. In figure 2.34 the share of the ESSs is reported.

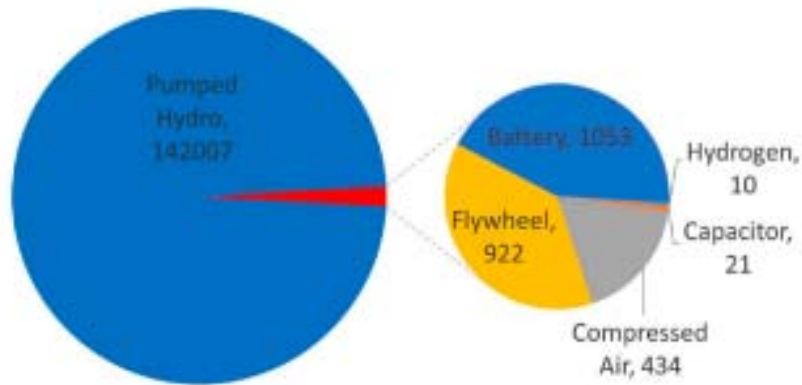


Figure 2.34 Share of global installed ESSs capacity in MW [43]

PHES involves the storing/releasing of the potential gravitational energy of elevated water: during a charging, the electrical energy is converted into mechanical and potential gravitational energy by pumping water at an upper reservoir. With the discharging process, water is released and electrical energy, to use in peak demand hours, is generated by turbines. This technology is applied mostly in high-power solutions presenting as the main drawbacks the high capital costs as well as a great dependency on the geographical site and a significant environmental impact on the site itself. Other mechanical systems are compressed air energy storage (CAES) and flywheel energy storage (FES). The former compress air, which is taken from the storage tanks, is heated and released through turbines and converted into electricity. Flywheels store energy in rotating mass by speeding it up during charging; the same machine generates electricity to the DG power system slowing down the rotating mass when FES are in discharging mode.

Electrochemical energy storage involves batteries (BESS) as the main components to store electrical energy in the form of chemical energy of the embedded substance. A wide range of types of batteries is available depending on the material of electrodes and electrolyte. Electrostatic (super capacitors) and electromagnetic (SMES) energy storage systems do not convert the electrical energy in other forms, but in the form of electrostatic and electromagnetic fields. Methods using heat for storage, the thermal energy storage (TES), can be latent, sensible, or thermochemical heat storage systems, depending on whether the heat is stored in phase changing materials (PCMs), in media changing exclusively their temperature or in thermochemical materials (TCMs) storing heat in reversible chemical reactions and sorption processes. The TES systems can store large amounts of power (tens MW as range) with small self-discharge, good energy density (80-250 Wh/kg), no negative environmental effects and relatively low costs. Their drawbacks are the low power density (10-30 W/kg) and efficiency (30-60%).

The choice depends largely on the applications: for power quality ones, storage technologies with very fast response (FES, BESS, SMES) are required, whereas for bridging power applications, continuity of supply instead of efficiency is the priority and TES and PHES ensure that [44]. As a means of energy storage, the chemical energy storage method is gaining great attention. This energy is the energy of chemical bonds released in a chemical reaction. Hydrogen energy storage system (HESS) is one of the most relevant technologies: the process involves the step in which hydrogen is produced and stored when an excess power is available and then the one in which the stored hydrogen is used by, for example, fuel cells. A HESS includes essentially a water electrolyzer, a hydrogen storage tank and a fuel cell that works by oxidizing hydrogen and generating electrons flowing via an external circuit and resulting in electricity. Hydrogen can be used directly or fed into a downstream methanation process. Both these solutions are included in the Power-to-gas technologies. This choice depends on several aspects. The main problem of hydrogen is the transport since the movement of this molecule is unfavorable both in gaseous and in liquid state. Even more important is the fact that there is not an already existing and well-developed infrastructure like the natural gas one. In addition, hydrogen has not achieved the public acceptance as energy vector, yet. The benefits of these systems are mainly the excellent energy density (800-10000 Wh/kg) and the negligible self- discharge (less than 3% per day); the critical aspects, which need to be solved to further develop this technology, are the high costs for large-scale applications and the need of improving the efficiency.

Among the existing energy storage technologies, a comparison in the diagram of the figure 2.36, on the basis of two significant parameters, is provided, in particular to point out the strengths of the

innovative Power-to-Gas technology (P2G). The technology presents a very high storage capacity (theoretical limits in the order of TWh), even more than three order of magnitude higher than the more conventional technologies such as batteries, compressed air and pumped storage. The chemical storage allows this capacity leading to the accumulation in a gas that can be liquefied, compressed or injected into pipeline networks. P2G is characterized also by a good flexibility in terms of discharge time with respect to the other technologies.

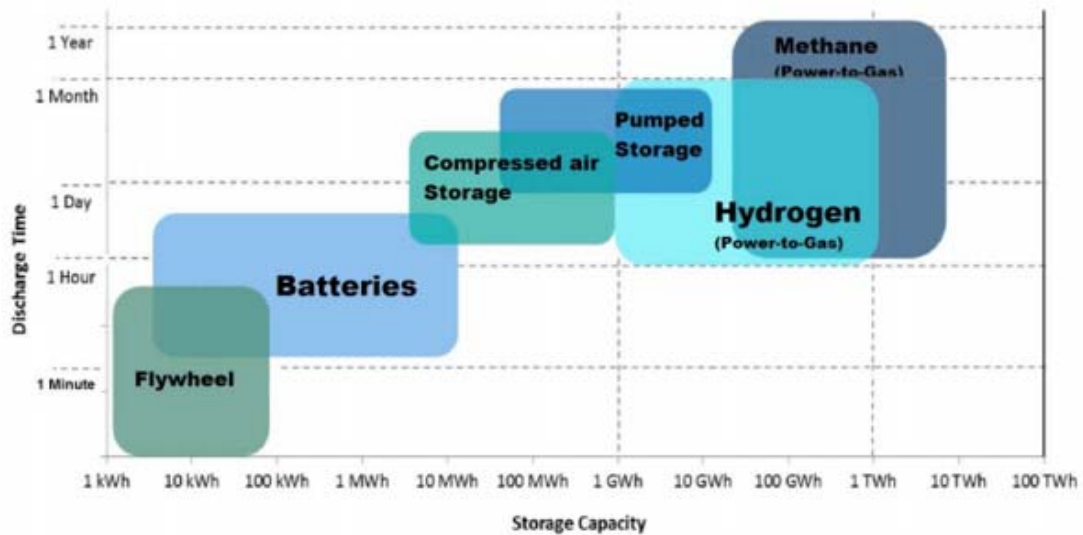


Figure 2.35 Classification of the different ESSs based on storage capacity and discharge time [45]

2.5.2 Carbon Capture and Storage (CCS) and Carbon Capture and Utilization (CCU) technologies

The Carbon Capture and Storage (CCS) and Carbon Capture and Utilization (CCU) processes consist of a series of techniques for the capture and sequestration and the capture and direct use of CO₂. The main phases are reported in the scheme of figure 2.36.

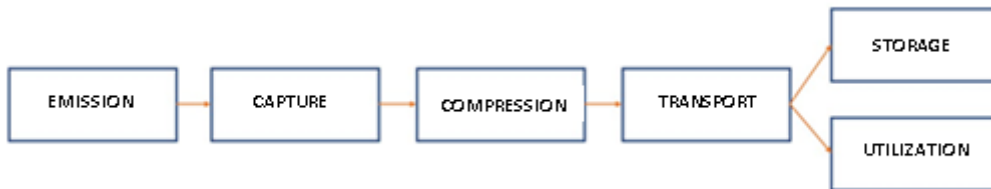


Figure 2.36 Conceptual diagram of the supply chain of CCS&CCU systems

For the CO₂ capture techniques is possible to apply the following classification [46]:

- pre-combustion capture
- post-combustion capture
- oxy-fuel combustion
- chemical looping combustion

The pre-combustion capture process basically involves syngas production, removal of CO₂ and combustion of hydrogen. The technique scheme is depicted in figure 2.37.

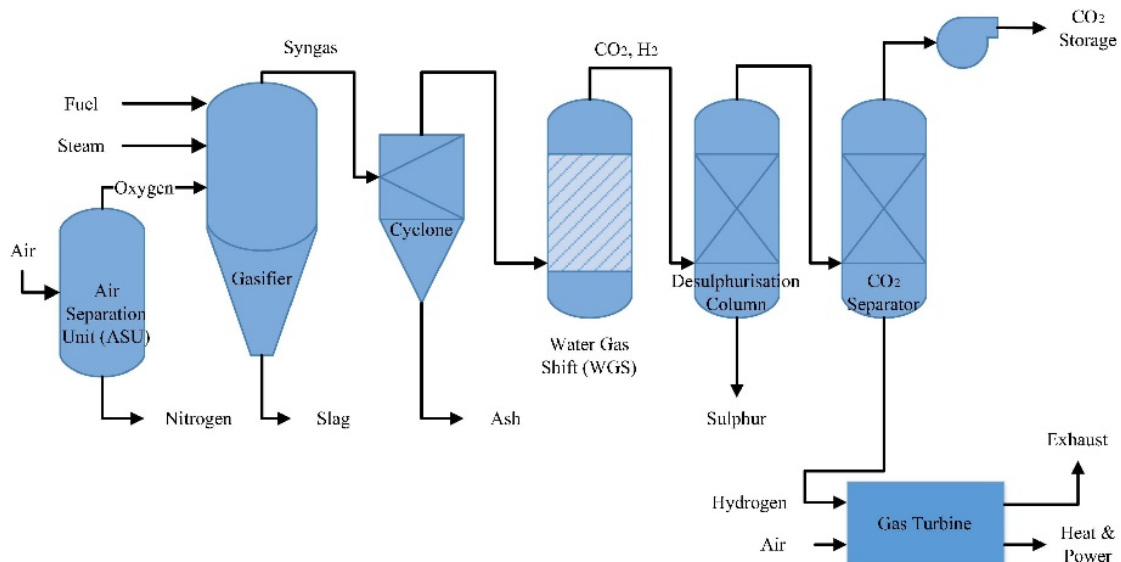


Figure 2.37 Process flow diagram of pre-combustion carbon capture system for gasification power plant [47]

To sum up the process: a partial oxidation of the fuel at temperatures higher than 800 °C is carried out with water vapor and oxygen, obtaining a raw syngas stream. The water-gas shift reaction is then exploited to convert the carbon monoxide into CO₂ and H₂. The produced stream is subject to chemical or physical CO₂ removal processes and then the CO₂ can be sent to the storage site. The H₂-rich stream from the CO₂ separation unit is finally used for energy production. The main advantage is to work with "clean" fuels, avoiding erosion and fouling of the system, which is a common issue for gas turbines. The air separation system and therefore the absence of N₂ result in an easier removal of the pollutants since their partial pressure is higher than in a traditional power plant. The main drawback is the loss of efficiency: in fact, it is impossible to produce CO₂ separately with no additional energy expenditure. In a comparison with the same energy produced, a plant with CO₂ capture entails higher fuel and investment costs.

Post-combustion capture processes consist in the treatment of exhaust gases produced by fossil fuels combustion. The main upside of this process (figure 2.38) is certainly the easy retrofitting. CO₂ from combustion gases, which is around 10-20%_{vol}, is separated through processes including chemical absorption (currently the most used), adsorption, membrane or cryogenic separation.

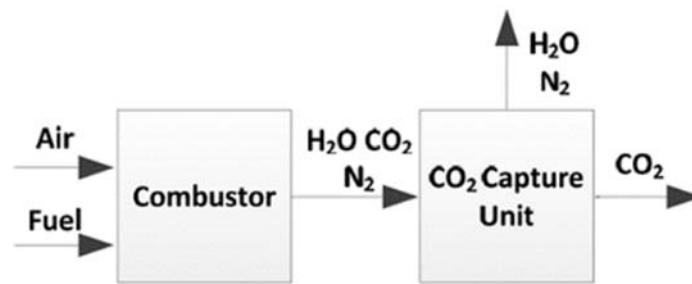


Figure 2.38 Scheme of a post-combustion capture process [2]

Chemical absorption (figure 2.39) exploits the reaction of an alkaline aqueous solvent with CO₂: MEA (monoethanolamine), MDEA (methyldiethanolamine) and DEA (diethanolamine) are generally the sorbents of choice for CO₂ separation. Amines are used to capture CO₂ from flue gases at low temperatures, carbon dioxide is then released at higher temperatures. These systems are characterized by significant energy costs and high environmental impacts for the production and regeneration of the sorbents. They, moreover, easily degrade thus can be used to treat only rather clean gas mixtures with only small quantities of impurities.

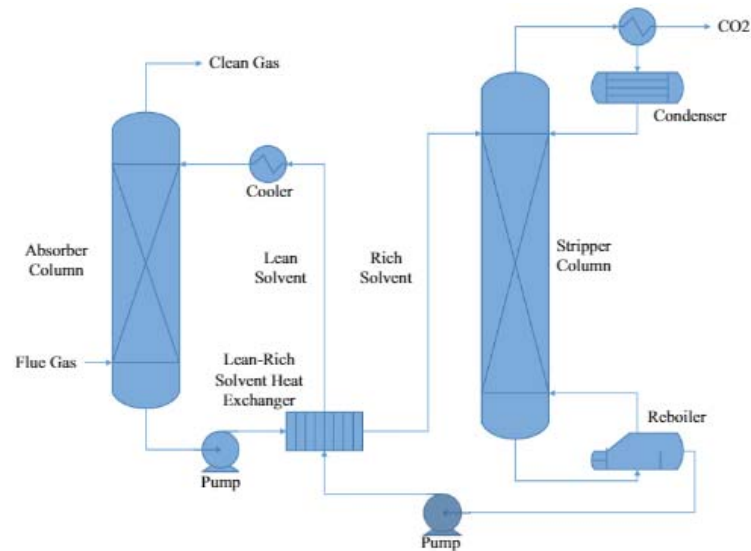


Figure 2.39 Scheme of the chemical absorption process of CO₂ [48]

Among the most innovative post-combustion capture processes, the Calcium Looping (CaL) is worth mentioning. This technique uses calcium oxide-based sorbents, generally obtained from natural limestone. The process, carried out by the means of two fluidized bed reactors (figure 2.40), a carbonator and a calciner, is based on the reversible carbonation reaction:

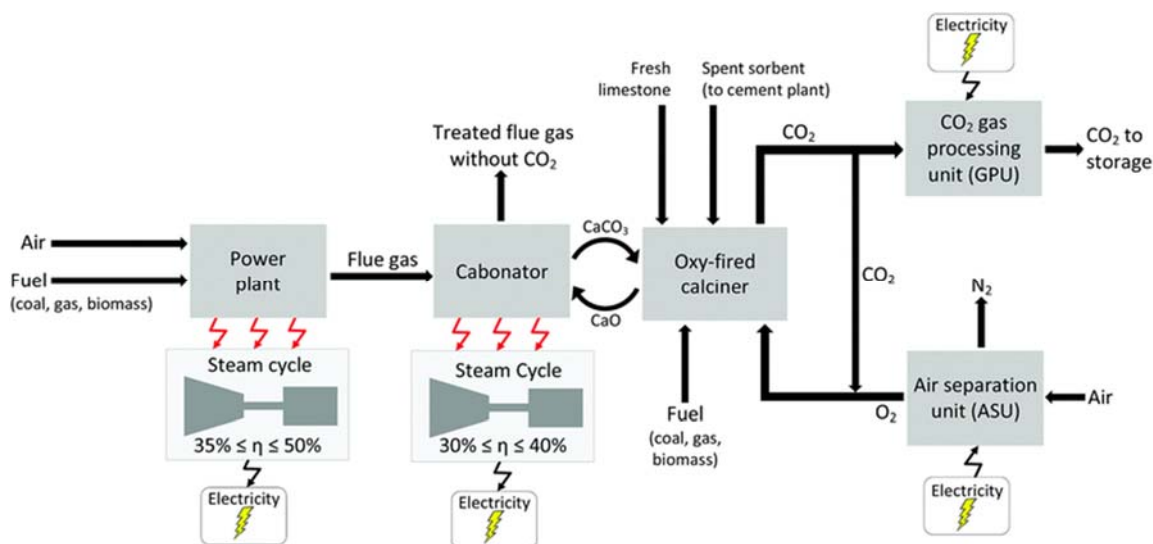
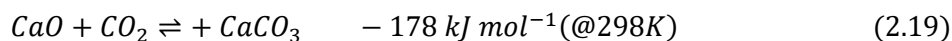


Figure 2.40 Calcium looping within a post-combustion capture process [49]

In the carbonator the calcium oxide reacts with the CO_2 at temperatures of about 650-700 °C obtaining the carbonate, which is continuously sent to the calciner where, at higher temperatures (850-950 °C), the reverse reaction occurs, regenerating the sorbent and releasing CO_2 in a concentrated stream that can be stored. A relevant advantage is the possibility of using sorbents deriving from natural and economical materials presenting a low environmental impact. Preliminary economic analysis [50] was carried out and the projections were positive: the cost may stand around US \$ 19.75/ton of CO_2 captured (systems applying amines cost about 32.5-80 US \$/ton of CO_2). Unfortunately, sintering phenomena severely affect the reactivity and, combined to the fragmentation due to the use of fluidized bed reactors [51], make it necessary to purge the exhausted sorbent and provide a fresh limestone make-up. Scientific community investigates the feasibility of reuse of exhausted materials to face the concerns about their disposal: some authors studied the possibility of producing from these materials a clinker with properties like those of commercial cement [52]. Other studies have focused on the feasibility of a reactivation of the exhausted sorbents through thermal pre-treatment or hydration, both by means of vapor or liquid water [53].

Based on the previous classification, the third technique is the Oxy-fuel Combustion. Here, the oxidant used is pure oxygen (up to 97%) (Figure 2.41) and the combustion gas thus mainly consists of CO₂ and water. After the water condensation, the nearly pure CO₂ stream is sent to storage. In the process, part of the exhaust gas is recycled to have a thermal flywheel in the combustion chamber, which enables to avoid overly high temperatures. The main penalty of the process is represented by the air separation unit, which can be quantified in 8-10 percentage points in terms of efficiency loss.

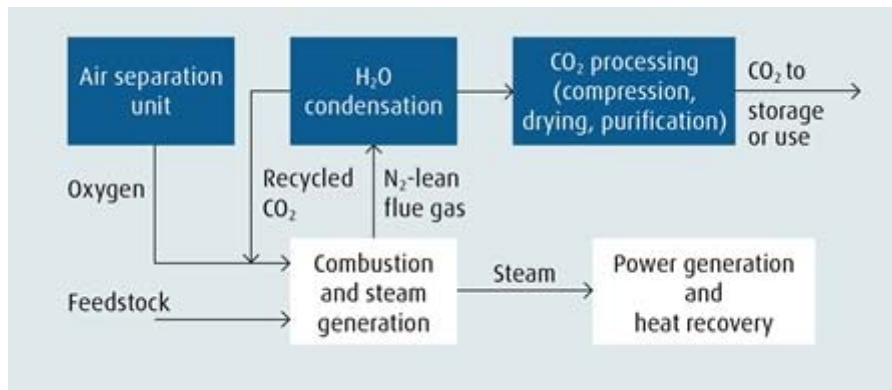
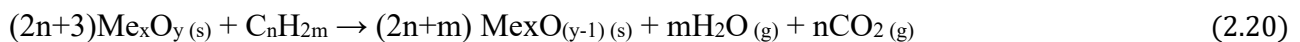


Figure 2.41 Oxy-fuel combustion scheme (Linde technology) [54]

Ultimately, the Chemical Looping Combustion (scheme in figure 2.42) allows the fuel not to come into direct contact with the oxygen. To transfer oxygen from air to fuel the use of an oxygen carrier (OC), typically a metal oxide, is required. Two reactors, in particular two interconnected fluidized beds, respectively called Air Reactor (AR) and Fuel Reactor (FR), are applied in this innovative technology. In the FR the fuel is oxidized by the metal oxide according to the general reaction:



where Me_xO_y and $\text{Me}_x\text{O}_{(y-1)}$ represent respectively the oxidized and reduced form of the oxygen carrier. Subsequently, the reduced OC is sent to the AR where air oxidizes it again, according to the following reaction:



The carrier can then return to the Fuel Reactor and the cycle restarts.

The stream leaving the Fuel Reactor (mainly CO₂ and H₂O), undergoes a condensation process.

Carrier oxidation is an exothermic reaction, while reduction is generally endothermic, the exceptions are represented by copper and manganese oxides, which are characterized by exothermic reductions. The choice of the oxygen carrier is one of the main parameters of the process and numerous characteristics have to be considered, such as:

- high reactivity both with the fuel and with oxygen in the temperature range of interest;
- high oxygen ratio (moles of oxygen that the carrier is able to exchange for moles of metal oxide);
- low tendency to attrition, fragmentation and agglomeration phenomena;
- low costs;
- low environmental impact.

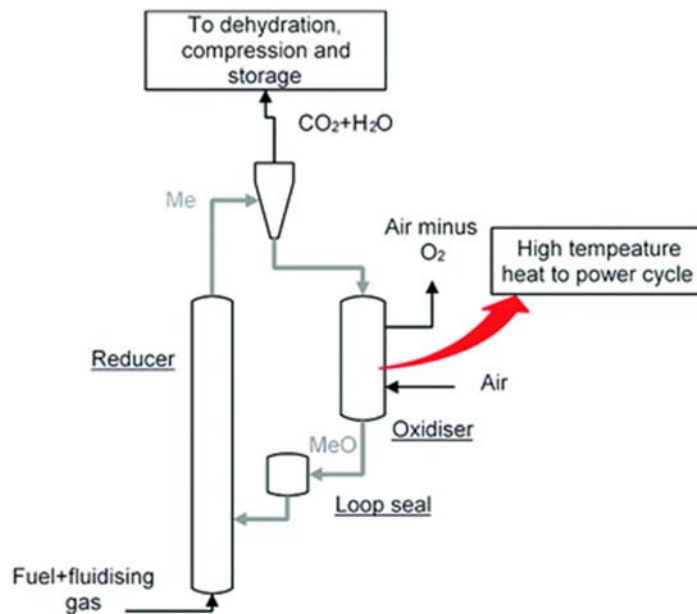


Figure 2.42 Chemical looping combustion capture process scheme [49]

Regards the economic point of view the capture process is the one affecting the most (about 80% of the total).

Following the capture and compression steps, the transport to the storage systems can take place in the liquid, solid or gaseous phase.

The transport of CO₂ by land is mostly operated using pipelines [55]. This method is the most efficient if the CO₂ comes from power plants whose life is greater than 23 years. For shorter periods, tanks are preferred. To optimize the mass/volume ratio, CO₂ needs to be transported as a dense phase (liquid or supercritical conditions). The optimal temperature and pressure ranges inside the ducts are 13-44 °C and 85-150 bar, respectively. One of the main problems is represented by the impurities that can lead to temperature and pressure variations. Furthermore, water, in concentrations greater than 50 ppm, could lead to corrosion due to the formation of carbonic acid.

There are several pipelines for the transport of gases and oil, but only a few are currently used for the transport of CO₂, and most are for the enhanced oil recovery (EOR) technology. This technique is based on the following concept: in exhausted oil or gas fields, if significant amounts of these substances are still trapped in the pores, the CO₂ could cause them to rise allowing an extraction otherwise difficult to perform. CO₂ contributes to keep the reservoir under pressure and acts as a solvent favoring the detachment of the oil from the rock. The safety level of CO₂ pipelines is very high; however the data are still uncertain since the extension of the transport network (EOR) is much smaller than that relating to oil/gas pipelines. A significant uncertainty is the durability of pipelines after long-term exposure to CO₂ flows, in terms of corrosion and fractures with possible supercritical CO₂ losses.

Turning to the storage processes, the geological method is the most studied: the greenhouse gas is injected into the subsoil (cavities of spent oil and gas fields or also exhausted marine fields, which is, however, less mature as technology). Compressed CO₂-rich stream injected into a porous and permeable rock tends to occupy the upper part of the reservoir rock but its migration towards the surface is hindered by the presence of a layer of compact and impermeable rock. Systems, which can be described as reservoir/rock rock/seal, are located at about 800 meters deep, where, due to the

pressure, carbon dioxide behaves like a supercritical fluid. CO₂ spreads as a gas in the pores of the rock but acts as a liquid in terms of density, occupying a volume about five hundred times smaller than that at the surface. Choosing the right site, carbon dioxide could be trapped for hundreds or thousands of years. Geological storage raises concern from an environmental point of view: several organizations make strong objections to the security of underground CO₂ confinement. Geologists claim that there are many solutions to obtain permanent and reliable capture even in case of violent earthquakes. In figure 2.43 the different geological storage options for CO₂ are depicted.

In addition, another noteworthy carbon dioxide storage technique is mineral sequestration, which can be carried out in situ or ex situ. Through these methods, CO₂ is fixed in the form of stable carbonate such as calcite (CaCO₃), dolomite (MgCa(CO₃)₂), magnesite (MgCO₃) or siderite (FeCO₃) [56]. For carbonation, the use of magnesium-based silicates xMgO·ySiO₂·zH₂O appears to be favorable since they are widely available in nature.

To sum up, as for the CCS technologies, they are thought to be a significant part of a range of techniques aimed at building a "near zero emission" future together with the exploitation of renewable sources and the energy saving policies.

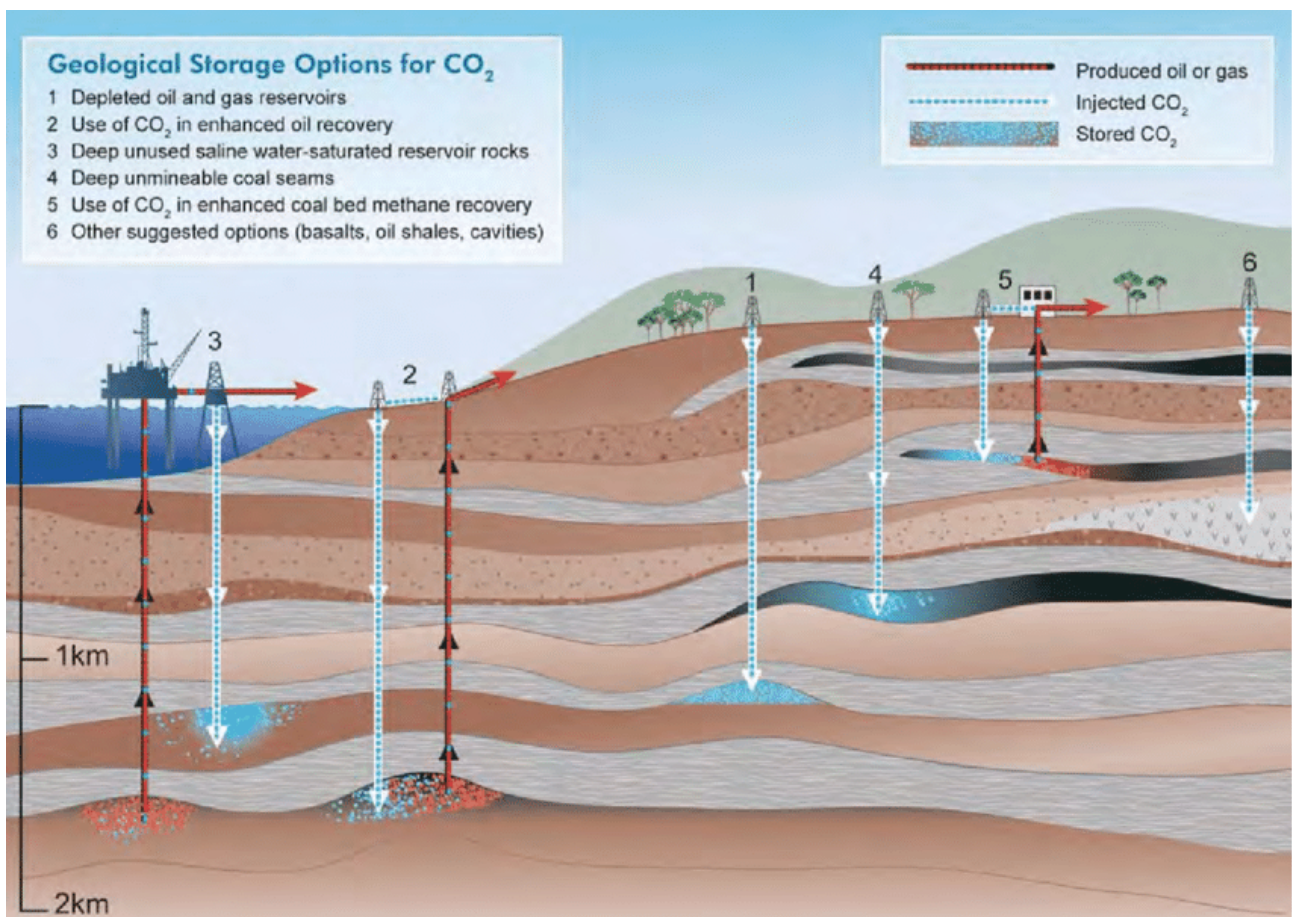


Figure 2.43 CO₂ storage processes [57]

The alternative to CCS is represented by the Carbon Capture and Utilization (CCU) techniques: in the CCU, the captured CO₂ is converted into commercial products. As well as evaluating its commercial profitability, it must be pointed out that due to the volumes involved, the CCU alone currently cannot settle the whole emissions issue.

Among the numerous examples (schematized in figure 2.44), micro-algae cultivation is an option of direct capture and use of CO₂ which received much attention recently. Micro-algae are microscopic plants growing both in salt and freshwater. For each ton of algal biomass, about 0.5 tons of carbon are fixed (from 1.8 tons of carbon dioxide absorbed). This biomass is a versatile raw material that can be used as fuel or non-combustible products, including bio-oils and proteins, high-value chemicals, food, and fertilizers. The investments have concerned mainly the production of fuel; however, no large-scale production of algal biofuels has been achieved so far. Microalgae present high growth rate and productivity. Many species can use salt or brackish water in photobioreactors, and these applications do not compete with conventional agriculture. Among the disadvantages, there are the high-energy demand for the continuous mixing, for the dehydration of the raw material and for some sort of salt management. Finally, such systems require very wide areas, hard to be found nearby power plants.

CO₂ is also already directly used in commercial processes in its pure form: for example, in the food and beverage industry as a carbonating agent, packaging gas, solvent for flavor extraction and in the decaffeination process. Likewise, CO₂ is used as solvent in dry cleaning and for accelerated greenhouse tomato production. In the pharmaceutical industry other applications can be found, where carbon dioxide can be used as a respiratory stimulant or as an intermediate in the synthesis of drugs, however, if the sources produce high purity CO₂ waste streams, like in ammonia production.

The already mentioned Enhanced Oil Recovery (EOR) or the Enhanced Coal-Bed Methane Recovery (ECBM) are other examples of direct use where CO₂ is exploited to extract crude oil or natural gas from not accessible deposits. The latter is not commercially available while the former has been widely practiced for over 40 years in several oil producing countries (Norway, US, Canada) [56]. The EOR can extract 30-60% over the oil originally available by means of the injection of various agents into the tank. Injected under supercritical conditions, CO₂ mixes with the oil decreasing its viscosity, thus helping to increase the extraction yield. However, it needs to be said that most of the CO₂ comes back to the surface with the oil and some gases are released to the atmosphere.

Lastly, there is the possibility of using CO₂ as a raw material to be converted into chemicals and fuels. This can be achieved using CO₂ molecule as a precursor for organic compounds such as carbonates, acrylates, and polymers through carboxylation or through reduction reactions in which chemicals and fuels such as methane, methanol, syngas, urea and formic acid are produced. The presented research fits precisely in this field of applications. Such processes are challenging because its conversion has a high energy cost and requires highly selective catalysts, since CO₂ is a very stable molecule. Recently, carbon dioxide conversion through catalytic hydrogenation is gaining increasing attention, involving synthesis of dimethyl ether, liquid hydrocarbons, light olefins, and alcohols, essentially through two hydrogenation pathways: methanol reaction and Fischer-Tropsch based hydrogenation. The Fischer-Tropsch process converts, by means of a metal catalysts, carbon monoxide and hydrogen into liquid hydrocarbons at temperatures of 150-300 °C and up to tens of atmospheres. Among the possible synthetic fuels, methanol, octane, and methane may be included. As for methanol, its synthesis process is quite simple and almost energy-neutral, however, the gravimetric energy density is in favor of methane and octane. For transportation, octane is the best

choice given that it is liquid and with a high energy density. In the case of octane, the drawback of the complex synthesis process via reversed water gas shift reaction combined with Fischer-Tropsch synthesis, must be considered. From a practical point of view, methane is the easiest chemical energy carrier to produce with the already mentioned potential.

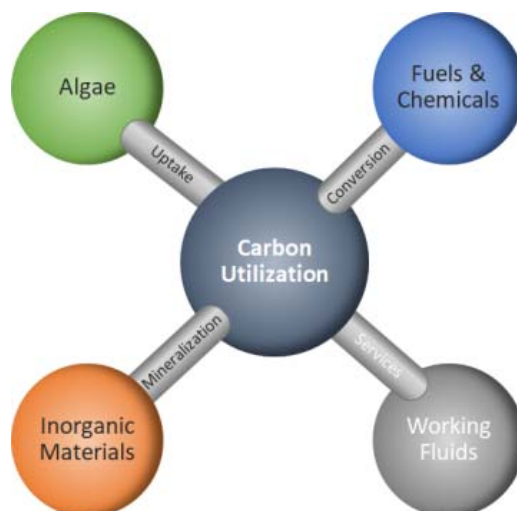
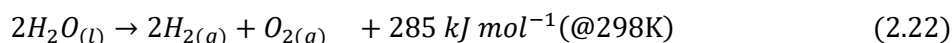


Figure 2.44 Overview of major applications from captured CO₂ [58]

2.5.3 Hydrogen production

The production of hydrogen is based on well-known industrial processes that have been carried out for more than a century. Currently, most of the produced hydrogen derives from fossil fuels, approximately 97%, and, excluding these sources and the nuclear ones, producing hydrogen otherwise may not be economically competitive in the immediate future. However, innovative processes to produce renewable hydrogen are of great interest in the direction of a decrease in the emission of pollutants. Processes from fossil fuels are multiple: steam reforming of methane is the most widely used process covering about 50% of the production. The reaction of natural gas with steam, at temperatures of about 800 °C and pressure around 4 bar, is often accompanied by the water-gas shift reaction, which increases the H₂ content in the syngas stream with efficiency standing at values between 65-85%. Another commercial method is the partial oxidation of hydrocarbons. For this process, the efficiency is estimated at around 50%. A solution between the two previous ones is the autothermal reforming of gasoline and methanol: here fuels react with both steam and air to produce a gas stream with a high H₂ content; the partial oxidation reaction (exothermic) is induced, and the heat is used for the endothermic reforming reaction. Lastly, coal gasification is one of the oldest techniques still having an important role, thanks to the coal availability worldwide: the reaction, carried out in most cases in entrained bed reactors, takes place by mixing at sufficiently high temperatures the coal with air, oxygen, or steam.

The production of hydrogen through water electrolysis, covering presently only 3% of the entire amount of obtained H₂, is possible by means of an electrolytic cell: basically, water molecules, due to the potential difference supplied through an external electric circuit, dissociate as follows:



Hydrogen at the cathode, e.g. the negative pole of the electrolyzer, and oxygen at the anode (the positive pole) are released. Generally, the cathode is made of platinum. The maximum theoretical efficiency (the ratio between the energy value of hydrogen produced and the electricity used) is between 80% and 94%. On the basis of the electrolyte used, there may be:

- alkaline electrolyzers;
- polymer membrane electrolyzers (also referred to as PEM - Proton Exchange Membrane);
- solid oxide electrolyzers (SOEC - Solid Oxide Electrolysis Cell).

A fundamental parameter that is used to distinguish the systems is the operating temperature: alkaline and PEM are low temperature electrolyzers using liquid water and operating at temperatures of 20-100 °C, whereas SOEC are high temperature electrolyzers that operate with water vapor and temperatures of 600-1000 °C [59]. The most established technology, up to the megawatt range, is the alkaline water electrolysis (AEL): the large scale is obtained by combining several modules. The alkaline aqueous solution is essentially a solution of KOH/NaOH, 20-30%, and the electrodes are made of asbestos diaphragm and nickel materials. The high corrosivity of the solutions is one of the main drawbacks with consequent high maintenance costs. The plants last approximately 30 years. The diaphragm separates the cathode and anode: the main limitation is the diffusion of the products through the diaphragm resulting in the formation of flammable mixtures. There are interesting new approaches in the alkaline electrolysis technology such as the anion exchange membranes (AEM) where polymers with anionic conductivity replace asbestos diaphragm. In the PEM water electrolysis technology, solid polysulfonated membranes (Nafion, Fumapem) are used as proton conductors. PEM water electrolysis is one of the most promising methods in terms of sustainability and environmental impact, with compact design, high current density, high efficiency, and fast response. The efficiency of PEM is comparable to the AEL one: about 60-84% while their current density is higher (0.5-2 A/cm² and 0.2-0.4 A/cm², respectively.) The electrocatalysts for PEM electrolysis are noble metals such as Pt/Pd at the cathode and IrO₂/RuO₂ at the anode, this is what makes the process more expensive than alkaline water electrolysis: one of the main challenges in PEM water electrolysis is to reduce the production cost maintaining the high efficiency. More in detail, the PEM costs are around 1300-2200 €/kW while the AEL ones 700-1100 €/kW. Moreover, PEM presents a lower lifespan than AEL. Recently, different authors have made several costs projections that appear to be optimistic: according to them, average costs for alkaline and proton exchange membrane electrolyzers may decrease to below 500 €/kW_{el} in 2050. Increasing automation and production capacities are thought to be the main reasons for the future expected cost decline [60]. Substantial research is also being carried out to improve the PEM components and approach commercial market. So far, the PEM modules applied have capacities up to 10-15 Nm³/h, far less than those of AEL systems, which reach 760 Nm³/h. The scale-up is necessary for the PtG market, for example, where PEM electrolysis is the best choice due to a better dynamic behavior making it preferable for intermittent application. Both PEM and AEL are suitable for high-pressure condition, the former for their compactness, the latter since the compression of liquid water is preferred to the compression of the product gas. Lastly, the solid oxide electrolysis (SOE) got attention due to the conversion of electrical energy into chemical energy along with the production of ultra-pure hydrogen with high efficiency. In the process, conventionally, nickel/yttria stabilized zirconia are used as O₂ conductors. SOE are clearly characterized by faster kinetics because are high-temperature electrolysis (HTEL) systems: this feature results in reduced electrical energy consumption compared to the other systems. HTEL is

generally thermoneutral: the heat produced in the cell is equal to the heat consumed by electrolysis. The main issues of these systems are related to the lack of stability and degradation, drawbacks that need to be solved to make a spread on large scale possible. The three mechanisms are shown in figure 2.45.

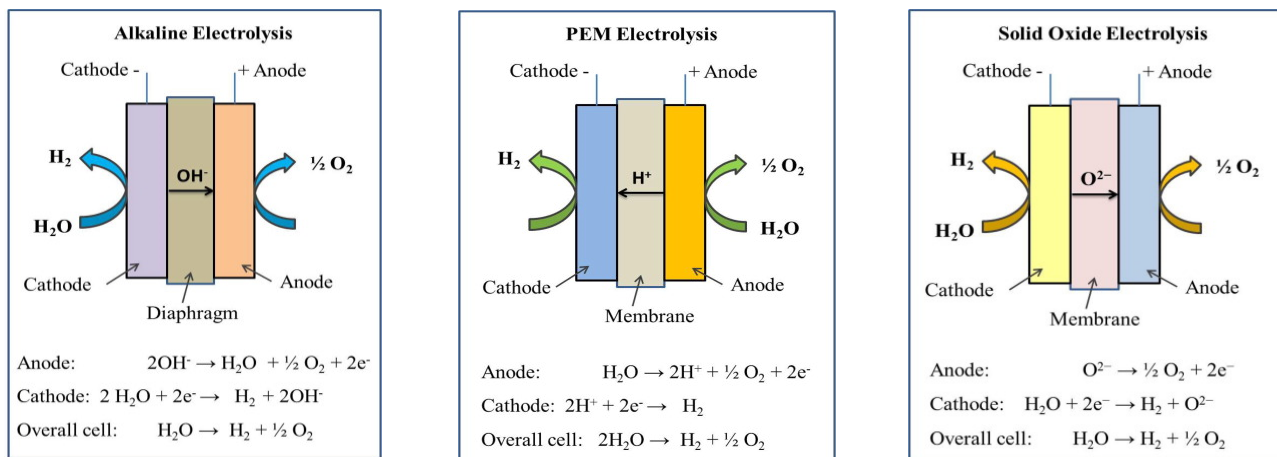


Figure 2.45 Schematic illustration of: Alkaline Electrolyzers (left), PEM (center) and Solid Oxide Electrolysis cell (right) [59]

Biomass is one of the most studied renewable energy sources for a wide range of purposes, including hydrogen production. The hydrogen content in a biomass is around 6%, however, the energy conversion efficiency is quite high (for example about 56% for steam reforming of pyrolysis oil). The two classes of existing biomass-to-hydrogen processes, biological and thermochemical, have already been described for synthetic methane production.

In the research field involving alternative energy, the use of solar radiation to produce fuels is one of the most interesting challenges. Considering hydrogen production from solar energy, the most developed technique is based on the combination of the electrolytic phase with the photovoltaic or solar thermal one, but photochemical and thermochemical systems exist, too. In these systems, metal oxides are applied and frequently CO is also produced, to obtain a mixture to be used for subsequent reactions.

TiO₂ (polarized by the effect of solar radiation) as photocatalyst is used for the photochemical conversion. This technology directly converts solar energy with no intermediate electricity production with theoretical efficiencies of about 26%. However, low absorption capacity of the solar spectrum and high recombination rate of products before their separation and collection, prevented the large-scale application, so far.

The thermochemical process exploits concentrated solar radiation to activate highly endothermic reactions. In a first step, this concentration enables to reach temperatures close to 1800 K and activates a reduction reaction of a metal oxide (figure 2.46). In a second step, the reduced form of the metal oxide reacts exothermically with H₂O and CO₂ so that the metal oxide, H₂ and CO are released. This last step, not needing solar radiation, can be carried out where the produced gas needs to be used. As in the photochemical case, from this type of technology, solar energy is directly transformed with similar theoretical efficiencies reported.

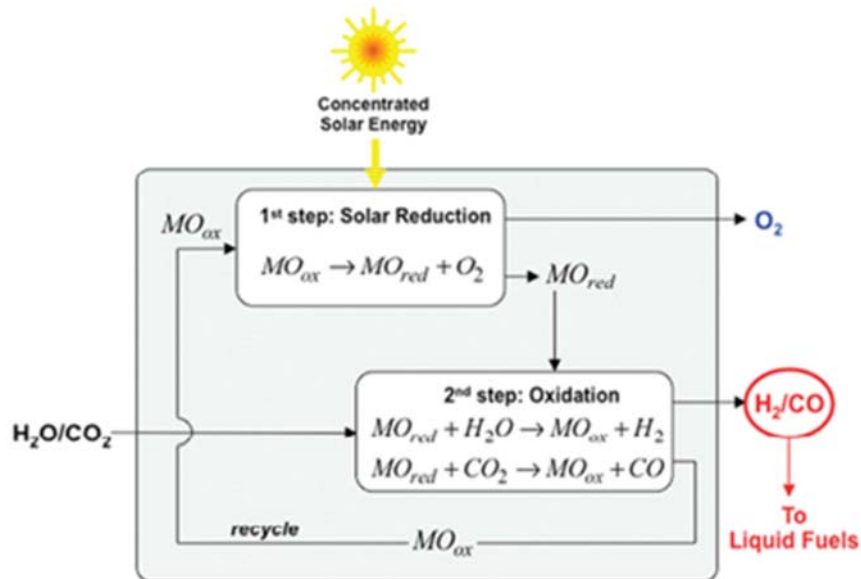


Figure 2.46 Hydrogen production form solar energy: thermochemical system scheme [2]

Recently, the chemical looping technology has been applied by several researchers also to the production of hydrogen. In literature, two categories of processes are found considering the advances in this field: chemical looping reforming (CLR) and chemical looping hydrogen production (CLH). The CLR combines chemical looping and steam reforming process with opportunities especially for industrial applications. The process involves the usual concept of metal oxides that transfer oxygen to the fuel: the difference with respect to chemical looping combustion (CLC) is the desired product that, in the CLR, is syngas. To achieve that, the complete oxidation of the fuel is prevented keeping the air to fuel ratio low. This chemical looping presents the advantage of attaining the heat to produce H_2 without oxygen production, air and carbon fuels mixing and partial consumption of the H_2 produced in the process. Problems regarding erosion by oxygen carriers and heat balance between FR and AR (fuel and air reactors) are its main caveats.

The further chemical looping process proposed, the CLH process, has received attention as a novel technology capable of producing ultra-pure hydrogen without further purification steps and inherent separation of CO_2 . The process should be developed for high-temperature and high-pressure conditions: it should be emphasized that the required high temperatures make this application difficult, even if recent studies have tried to overcome that by coupling the CSP (Concentrated Solar Power) technology to the looping process. In particular, the CLH system consists of two reactors: a water splitting reactor and a reduction reactor. In the reduction reactor, a gaseous fuel (CH_4 , H_2 , CO , C_nH_{2n+2} , or syngas) reacts with the metal oxide; the metal particles released are transported to the water splitting reactor and react with steam producing hydrogen and metal oxide particles, recycled back to the reduction reactor.

The reactions can be simplified as follows:

- water splitting reaction: $M+H_2O \rightarrow MO+H_2$
- reduction reactor: $4MO+CH_4 \rightarrow 4M+CO_2+H_2O$
 $MO+H_2 \rightarrow M+H_2O$
 $MO+CO \rightarrow M+CO_2$

with M: metal, MO: metal oxide. The figure 2.47 reports the two processes described above.

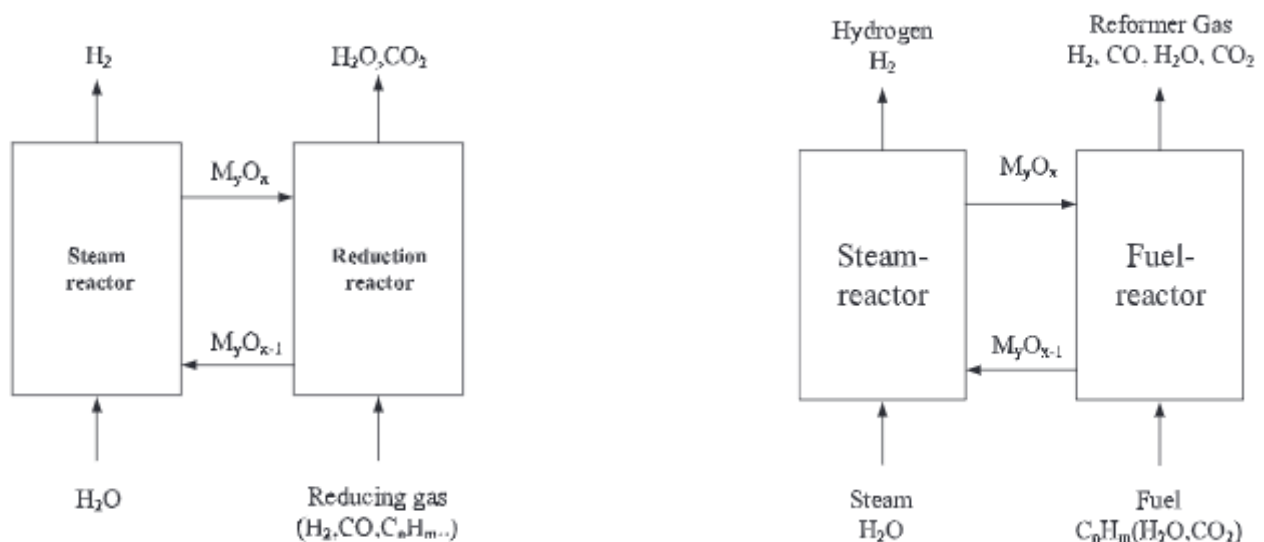


Figure 2.47 Schematic diagram of the chemical looping hydrogen production (left) and CLR for hydrogen and syngas production (right) [61]

3 Sorption Enhanced Methanation

3.1 Sorption Enhanced concept applied to methanation reactions

The sorption enhanced reaction concept is well known, applied, and investigated in literature. This application is based on Le Chatelier's principle according to which, the conversion and the rate of forward reaction in an equilibrium-limited reaction can be enhanced by selectively removing some of the products from the reaction environment [62]. The categories of reactors that can be used are numerous: fixed bed, continuous-countercurrent moving-bed, membrane reactors. These latter perform the products removal by means of selective permeation through the reactor wall. When a catalyst is required in a chemical reactor, a mixture sorbent-catalyst is used. The sorbent has to remove selected reaction products by physisorption or chemisorption, needing, in general, to be periodically regenerated in situ by using pressure or thermal-swing adsorption. The concept described above was also proposed combined to methanation reaction to improve the use of the excess heat provided by the reaction and to reach high SNG grade. In literature, it is mostly proposed as a biogas upgrade process, converting the CO₂ of raw biogas into methane using hydrogen from renewable energy sources. The main efficiency loss of the Sabatier process is the heat release, equal to approximately 17% of the heating value. The strong exothermicity entails a theoretical high reaction yield at low temperatures, however in these conditions the reactions are kinetically limited. As for the pressure, methanation reactions proceed with a net decrease of the moles number, so that high pressures promote the conversion. The concept is, hence, proposed mainly with the aim of achieving good performances possibly at low pressures, overcoming the thermodynamic constraints. Theoretically, the sorption enhanced reaction can be carried out in a catalytic bed by adding a sorbent material to the catalyst, however, in the published papers, the Le Chatelier principle is applied mainly using the so-called sorption enhanced catalysts (or bi-functional catalysts) to increase the kinetics and yield by local water absorption at the reaction centers. The gas-solid thermodynamics determines the adsorption and desorption of the species and, consequently, the kinetics of the catalyst: through a material with a sorption function, it is possible to tailor the coverage of the reactions sites by removing the produced water using a sorbent with a high-water affinity [63].

3.2 SEM as a SNG upgrading process

Sorption-enhanced methanation was studied relating to methanation used as a SNG upgrading process by Walspurger et al [64]. The authors studied the extent of the improvement in methane quality that may be achieved, as well as the limits of the process. The sorption enhanced methanation reaction process showed unique performances for high grade SNG production at low pressure using commercial materials (figure 3.1).

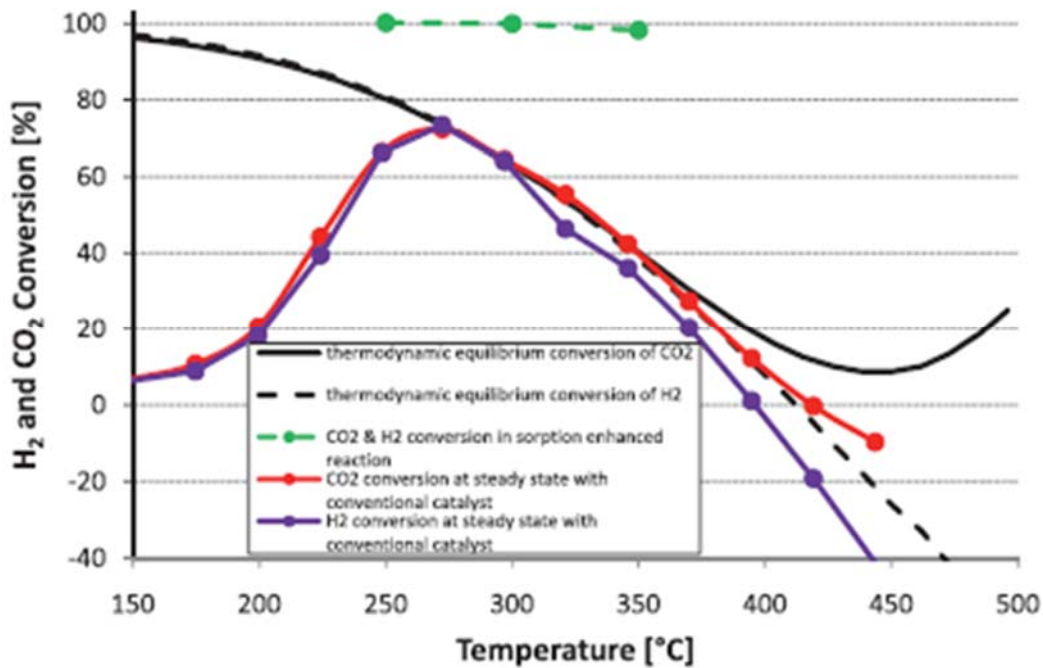


Figure 3.1 Walspurger et al. [64] SEM concept applied to CO₂ methanation

They analyzed the thermodynamics of the CO₂ methanation in ASPEN Plus to identify the feed characteristics and the target performance. The streams conditions and the recycle ratio considered are those typically found in industrial process (CO₂ captured using amine absorption at 1.6 bar and 40 °C, the hydrogen produced by an electrolysis process at 1 bar and 40 °C). The target was to have, downstream the catalytic fixed beds section, SNG of sufficient quality for a certain gas grid (specifications: CO₂ < 3%, H₂ < 0.5%, CO < 0.5%, H₂O < 90 ppm pressure of 60 bar). The reactors temperature ranges were fixed considering the characteristics of commercial catalysts: maximum temperature is 650 °C, inlet temperatures of 300, 250 and 220 °C, respectively. The pressure was evaluated in a sensitivity study up to the grid pressure of 60 bar. The modeled section consisted of three fixed bed methanation reactors with a recycle from the second to the first reactor and intermediate cooling: for modelling the influence of in situ water removal, the third reactor was considered either as a conventional reactor or as a sorption-enhanced reactor. It was seen from the simulation that a water-removing reactor in place of the third conventional reactor led to a H₂ level in the SNG significantly lower and that the gas grid specifications can be matched at much lower operational pressure. Figure 3.2, disclosing the theoretical hydrogen concentration in the dry stream at the outlet of the section as a function of the operational pressure, reports these results.

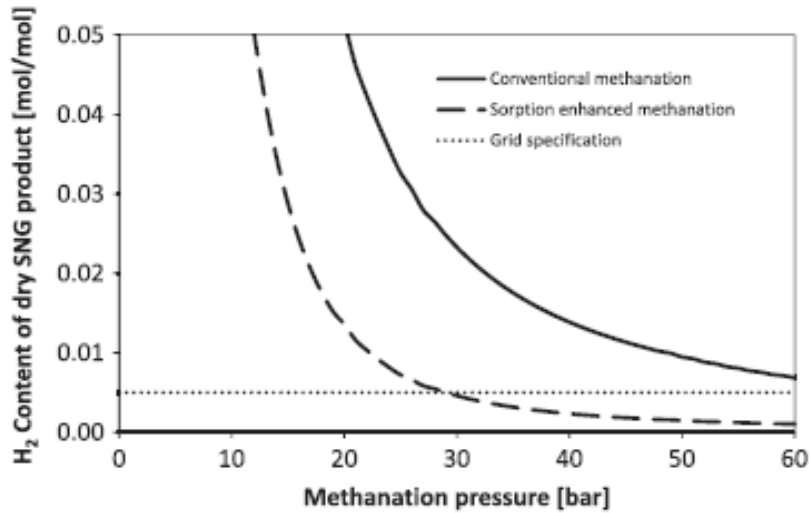


Figure 3.2 H₂ level in SNG produced for the conventional and for the sorption enhanced methanation [64]

The authors pointed out that operating the methanation at relatively low pressure may determine a significant compression energy saving, up to 60% at 5 bar and even more, at lower pressure. The compression energy duty represents 10% of the energy content of the SNG when the mixture of CO₂ and H₂ from 1 bar is compressed to 60 bar. The gaseous reactants are quite commonly available at a pressure of 1 bar: for instance, in the methanation from biomass gasification where the streams, from the indirect gasification process, are supplied at pressure <10 bar. Below 10 bar, the compression energy duty may be reduced to less than 6%. More generally, the savings are significant for conditions between 5 and 20 bar compared to operations at 60 bar. The simulation model also showed that the temperature rise is quite high (up to about 600 °C): for this reason, the possibility of implementing a sorption enhanced step in place of a conventional third reactor appeared a reasonable option not relying on a complex and expensive isothermal reactor. In fact, considering an operational pressure of 25 bar, the inlet composition of a sorption enhanced reactor downstream two reactors in series with a recycle loop, would be able to allow only a limited temperature rise during conversion. However, considering pressures below 10 bar, the authors found out that an amount of CO₂ and H₂ remains to be converted in a sorption-enhanced reactor, since this amount would lead to an excessive temperature rise to consider this type of process as third step to carry out in a fixed bed reactor.

3.3 State of the art of the materials to perform SEM

Walspurger et al. [64] investigated experimentally SEM in their work, too. For the adsorption/desorption tests, Merck zeolite 4A was tested. As for the adsorption, more specifically, the sample consisted of a mix of a Ni-based catalyst and zeolite 4A. The catalytic test revealed that at high operating temperature (above 400 °C.), the low operating pressures promote even the consumption of methane. Either way, they demonstrated that for conversion ranges corresponding to adiabatic temperature rise of up to 200 °C and for low pressures, sorption enhanced methanation potentially overcomes the conversion constraints found when conventional methanation is carried out and high methane purity and low hydrogen content are required. The concept in the study was based on a temperature swing adsorption cycle using a purge gas. The experimental campaign showed that commercial materials are capable of operating in cyclic sorption enhanced conditions at the temperature range of interest. The breakthrough water capacities were 1.52 mmol/g, 1.31 mmol/g and 1.07 mmol/g at 250, 300 and 350 °C respectively. In contrast with the adsorption, the regeneration temperature had not a large effect on the uptake capacity of the sorbent. The regeneration temperature value could be close to those of the operating conditions, but the choice and availability of a dry purge gas is crucial to keep the energy requirement low (this gas could be the H₂ produced by the electrolyzer or even CO₂ if the catalyst stability was not affected). The energetic performance may be optimized by the heat integration with the exothermic methanation reaction, the development of bifunctional adsorbent/catalyst materials also allowing for the least temperature swing possible and, lastly, a proper process configuration. All these aspects will be the keys for the translation of these concepts in a cost effective SNG upgrading method. Regarding the conceiving of bi-functional materials, this novelty would solve another aspect pointed out by these experimental results that is the importance of improving the mass transfer rate between the catalytic sites and the adsorbent sites. In this respect, Borgschulte et al. [63] moved forward in this research field. They showed the improvement of CO₂ methanation by sorption enhanced catalysis, studying Ni particles on zeolites 5A. Sorption catalysts were discussed considering operating and reaction mechanisms, providing a whole range of interesting implications for catalysis. Catalysts with a load of Ni approximately equal to 6%_{wt} showed the best performance. Figure 3.3 reports the schematic structure of a Ni based sorption catalyst and a comparison with a conventional catalyst in terms of the free energy of reactant and products.

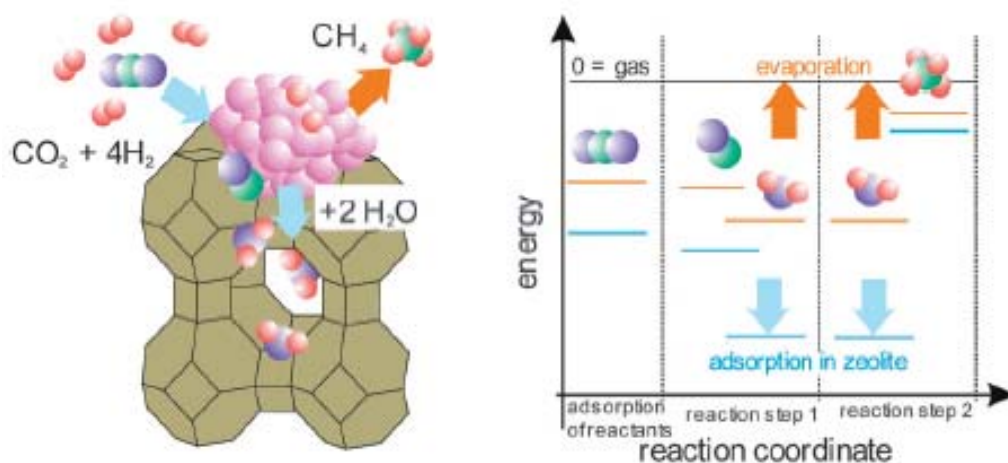


Figure 3.3 Structure model of a sorption catalyst based on Ni particles on zeolites (left); free energy on the conventional catalyst (orange) and on a sorption catalyst (blue)

The sorption catalyst was compared to a commercial one to evaluate catalytic performance; catalytic properties of the former are only slightly improved: maximum conversion at slightly lower temperatures and lower CO release. The authors demonstrated the power of the sorption effect by the transient kinetics measurements: initially the gas contains about 100% methane; when the amount of water adsorbed exceeds the zeolites sorption capacity, water leaves the reactor and, simultaneously, the reaction methane yield decreases. The reactor showed a 100% selectivity for a limited time, after which regeneration is required. The obtained materials can be readily applied in biogas upgrade process. Moreover, zeolites can be tailored to exhibit defined chemical properties (surface acidity, pores size, etc.) and thus improve sorption properties of the presented sorption catalysts. Later, Delmelle et al. also considered zeolites 13X in addition to 5A [65]. Zeolite 13X showed an operation time three times higher than the 5A. This can be explained by its higher water sorption capacity especially at temperatures higher than the room one. Both catalysts presented the same CO₂ conversion in conventional CO₂ methanation, which leads to think that there is a sole performance dependence on the metallic nickel phase. In fact, in general, the support can influence the performances but, in this case, although Zeolite 13X has a higher Si/Al ratio and therefore lower acidity than the zeolite 5A, the CO₂ conversion levels are similar for the two supports considered. 5Ni/13X catalyst (5Ni stands for 5%_{wt} of Nickel) exhibited an improved performance. Zeolites LTX larger pores (9 angstrom compared to 5 of zeolite LTA 5A) enable better air and water transport and therefore also more efficient catalyst regeneration under oxidizing conditions, instead of reducing ones, that are needed in real systems to avoid deactivation due to coke and/or sulphur poisoning. This result can be explained by the fact that oxygen and nitrogen molecules have sizes and weights, which are the same order of magnitude of water molecules so that collisions between these gas species may be energetically more effective and, thus, air carries out the water from the zeolites better than hydrogen. For the experiments, the samples were prepared by wet impregnation and Nickel nanoparticles resulted homogeneously distributed throughout the support with sizes in the range 20-30 nm. They found out that the 5Ni/13X catalyst is active at 300 °C while as for Ni particles on zeolite 5A, most of the nickel oxide is reduced above 500 °C. This is a significant result for the choice of the catalyst, based on the considered temperature of the application.

Still Delmelle et al., more recently (2018) [66], evaluated water diffusion aspects in a sorption-enhanced methanation catalyst. Water diffusion in the zeolite appeared the rate-limiting step in both methanation and drying phases. Considering the same methanation time, samples under cyclic treatments (methanation/drying) exhibited carbon contents about 55% higher than the ones subjected to continuous methanation conditions. This may be a specific degradation phenomenon, which is not a deactivation phenomenon. Intermediates and products are generated in the zeolite during methanation, blocking, certainly, also the pores: the consequence is a decrease in the water diffusion during the drying (diffusion coefficient decreases of about 40% after around 40 cycles). This decrease affects the regeneration because increases the water diffusion path lengths whereas it has no effect on the catalytic performance. Drying in oxidizing conditions may be a good solution to this degradation. A noteworthy paper on this subject by Agirre et al. [67] was published in 2021. The authors studied the most suitable parameters to operate water sorption simultaneously with methanation in fixed bed reactors; the trend is trying to allow the lowest possible temperature corresponding to high selectivity to methane and low CO production. They found an optimum temperature of 290 °C and 15 bar of total pressure since the commercial catalyst applied (KATALCO-57-4Q, Johnson Matthey) was active above 275 °C. The hydrogen conversion was around 92-94% with very high selectivity (no CO

detected). As for the sorption experiments, these authors considered three materials: CaO, La₂O₃, zeolites 4A. This last one showed a very quick sorption and saturation with, therefore, a very short transient period: this is a critical issue if combined to methanation kinetics. At room temperature the zeolites adsorbed around 11% (these data coincide with those of numerous other sources) but strongly decreased with increasing temperature and showed a perfect reversibility of water sorption. As for CaO, the best result with a view to methanation was that it adsorbs water up to 350 °C, making this sorbent absolutely promising for the application that is being examined. CaO sorbent behaves, obviously, different to zeolites because chemisorption is expected to occur. The room temperature sorption in a first cycle is higher than that for zeolites but since the second cycle the capacity decrease, the mechanisms seem to change, and the sorption-desorption processes are not completely reversible in contrast to zeolites. The most recent works focus mainly on SEM applied to CO₂ methanation. In a work published in 2021 [68], four different bifunctional catalyst-sorbent materials were studied for CO₂ methanation carried out in fixed beds. In particular, the authors found that the best performing material was a 5% Nickel catalyst on zeolites 13X (already known to be a better support for SEM with respect to 5A) with the addition of 2.5% of Cerium. This material showed 100% selectivity and conversion at temperatures as low as 180 °C and good stability during the cycles.

Table 3.1 summarizes the main test conditions applied in CO₂ SEM publications using the materials reviewed in this section.

^a Catalyst/Sorbent	Feed H ₂ :CO ₂ :N ₂ :CH ₄	GHSV	^b mass (g)	T _{SEM} (°C)	pressure (bar)	^c H ₂ O uptake (mmol/g)	^d T _{REG} (°C)	Ref.
Bifunctional materials								
5Ni/5A	400:50:0:0	1000/h	13	170	1.2	N.A.	N.A.	[63]
Ni/Al ₂ O ₃ mix 4A	9.9:2.5:6:81.6	2500 mL/g _{cat} /h	3.6	250-300-350	1	1.52-1.31-1.07	350-450	[64]
5Ni/5A	4.05:1:0:0	92/h	250	300	1	N.A.	300	[65]
5Ni/13X	4.05:1:0:0	92/h	250	300	1	N.A.	300	[65]
5Ni2.5Ce13X	10:2.5:6:81.5	923 mL/g _{cat} /h	6.5	260-280-300-320	1	1.65-1.4-1.1-1	450	[68]
5Ni13X	9.9:2.5:6:81.6	714 mL/g _{cat} /h	8.4	280-300-320	1	1.3-1.1-0.9	450	[68]
5Ni5A	9.9:2.5:6:81.6	714 mL/g _{cat} /h	8.4	280-300-320	1	0.95-0.8-0.75	450	[68]
5NiL	9.9:2.5:6:81.6	714 mL/g _{cat} /h	8.4	300-320	1	0.5-0.3	450	[68]
Commercial Katalco 57-4Q catalyst mixed with sorbent materials								
12.6Ni(CaO/Al ₂ O ₃)/4A	295.5:90.6:150:0	382.9 NmL/g _{cat} /min	1.4	290	15	1.39	N.A.	[67]
12.6Ni(CaO/Al ₂ O ₃)/La ₂ O ₃	295.5:90.6:150:0	382.9 NmL/g _{cat} /min	1.4	290	15	0.5	N.A.	[67]
12.6Ni(CaO/Al ₂ O ₃)/CaO	295.5:90.6:150:0	382.9 NmL/g _{cat} /min	1.4	290	15	4	N.A.	[67]

^athe number before the active phase (Ni) refers to metal loading (%wt).

^bfor non bifunctional materials it refers to catalyst mass and the length of catalytic/adsorbent bed is fixed to 10 cm.

^cthe H₂O uptake for non bifunctional materials are obtained in a Thermogravimetric Analyzer (not under SEM conditions).

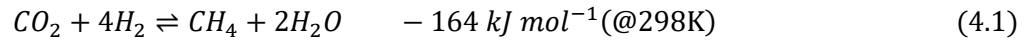
^dT_{reg} is the regeneration temperature.

Table 3.1 Summary of the different materials used in CO₂ sorption enhanced methanation investigations reported in the literature. Adapted from [68]

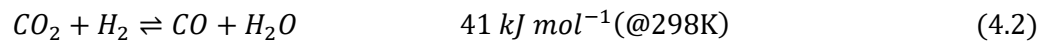
4 CO₂ SEM: thermodynamic analysis

4.1 Thermodynamics of conventional CO₂ methanation

Several studies in literature deal with the thermodynamics of carbon oxides methanation [69]. As for the methanation of CO₂, the following equation describes the reaction:



The process is characterized by a volume contraction of 40% and the conversion releases 164 kJ per mole: 1.8 kW of heat for each m³ of methane (STP) produced per hour. Equilibrium of reaction is influenced by pressure and temperature: high pressures favor the production of methane, by contrast, high temperatures limit that. Figure 4.1 shows the typical mole fractions at equilibrium calculated considering a stoichiometric H₂/CO₂ molar ratio of 4: CH₄ and H₂O are the main products at relative low temperatures (200-250 °C). Above 450 °C, CO by-product increases due to the reverse water gas shift reaction:



For high temperatures, also unreacted CO₂ and H₂ increase along with a CH₄ decrease. CO₂ mole fraction is maximum at a temperature that exceeds 550 °C and then decreases because the RWGS reaction becomes predominant. An important point is that no carbon deposition is predicted to occur under these conditions. CO₂ methanation is often thought to be describable as a series of reactions involving firstly the reversed water-gas shift reaction, followed by CO methanation in the presence of steam with H₂/CO/H₂O ratio of 3/1/1; the presence of H₂O may explain why no carbon deposition is found.

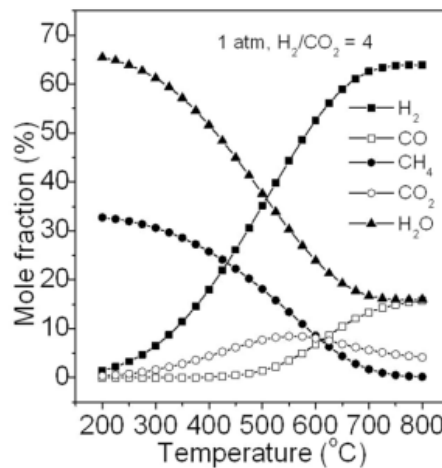


Figure 4.1 Products mole fraction at equilibrium [69]

Figure 4.2 shows the effects of pressure and temperature on CO₂ methanation. As already anticipated, CO₂ conversion decreases with temperature and increases with increasing pressure at temperatures below 600 °C (figure 10-a): at 1 atm and beyond 600 °C the conversion increases, mainly because the RWGS above 600 °C consumes CO₂.

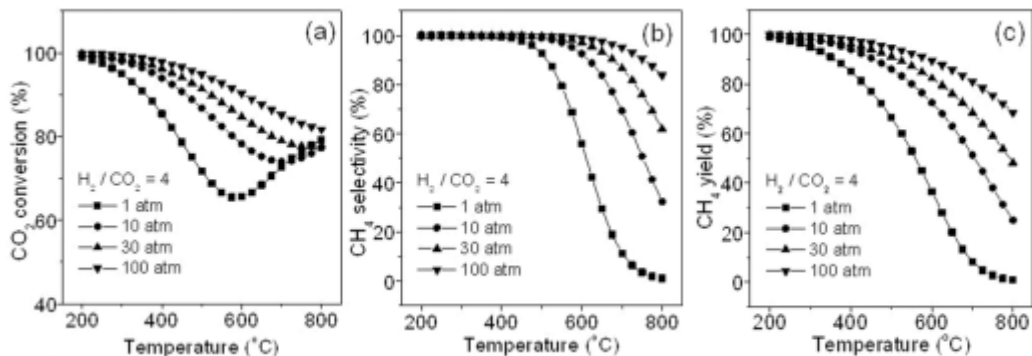


Figure 4.2 Effects of pressure and temperature on: (a) CO₂ conversion, (b) CH₄ selectivity and (c) CH₄ yield [69]

The performance indicators are remarkably affected by the H₂/CO₂ ratio: figure 4.3 describes this effect on CO₂ methanation. High H₂/CO₂ ratio generally leads to high CO₂ conversion and CH₄ selectivity also at 1 atm. The behavior at H₂/CO₂ equal to 2 is different and CO₂ conversion achieves only 50 and 70% at 1 and 30 atm and CH₄ maximum selectivity is 73% and 88% at 1 atm and 30 atm, respectively. As for the CH₄ yield, for the H₂/CO₂ ratio equal to 2, this is only 45% at 30 atm. Lastly, when H₂/CO₂ ratio is 2, significant carbon deposition (up to 50%) is found below 500 °C even at 30 atm. In conclusion, to obtain a high CH₄ yield and avoid carbon deposition, H₂/CO₂ ratio should not be lower than 4 even at 30 atm.

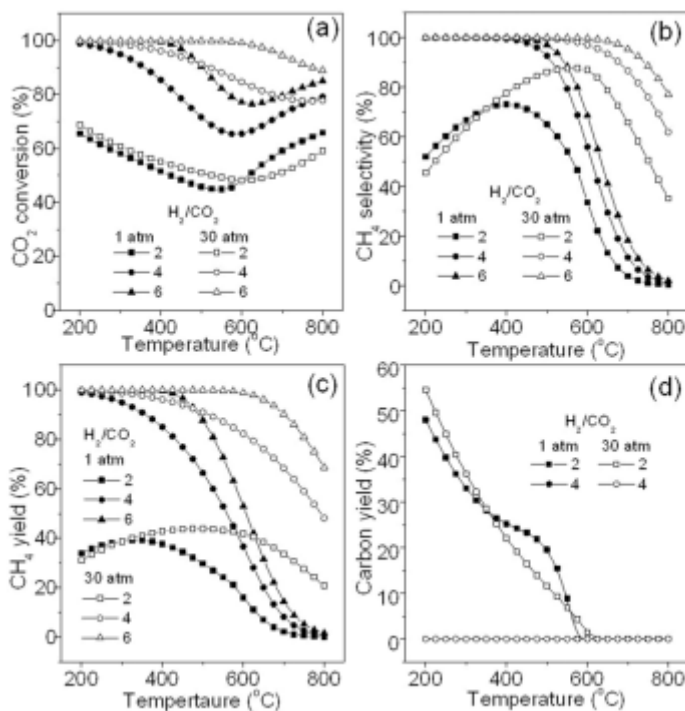


Figure 4.3 Effect of different H₂/CO₂ ratios on: (a) CO₂ conversion, (b) CH₄ selectivity, (c) CH₄ yield and (d) carbon yield [69]

4.2 Present analysis methodology

CO₂ methanation thermodynamics under SEM conditions was not previously investigated in the literature. To study the thermodynamics of pure CO₂ sorption-enhanced methanation, at low pressures in order to optimize the operating conditions of such a process, equilibrium calculations were performed in this work. The compositions of a reactive system at the equilibrium can be calculated following two methods. In the stoichiometric method, the reactions involved in the whole process need to be known and the calculation proceeds via the identification of the relevant independent reaction equilibrium constants, solving the system of these equilibrium equations combined to the material balance equations on the different chemical species. The second method (non-stoichiometric method) involves the minimization of the Gibbs free energy of the system, a function that has its minimum value at chemical equilibrium. This kind of calculation only requires the definition of the chemical species of interest rather than the exact knowledge of all the reactions involved. For complex systems, this latter method is clearly preferred. Mathematically, the solution is achieved by means of a constrained minimization technique; the constraints are the conservation of the elements present in the system. The technique was implemented in MATLAB environment using a home-made code and the thermodynamic data base reported in [70].

In particular, the total Gibbs free energy of a system is defined as:

$$G_T = \sum_{i=1}^N n_i \mu_i \quad (4.3)$$

where n_i are the molar flow rates and μ_i the chemical potentials of species i . In turn, μ_i is:

$$\mu_i = \Delta G_{f_i}^0 + RT \ln \left(\frac{f_i}{f_i^0} \right) \quad (4.4)$$

In this last equation, $\Delta G_{f_i}^0$ is the Gibbs free energy of formation of species i , R the ideal gas constant, T the absolute temperature, f_i the fugacity and f_i^0 the standard gas fugacity. For the gas phase:

$$f_i = y_i P \varphi_i \quad (4.5)$$

$$f_i^0 = P^0 \quad (4.6)$$

where y_i and φ_i are the molar fraction and the fugacity coefficient of the species i , respectively, P the total pressure and P^0 the standard total pressure.

Finally, the function to be minimized is:

$$f_{obj} = \sum_{i=1}^N \left[n_i \left(\Delta G_{f_i}^0 + RT \ln \left(\frac{y_i \varphi_i P}{P^0} \right) \right) \right] + n_c \Delta G_{f_{C(s)}}^0 \quad (4.7)$$

In the last term of the equation, n_c is the molar flow rate of the only solid that is expected to be found: carbon and $\Delta G_{f_{C(s)}}^0$ is its standard Gibbs free energy of formation.

The MATLAB *fmincon* command is used purposely to find the local minimum of a non-linear constrained problem. As already indicated, the constraints in our system are the material balances on the elements present.

The syntax is:

$$x = \text{fmincon}(f, x_0, A, b, A_{eq}, b_{eq}, l_b, u_b)$$

$$\begin{cases} \min f(x) \\ Ax \leq b \\ A_{eq}x \leq b_{eq} \\ g(x) \leq 0 \\ h(x) = 0 \\ l_b \leq x \leq u_b \end{cases}$$

where f is a scalar function, x , x_0 , b , b_{eq} , l_b , u_b are vectors, A , A_{eq} are matrices and g and h are vector functions (x_0 is the initial point, which the user needs to provide).

When using the non-stoichiometric approach, the choice of all possible species (trace amount species can be neglected) to be accounted for, is crucial. In this work, these major species can be considered: CO_2 , H_2 , CH_4 , CO , H_2O , C (solid carbon).

At the conditions analyzed, higher molecular weight hydrocarbons were neglected, and the gaseous species were considered as ideal gases (pressure below 10 atm) with their fugacity coefficients thus set to unity. The list of the possible reactions involved is reported below to better analyze the thermodynamic results, though they are not necessary to perform the minimization technique.

Reaction #	Formula	$\Delta H_{298\text{ K}}$ (kJ mol ⁻¹)	Description
1	$\text{CO}_2 + 4\text{H}_2 \leftrightarrow \text{CH}_4 + 2\text{H}_2\text{O}$	-165.0	CO_2 methanation
2	$\text{CO} + 3\text{H}_2 \leftrightarrow \text{CH}_4 + \text{H}_2\text{O}$	-206.2	CO methanation
3	$\text{CO}_2 + \text{H}_2 \leftrightarrow \text{CO} + \text{H}_2\text{O}$	41.2	Reverse water-gas shift
4	$2\text{CO} + 2\text{H}_2 \leftrightarrow \text{CH}_4 + \text{CO}_2$	-247.3	Reverse dry reforming of CH_4
5	$2\text{CO} \leftrightarrow \text{C} + \text{CO}_2$	-172.4	Boudouard reaction
6	$\text{CH}_4 \leftrightarrow 2\text{H}_2 + \text{C}$	74.8	CH_4 cracking
7	$\text{CO}_2 + 2\text{H}_2 \leftrightarrow \text{C} + 2\text{H}_2\text{O}$	-90.1	CO_2 reduction
8	$\text{CO} + \text{H}_2 \leftrightarrow \text{C} + \text{H}_2\text{O}$	-131.3	CO reduction

Table 4.1 Reactions involved in the CO_2 methanation process

Calculations for the thermodynamic analysis were carried out with two main important targets: discussing the possible carbon deposition, which may be more significant due to H₂O removal, and the suitability of the product compositions for the injection into the natural gas grid.

For the analysis, the inlet conditions considered were:

- a stoichiometric feed (H₂/CO₂ = 4 on a molar basis)
- a feed with an excess of hydrogen.

The inlet moles were translated into the total available moles of oxygen, hydrogen and carbon elements constituting the constraints in the mathematical procedure. The moles of H₂O captured during SEM were converted into a certain number of moles of oxygen and hydrogen subtracted from the total available pool. The maximum number of moles of H₂O that could be generated at complete conversion of the limiting reactant and, consequently, the maximum possible subtracted amount, are two times the inlet moles of CO₂ (which is always the limiting reactant considering the evaluated conditions). A water removal fraction was introduced:

$$R_{H_2O} = n_{H_2O,cap}/2 \cdot n_{CO_2,in} \quad (4.8)$$

The water removal fraction equal to 0 represents traditional methanation, if it is equal to unity, the maximum number of moles of water that can be generated from the complete conversion of the limiting reactant, are captured. The intermediate cases represent partial steam capture conditions.

In our system only carbon, oxygen and hydrogen elements are present so a convenient way to represent carbon deposition boundaries is the use of ternary diagrams. They report the molar fraction of the three elements in the gas phase and are useful also because if the feed composition is fixed it means that the ratio of the three elements is fixed and this point does not change with the conversion unless carbon is formed or water is removed: in these cases, in fact, elements are subtracted from the gas phase. This fixed ratio of the three elements completely determines if carbon will form or not [71].

In figure 4.4 the shaded area includes all the theoretically possible gaseous compositions of the system (the five gaseous species considered in this work, CO₂, H₂, CH₄, CO, H₂O, are all found on the axes of the diagram, consisting of only one or two elements). A feed of H₂ and CO₂ is a point on the line connecting these two species on the diagram. For example, the point SF in fig.4.4 indicates the stoichiometric feed and lies at the intersection between the lines connecting H₂-CO₂ and CH₄-H₂O (methanation reaction products). It should be noted that the lever rule can be used in these diagrams for calculations.

The deposition boundaries at certain temperatures and pressures are curves (isotherms) dividing the shaded area into two zones. The upper zone is where carbon is generated. These isotherms represent all the ratios of CHO elements in the gas phase which are in equilibrium with solid carbon at that temperature and pressure.

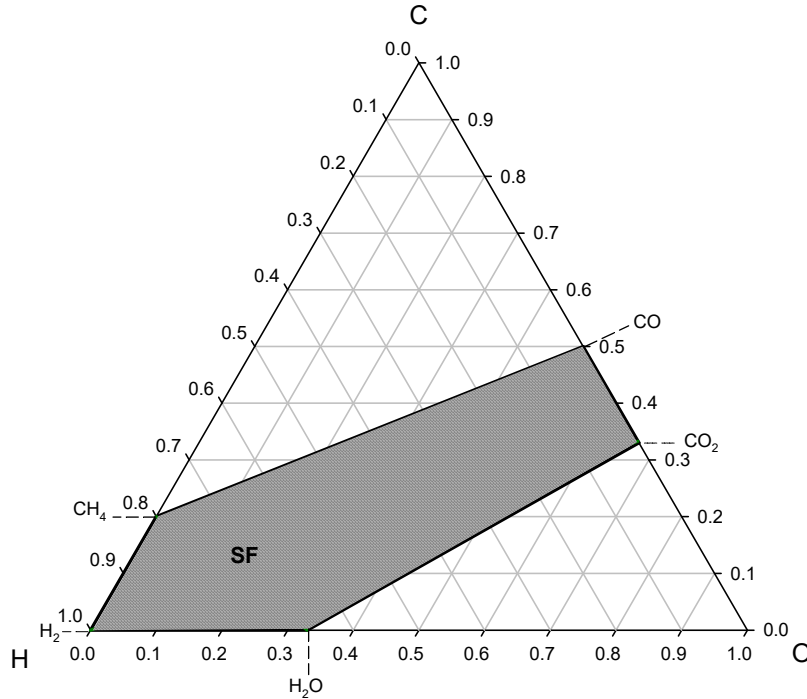


Figure 4.4 CHO ternary diagram with the possible gaseous compositions in the system (shaded area) and the stoichiometric feed (point SF)

The typical performance indicators for the methanation were introduced: total CO₂ conversion, selectivity and yield referred to products containing carbon ($i = \text{CH}_4, \text{CO}, \text{C}$) (4.7, 4.8 and 4.9 respectively):

$$X_{\text{CO}_2} = (n_{\text{CO}_2,\text{in}} - n_{\text{CO}_2,\text{out}})/n_{\text{CO}_2,\text{in}} \quad (4.9)$$

$$S_i = n_{i,\text{out}}/(n_{\text{CO}_2,\text{in}} - n_{\text{CO}_2,\text{out}}) \quad (4.10)$$

$$Y_i = n_{i,\text{out}}/n_{\text{CO}_2,\text{in}} \quad (4.11)$$

where, obviously, $Y_i = S_i \cdot X_{\text{CO}_2}$.

As SNG quality indicator, the dry gas content of the main contaminants is used here, considering the most stringent European limitations: CO₂ < 2.5%, CO < 0.5%, and H₂ < 2% [72, 73].

Two pressures were set for the analysis, 1 and 10 atm.

4.3 Results and discussion

By way of example, for two H₂O removal fraction values, $R_{H_2O} = 0$ and 0.5, figures 4.5 and 4.6 report the equilibrium mole fractions and the main performance indicators, respectively, as a function of temperature for the two pressures considered. In fig. 4.5, the total species mole fractions are reported, including solid carbon (these total mole fractions coincide with the gas phase mole fractions only when no solid carbon is formed). As for traditional methanation ($R_{H_2O} = 0$), results have already been reported before [69, 72, 74]. Briefly commenting, CO₂ conversion is 100% at 200°C, decreasing with the temperature in the range considered up to 600°C. Selectivity to methane decreases above certain temperatures (~400°C at 1 atm, ~500°C at 10 atm) due to the formation of CO by the reverse water-gas shift reaction. Methane and steam are the main species at low temperature and the performance indicators improve when passing from 1 to 10 atm. No carbon is formed at both pressure levels when a traditional methanation is considered: the produced steam can suppress deposition of carbon.

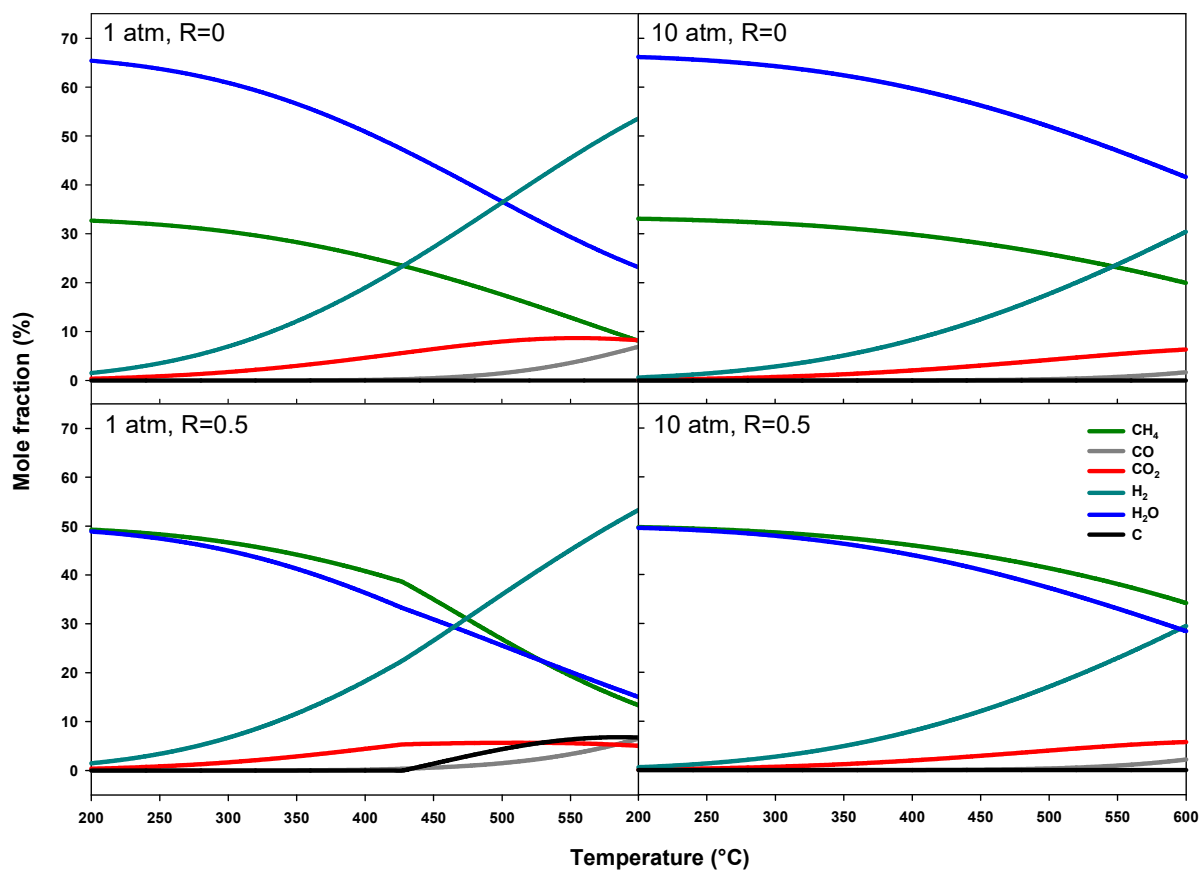


Figure 4.5 Calculated equilibrium mole fractions as a function of temperature, at two pressures (1 and 10 atm) and at two H₂O removal fraction values ($R_{H_2O} = 0$ and 0.5)

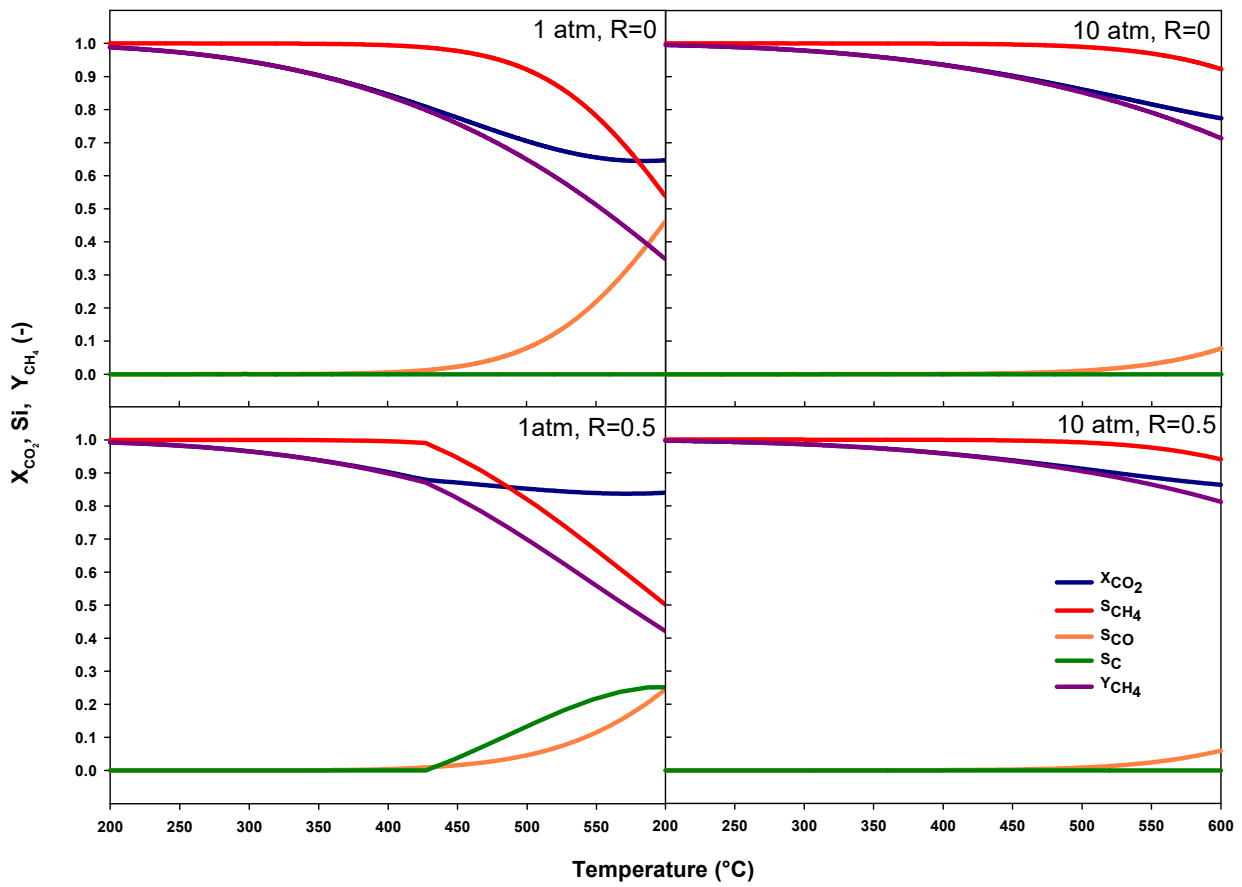


Figure 4.6 Calculated performance indicators as a function of temperature, at two pressures (1 and 10 atm) and at two H₂O removal fraction values (R_{H₂O} = 0 and 0.5)

Considering half of the maximum formable steam captured ($R_{H_2O} = 0.5$), the first visible effect is an appreciable increase in the CO_2 conversion, especially at higher temperature and lower pressure, the main reason to perform SEM. On the other hand, no carbon forms at 10 atm. At 1 atm carbon starts to form above $\sim 430^\circ C$, inducing a sharp decrease of the selectivity to methane. It may be interesting to point out that increased formation of carbon is partially compensated by a decreased formation of CO at this pressure level, since a decrease in available steam would enhance both carbon formation by CO_2/CO reduction reactions and CO consumption by methanation (reactions 7-8 and reaction 2 of the table 4.1, respectively).

The carbon deposition boundaries are depicted in the range 200-600°C at the two pressure levels of 1 atm and 10 atm in figures 4.7 and 4.8, respectively. In these diagrams the two operating points representing traditional CO_2 methanation with stoichiometric feed (SF, $R_{H_2O} = 0$) and SEM condition with half of the maximum producible steam removal (HR, $R_{H_2O} = 0.5$) are displayed. The point SF is located at the intersection between the line connecting H_2 and CO_2 and the line connecting the methanation products while the HR point is located on the line connecting CH_4 and H_2O , in an intermediate position between the SF point and the CH_4 point (which corresponds to the condition $R_{H_2O} = 1$).

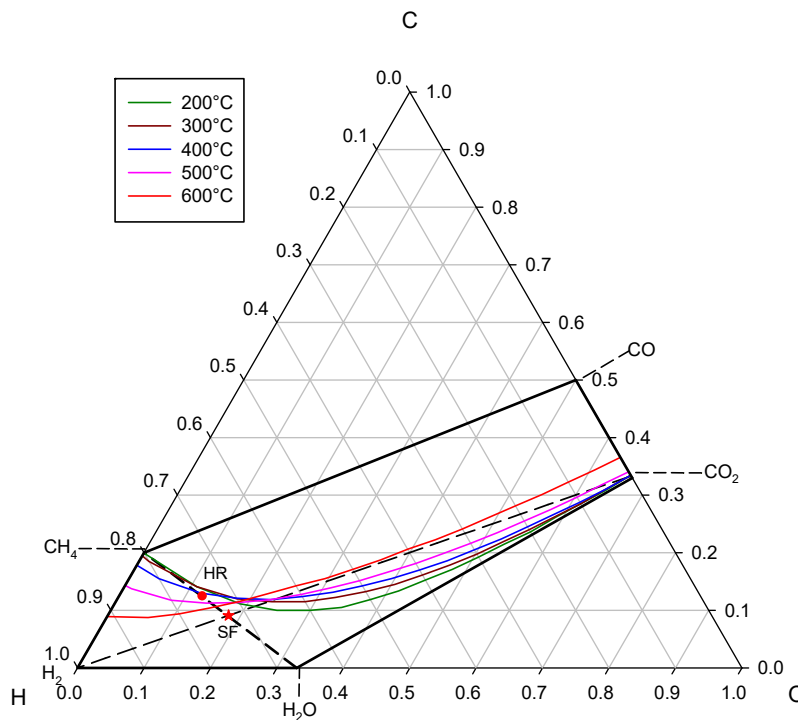


Figure 4.7 Carbon deposition boundaries at 1 atm

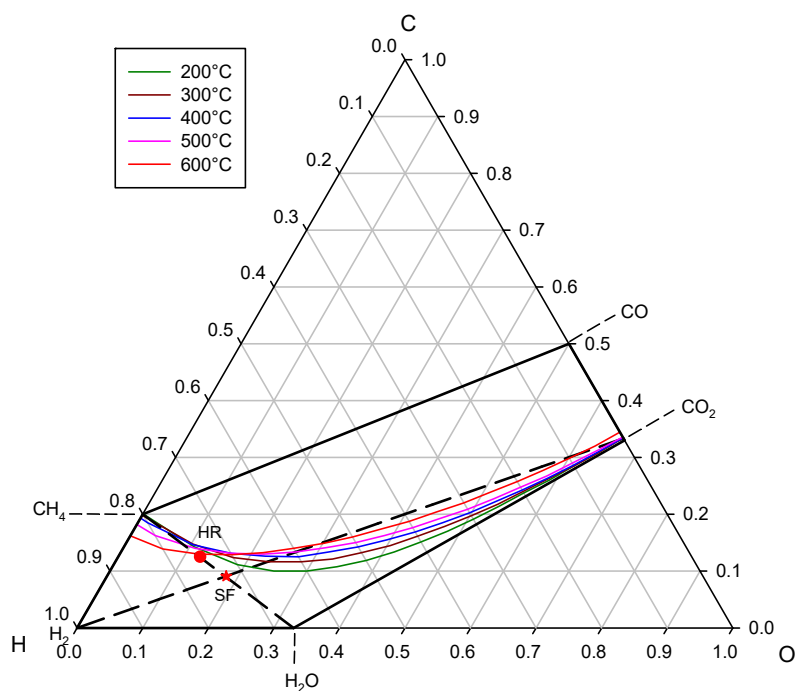


Figure 4.8 Carbon deposition boundaries at 10 atm

At 10 atm no carbon is formed in the range 200-600°C for $R_{H_2O} = 0.5$: the HR point in fact is always located below all the curves. However, carbon would form in other conditions, i.e. for $R_{H_2O} > 0.5$, which is the same as moving upwards along the line connecting CH_4 and H_2O . At 1 atm the HR point is above the 500 and 600°C curves. In this case, too, increasing R_{H_2O} would mean to enhance carbon generation. Therefore, it can be primarily pointed out as first result that under a stoichiometric feed ($H_2/CO_2 = 4$) only partial steam removal can be performed in order to avoid carbon deposition at low pressure.

Based on this consideration, the maximum value of R_{H_2O} which ensures no-carbon formation was calculated. In the ternary diagram, for each temperature, the value $R_{H_2O,max}$ is the point where the line connecting CH_4 and H_2O crosses the carbon deposition boundary. Figure 4.9 shows the $R_{H_2O,max}$ values as a function of temperature for the two pressures: under all operating conditions considered in this work $R_{H_2O,max} < 1$, i.e. it is not possible to capture all the formable steam without generating carbon. The calculated $R_{H_2O,max}$ can be found in the range 0.28-0.94, with larger values at lower temperature and higher pressure. It can be underlined that SEM conditions corresponding to $R_{H_2O,max}$ provide, clearly, the best methanation performance with stoichiometric feed. At 600 °C there is an increase of 10 percentage points in methane yield: this result is depicted in figure 4.10.

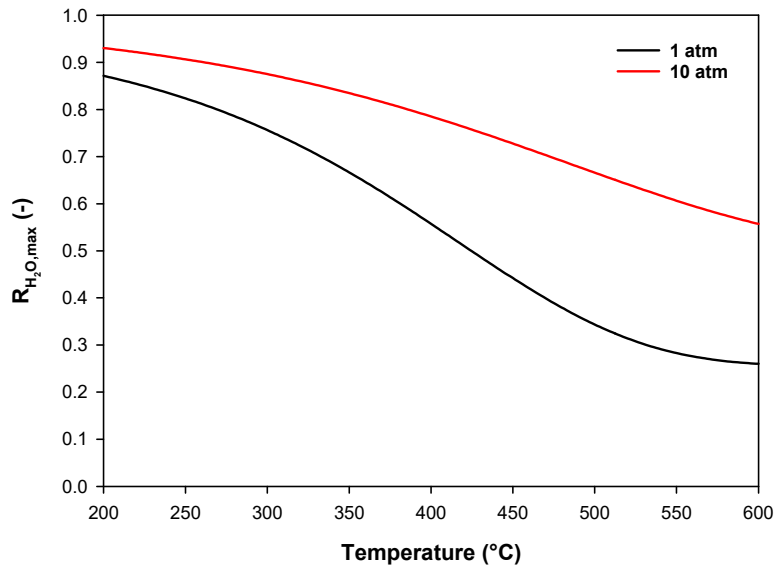


Figure 4.9 $R_{H_2O,max}$ as a function of temperature for two pressures (1 and 10 atm)

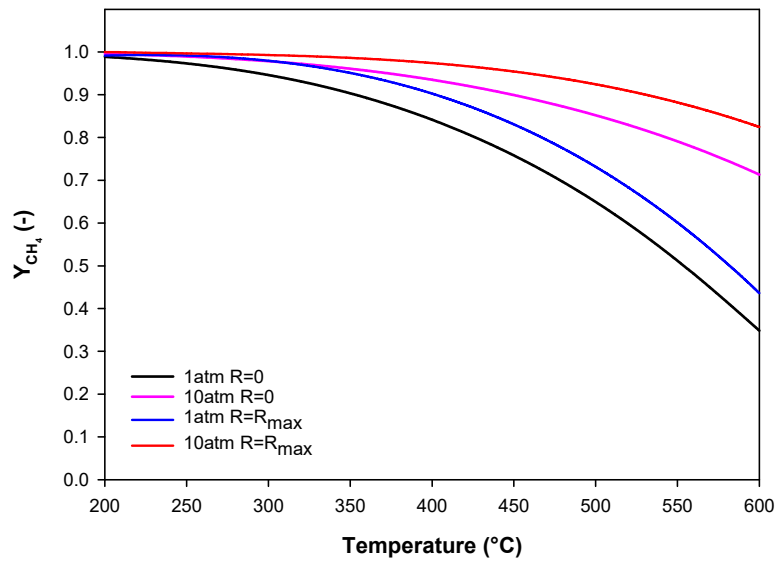


Figure 4.10 Methane yield as a function of temperature for the two pressures under traditional methanation ($R = 0$) and optimal SEM ($R = R_{max}$) conditions

Back to the other important target to investigate, the gas quality, it is interesting to compare this indicator under SEM conditions corresponding to $R_{H_2O,max}$, namely those providing the best performance, with that obtained under traditional methanation ($R_{H_2O} = 0$). Figure 4.11 reports the dry gas molar concentrations of CO_2 , CO , and H_2 under the above conditions (in the figure, also the main contaminants specifications are reported as dashed lines, for reference).

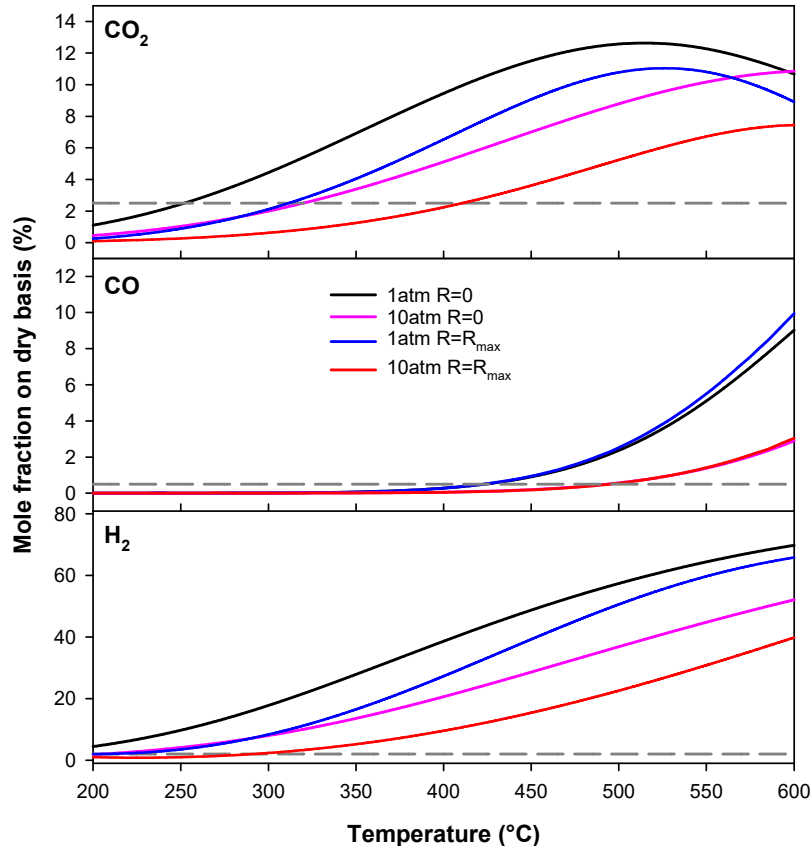


Figure 4.11 Dry gas molar concentrations of CO_2 , CO , and H_2 as a function of temperature. The grey dashed lines in the graphs refer to the limit values of 2.5% (CO_2), 0.5% (CO), and 2% (H_2)

Regarding the suitability of the equilibrium product gas composition for the injection in the natural gas grid the following results can be summarized:

- the outlet CO concentration is not affected appreciably by operating under SEM conditions: its limit 0.5% is fulfilled below 420 °C and 490 °C at 1 and 10 atm, respectively;
- optimized SEM conditions can significantly extend the operating range as regards the acceptable outlet CO_2 concentration, 2.5%: from 250 to 310°C and from 320 to 410°C at 1 and 10 atm, respectively;
- the acceptable outlet H_2 concentration appears to be the most critical limit to be respected: only at 10 atm under SEM the limit is fulfilled and only below 290 °C.

The feasibility of working under a non-stoichiometric feed was also investigated and illustrated with a ternary diagram, in figure 4.12, showing this possible advantage. By way of example, the carbon deposition boundary curve at 1 atm and 500°C is reported. In this diagram, a feed richer in H₂ (i.e. H₂/CO₂ > 4) is a point on the line H₂-CO₂ on the left of the SF point. In the figure, for example, a feeding point NSF can be found such that even with R_{H₂O} = 1 still no carbon is formed. This point in this case refers to a feed with H₂/CO₂ ~ 5. With 4 < H₂/CO₂ < 5, more H₂O can be captured with respect to the SF case but R_{H₂O,max} remains < 1. R_{H₂O,max} = 1 can always be obtained using a ratio > 5, however there is clearly no advantage in operating at such a large hydrogen excess, since the greater the feed ratio the higher the unreacted H₂ in the exit gas. In any case, when R_{H₂O,max} = 1, the equilibrium conditions can be depicted by a point on the left axis in the ternary diagram, located between CH₄ and H₂ (see fig. 4.12), implying a methane yield always = 1 and CO₂ and CO concentrations = 0, which are clearly very appealing operating conditions.

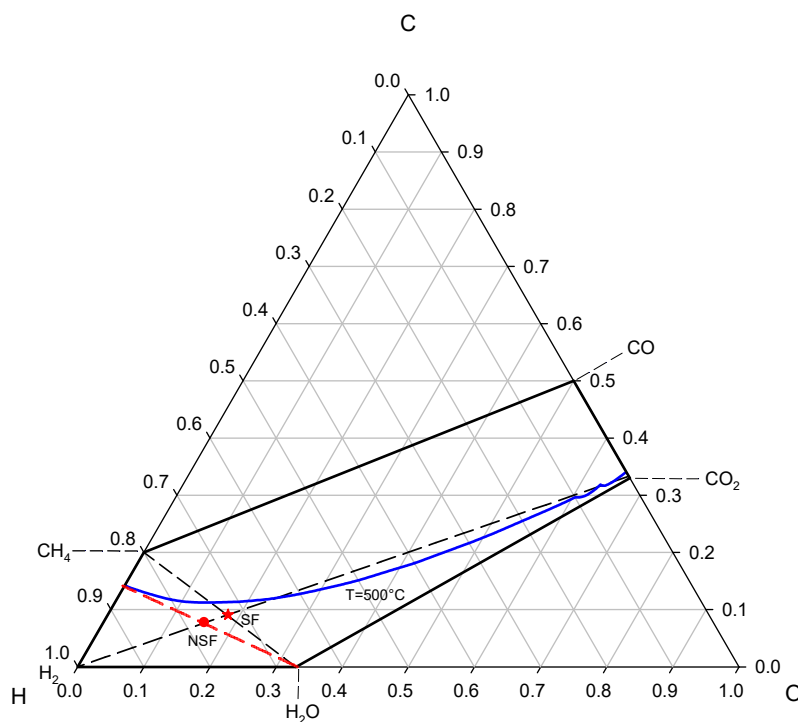


Figure 4.12 Carbon deposition boundary at 500°C and 1 atm

This evaluation was extended to all temperatures at the considered pressures: figure 4.13 reports the threshold H₂/CO₂ feed ratios where R_{H₂O,max} = 1 can be attained. This ratio increases exponentially with temperature and, as expected, values at 10 atm are much lower than those at 1 atm.

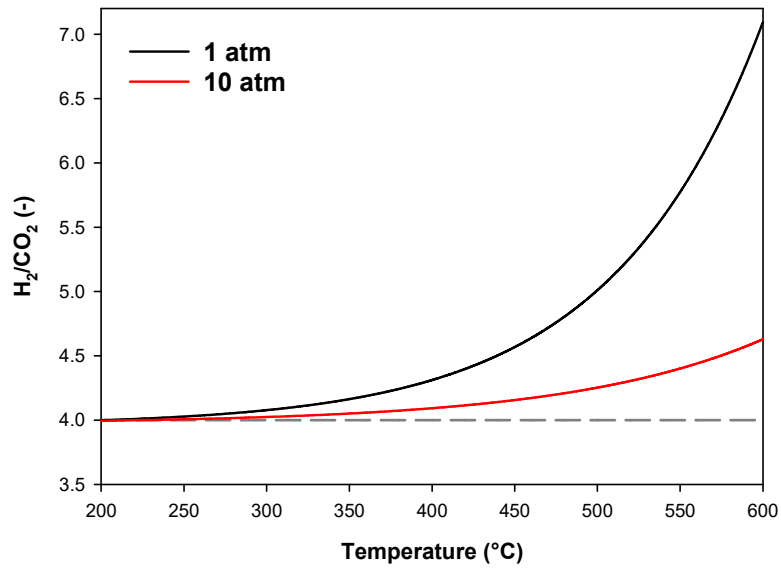


Figure 4.13 Non-stoichiometric H_2/CO_2 feed ratios where $R_{\text{H}_2\text{O},\text{max}} = 1$

The H_2 amount in the gas is still the critical quantity to be examined. In figure 4.14 the comparison between the H_2 dry gas molar concentration for NSF conditions and that for traditional methanation ($R_{\text{H}_2\text{O}} = 0$) and stoichiometric feed, is reported. It can be observed that under optimal non-stoichiometric feed conditions with $R_{\text{H}_2\text{O}} = 1$ the 2% H_2 limit can be respected only below 230 and 300°C at 1 and 10 atm, respectively.

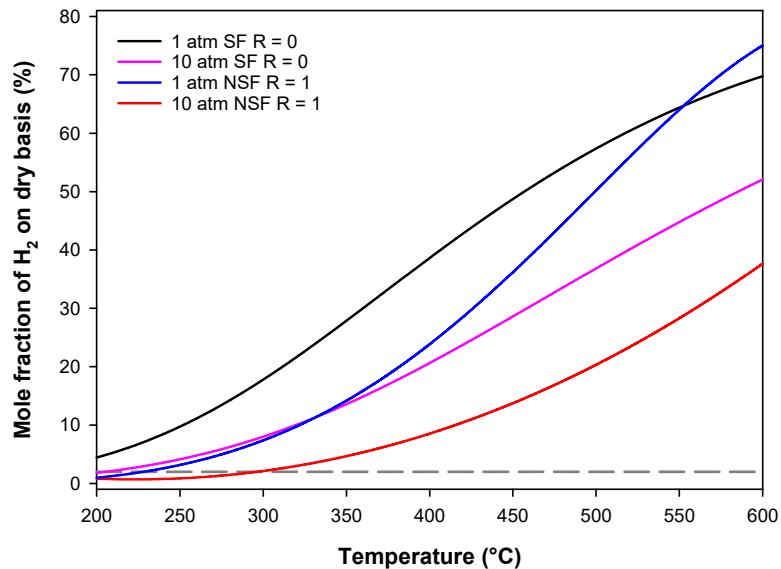


Figure 4.14 Dry gas H_2 molar concentration with stoichiometric feed ($R = 0$) and optimal non-stoichiometric SEM ($R = 1$) conditions

Based on the above considerations, optimal SEM conditions may either imply non-stoichiometric feed and $R_{H_2O} = 1$ or stoichiometric feed and thus $R_{H_2O} < 1$. At this point, it can be meaningful to make some evaluations on the possible operating conditions in different reactor types. Considering a fixed bed process during SEM, until steam breakthrough from the bed, all the produced H_2O is removed by the sorbent: this means that $R_{H_2O} = 1$ operation is the only one performable in such reactors where, hence, only non-stoichiometric feeds could guarantee no-carbon formation. On the other hand, both a membrane reactor and a dual fluidized bed may assure steady operation and H_2O capture fraction in the whole range $0 < R_{H_2O} < 1$, with more flexible operation guaranteeing avoidance of carbon deposition.

Specifically, R_{H_2O} can be regulated:

- in a membrane reactor, by tailoring the permeability or the pressure gradient across the membrane;
- in a dual fluidized bed reactor, by changing the sorbent circulation rate or the ratio of sorbent/catalyst loaded in the system.

5 CO₂ SEM: AspenPlus simulation

5.1 CO₂ SEM using CaO as sorbent: Aspen model

Before experimentally testing CO₂ SEM using CaO in the lab-scale fluidized bed reactors, the process in a dual interconnected fluidized beds system was simulated with AspenPlus software. The SEM process was analyzed with the main goal of obtaining final synthetic natural gas streams matching network specifications, studying the effect of the variation of the input CaO sorbent flow rate. Moreover, referring to pure CO₂ methanation, the previously shown thermodynamic analysis (Chapter 4) was carried out with a strong simplifying assumption: the removal of water vapor did not take into account any specific sorbent material present in the system and, possibly, participating to the chemical equilibrium calculations. However, one of the selected sorbents, CaO, gives hydration in the range of interest for our process resulting in a chemical adsorption. As verified in the experimental campaign on the sorption capacity of the materials (Chapter 7), when considering CaO hydration, unfortunately, the undesired carbonation reaction of the sorbent must be also considered. The SEM process was here modeled considering, more specifically, the kinetics involved in all the reactions and simulating the methanation as a real chemical looping system. To do that, AspenPlus[®]V10 software provides the FluidBed reactor block, which is specifically designed to simulate fluidized bed reactors, and it was applied here to build the process scheme. Aspen Plus FluidBed block describes the bed fluid mechanics as isothermal and one-dimensional. The model considers the fluidized bed as consisting of two zones: a bottom zone and a freeboard. The former is distinguished by high solids concentration and involves the modeling of bubbles growth and splitting (according to Werther [75]), while for the freeboard, with low solid concentration, the fluid mechanics is described according to Levenspiel [76]. Bed inventory can be specified fixing the pressure drop or the solids hold-up and, consequently, the height of the bottom zone and that of the freeboard can be determined. The simplified scheme is reported in Figure 5.1. The model allows to consider chemical reactions assuming gas as in plug flow and solids ideally mixed with each balance cell considered as a mixed reactor. Several correlations are provided to determine quantities like minimum fluidization velocity, transport disengagement height, distributor pressure drop as well as bubble-related quantities (e.g. bubble diameter, bubble rise velocity) and interstitial gas velocity profiles. The user can specify the voidage at minimum fluidization, Geldart group for the bed material and also directly the minimum fluidization velocity with no calculations. In this work, correlations were selected to determine minimum fluidization velocity (Wen & Yu) and the extent of elutriation (Tasirin & Geldart) [77].

For the solids, the model characterizes solid particles with size, density and terminal velocity and takes into account also the entrainment of particles by means of different options. The change in particle size distribution (PSD) due to reaction may be considered by using selected entrainment correlations, by means of which the solids mass flow and PSD at the outlet can be calculated. The particle size distributions are modeled by functions of parameters which identify a characteristic particle size and a deviation to describe the distribution wideness. In this work, the GGS (Gates-Gaudin-Schuhmann) distribution function was used, for which the general cumulative formula is:

$$Q(d) = \begin{cases} (d/d_{max})^n & d < d_{max} \\ 1 & d > d_{max} \end{cases}$$

with $d_{max}=0.6$ mm and $n=1.5$ for all the solids considered. In our simulations the particle size distribution of the outlet sub-streams involved in the reactions was set equal to the PSD of the corresponding inlets.

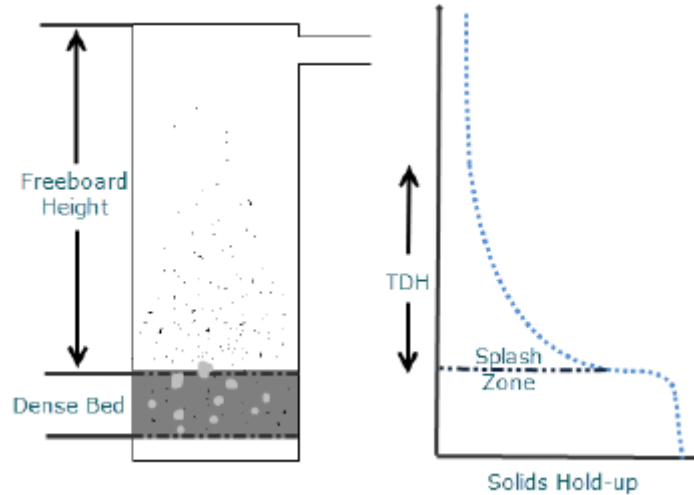


Figure 5.1 Two zones-model scheme

The flowsheet of the simulated looping SEM process is reported below (Figure 5.2).

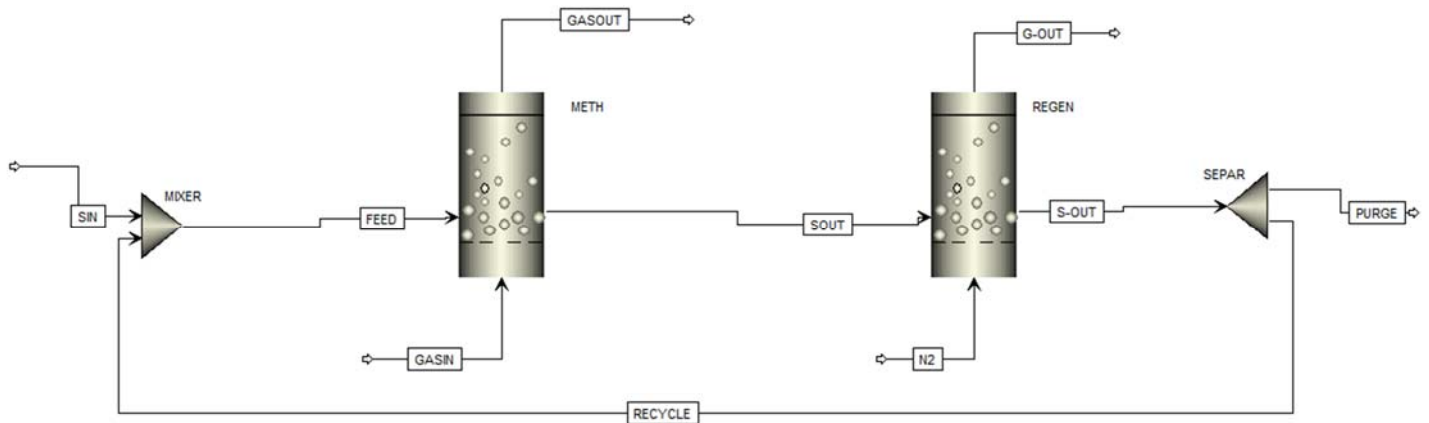


Figure 5.2 SEM process flowsheet

In the methanator (METH block) the catalytic methanation takes place, using a Ni/Al₂O₃ catalyst; simultaneously, the steam produced in situ is removed using the CaO sorbent, which can also give carbonation in the presence of CO₂. Consequently, the kinetics of methanation, water-gas shift, hydration, and carbonation were implemented in this block. This reactor was simulated in the temperature range of interest for SEM: 250-350 °C. In the regenerator (REGEN block, 450 °C) the sorbent is regenerated using a nitrogen stream and then recycled to the methanator. Both reactors are at atmospheric pressure. A make-up stream of sorbent, which is subject to deactivation, and, consequently, a purge stream, are required in the scheme. The analysis was carried out introducing two dimensionless parameters (both defined on molar basis). To characterize the gas feed, the following parameter was used:

$$\alpha = \frac{H_2 - CO_2}{CO_2} \quad (5.1)$$

The parameter describes the gas feed in terms of reactants: a stoichiometric feed implies a value equal to 3. To characterize the solid feed stream, a second parameter θ was defined as the ratio between the CaO fed to methanator and the stoichiometric value for this sorbent:

$$\theta = \frac{CaO}{CaO_{st}} \quad (5.2)$$

When referring to the stoichiometric solid, the hydration reaction is considered and, in particular, water removed by CaO is a methanation product: CaO_{st} is, therefore, the stoichiometric CaO with respect to the maximum amount of water that can be formed by this reaction when complete. θ equal to 1 corresponds to a stoichiometric solid supply. If $\alpha \geq 3$, i.e. when the input gas supply is stoichiometric or over-stoichiometric (i.e. with excess H_2), water that can be at most produced from the CO_2 methanation reaction is merely equal to $2CO_2$; if $\alpha < 3$, water can amount at most to $H_2/2$. As for the kinetics aspects, a set of main reactions involved was selected. Table 5.1 reports the reactions implemented in the model. Among the possible reactions that can occur during methanation process, three main reactions were considered: methanation of CO, reverse reaction of WGS, and methanation of CO_2 . The kinetic expressions of these reactions were taken from the work by Xu and Froment [22]. Kinetics involving CaO, i.e. hydration [78] and carbonation [79], were also implemented in the model.

<u>REACTIONS</u>	$\Delta H_{298 K} \text{ (kJ mol}^{-1}\text{)}$
$CO + 3H_2 \leftrightarrow CH_4 + H_2O$	-206.2
$CO_2 + 4H_2 \leftrightarrow CH_4 + 2H_2O$	-165.0
$CO_2 + H_2 \leftrightarrow CO + H_2O$	41.2
$CaO + H_2O \leftrightarrow Ca(OH)_2$	-65
$CaO + CO_2 \leftrightarrow CaCO_3$	-178

Table 5.1 Reactions implemented in the simulation

The chosen kinetics followed the two main used models: Power Law and Langmuir-Hinshelwood-Hougen-Watson (LHHW) kinetic models, both implementable in AspenPlus.

The general expression of the Power Law is:

$$r = \text{kinetic factor} \prod_{i=1}^N C_i^{\alpha_i} \quad (5.3)$$

$$\text{kinetic factor} = k \left(\frac{T}{T_0} \right)^n \exp^{(-E/R)[1/T-1/T_0]} \quad (5.4)$$

Instead, for rate-controlled reactions, the LHHW rate expression can be written as:

$$\gamma = \frac{\text{kinetic factor}(\text{driving force expression})}{(\text{adsorption expression})} \quad (5.5)$$

$$\text{driving force expression} = K_1 \left(\prod C_i^{v_i} \right) - K_2 \left(\prod C_j^{v_j} \right) \quad (5.6)$$

$$\text{adsorption expression} = \left\{ \sum K_i \left(\prod C_j^{v_j} \right) \right\}^m \quad (5.7)$$

with:

r = rate of reaction

k = pre-exponential factor

T = temperature in Kelvin

T₀ = reference temperature in Kelvin

n = temperature exponent

E_a = activation energy

R = universal gas law constant

C = component concentration

m = adsorption expression exponent

K₁, K₂, K_i = equilibrium constants

v = concentration exponent

i, j = component index

For methanation kinetics, the expressions and parameters have already been reported (see paragraph 2.1.2), except for the expressions of the equilibrium constants (K_1 , K_2 , K_3) of the three reactions considered, written below:

$$K_1 = 10^{10} \exp\left(30,42 - \frac{27106}{T}\right) \quad (5.8)$$

$$K_2 = \exp\left(-3,798 + \frac{4160}{T}\right) \quad (5.9)$$

$$K_3 = 10^{10} \exp\left(34,218 - \frac{31266}{T}\right) \quad (5.10)$$

Where 1,2,3 refer to CO methanation, RWGS reaction and CO₂ methanation, respectively. The model developed by the authors was a LHHW expression: the following figures (fig. 5.3, 5.4 and 5.5) show the terms of the driving force expressions in the software required form.

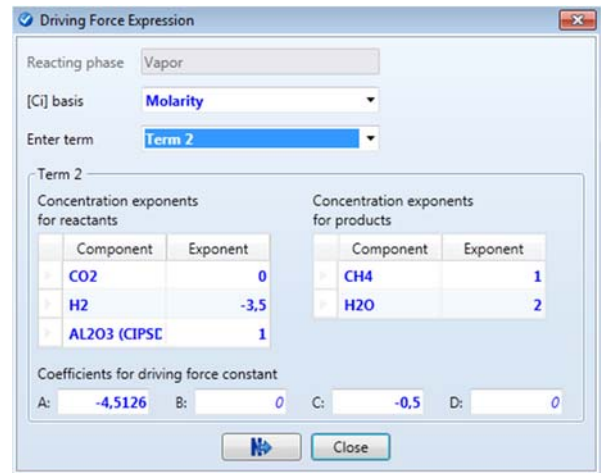
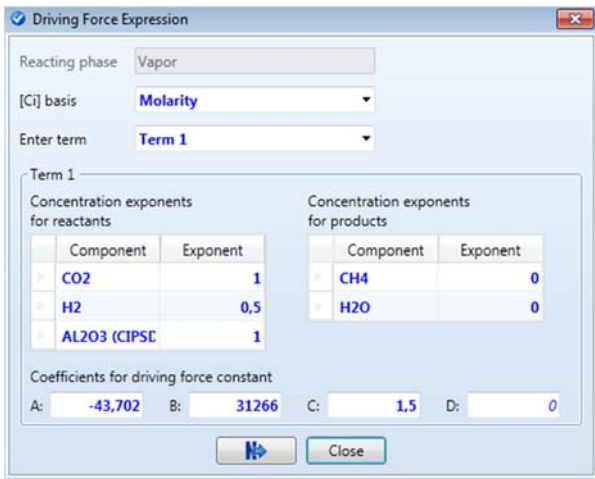


Figure 5.3 Driving force CO methanation

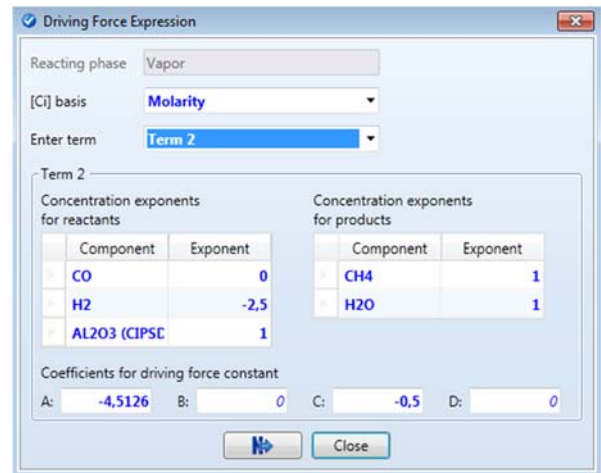
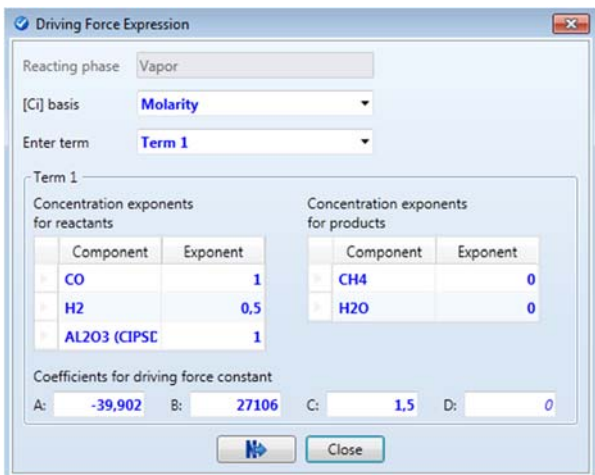


Figure 5.4 Driving force CO₂ methanation

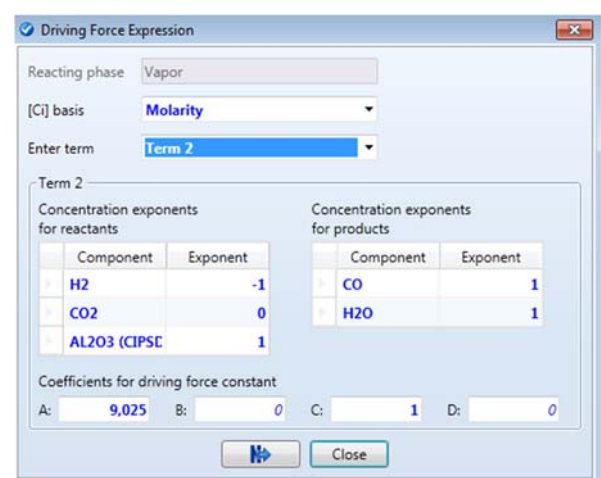
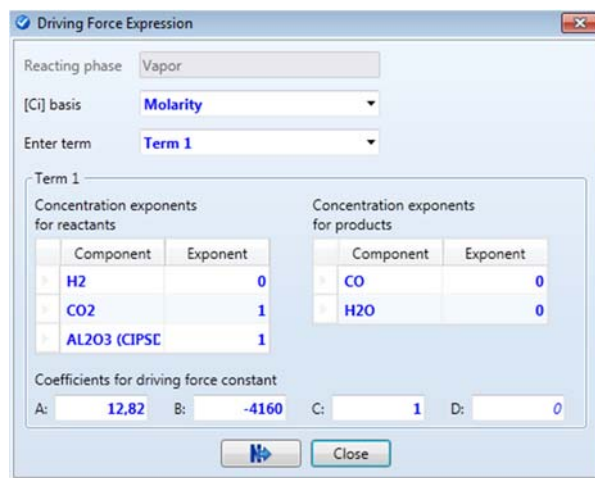


Figure 5.5 Driving force RWGS reaction

The adsorption expression is the same for the three reactions (figure 5.6):

Reacting phase: Vapor
[C] basis: Molarity
Adsorption expression exponent: 2

Concentration exponents

Component	Term no. 1	Term no. 2	Term no. 3	Term no. 4	Term no. 5	Term no. 6
CH4	0	1	0	0	0	0
H2	0	0	1	-1	0	0
H2O	0	0	0	1	0	0
CO	0	0	0	0	0	1

Adsorption constants

Term no.	1	2	3	4	5
Coefficient A	0	-16,711	-28,307	12,084	-18,8
Coefficient B	0	4606,5	9975,93	-10671,5	8502
Coefficient C	0	1	1	0	1
Coefficient D	0	0	0	0	0

Figure 5.6 Adsorption term for methanation process kinetics

It should be noted that an equilibrium constants K in Aspen must be given through parameters according to the formula:

$$\ln(K) = A + \frac{B}{T} + CT + DT^2 \quad (5.11)$$

Considering the reactions involving CaO and in particular hydration, the final equation applied in the simulation was [89]:

$$\frac{dX}{dt} = 13945 \times \exp\left(\frac{-89,486 \times 10^3}{RT}\right) \left(\frac{P}{P_{eq}} - 1\right)^{0,83} \cdot 3(1 - X) [-\ln(1 - X)]^{0,666} \left[\frac{1}{s}\right] \quad (5.12)$$

In this expression, P represents the partial pressure of water and X the calcium oxide conversion. The equilibrium partial pressure of water (P_{eq}) was expressed as follows:

$$\ln\left(\frac{P_{eq}}{10^5}\right) = -\frac{12845}{T_{eq}} + 16,508 [Pa] \quad (5.13)$$

A fixed average conversion degree ($X=0.5$) was assumed to implement the kinetics in terms of molar fractions.

The expression for the dehydration reaction is also reported [78]:

$$\frac{dX}{dt} = 1,9425 \times 10^{12} \exp\left(\frac{-187,88 \times 10^3}{RT}\right) \left(1 - \frac{P}{P_{eq}}\right)^3 (1 - X) \left[\frac{1}{s}\right] \quad (5.14)$$

To implement this equation, the reaction was divided into 4 blocks such that the summation gives the equation above:

$$1. \quad \left(\frac{dX}{dt}\right)_1 = kP_{eq}^3; \quad r_1 = \frac{k}{y_{eq}^3} y_{eq}^3 Y_{Ca(OH)_2} = kY_{Ca(OH)_2} \quad (5.15)$$

$$2. \quad \left(\frac{dX}{dt}\right)_2 = -kP^3; \quad r_2 = -\frac{k}{y_{eq}^3} y^3 Y_{Ca(OH)_2} \quad (5.16)$$

$$3. \quad \left(\frac{dX}{dt}\right)_3 = -3kP_{eq}^2 P; \quad r_3 = -\frac{3k}{y_{eq}^3} y_{eq}^2 Y_{Ca(OH)_2} Y \quad (5.17)$$

$$4. \quad \left(\frac{dX}{dt}\right)_4 = 3kP_{eq} P^2; \quad r_4 = \frac{3k}{y_{eq}^3} y_{eq} Y_{Ca(OH)_2} Y^2 \quad (5.18)$$

In AspenPlus, four POWERLAW kinetics were entered (direct 1 and 4, inverse 2 and 3). The data are reported below:

$$1. \quad k = 1.9425(10)^{12}$$

$$E = 187.88 \text{ kJ/kmol};$$

$$2. \quad k = 394000$$

$$E = 81.087 \text{ kJ/kmol};$$

$$3. \quad k = 5.99(10)^{-10}$$

$$E = -132.449 \text{ kJ/kmol}$$

$$4. \quad k = 0,0266$$

$$E = -25.706 \text{ kJ/kmol}.$$

Lastly, for the carbonation reaction, the following expression was considered [79]:

$$\frac{dX}{dt} = \frac{k_s S_0}{1 - \varepsilon_0} (C - C_{eq})(1 - X)^{2/3} \left[\frac{1}{s}\right] \quad (5.19)$$

The kinetics of reactions between gases and solids are typically schematized using models in which a uniform solid layer is produced and covers the entire solid surface with a distinct interface between the solid reactant and the product (the shrinking-core or shrinking-pore model). However, the

considered study establishes a general theory to model the kinetics of gas-solid reactions for solid reactants of various shapes, assuming that the solid product grows as clusters instead of a uniform solid layer. The expressions for the kinetic constant (k_s) and the equilibrium concentration of CO_2 (C_{eq}) are given below:

$$k_s = k_{s0} \exp\left(-\frac{E_k}{RT}\right) \left[\frac{\text{m}^4}{\text{mol} \cdot \text{s}} \right] \quad (5.20)$$

$$C_{\text{eq}} = \frac{1,826 \times 10^6}{8,314 \cdot T} \exp\left(\frac{-19680}{T}\right) \left[\frac{\text{mol}}{\text{m}^3} \right] \quad (5.21)$$

Table 5.2 shows the values of all the physical and kinetic parameters used, such as the initial specific surface area of calcium oxide (S_0), the initial porosity (ϵ_0), the pre-exponential factor (k_{s0}), and the activation energy (E_k) of the carbonation reaction.

S_0 [m^2/m^3]	ϵ_0 [-]	k_{s0} [$\text{m}^4/(\text{mol}\cdot\text{s})$]	E_k [KJ/mol]
42×10^6	0.47	2.72×10^{-7}	44.76

Table 5.2 Physical and kinetic parameters

The driving force expression implemented is shown below (figure 5.7).

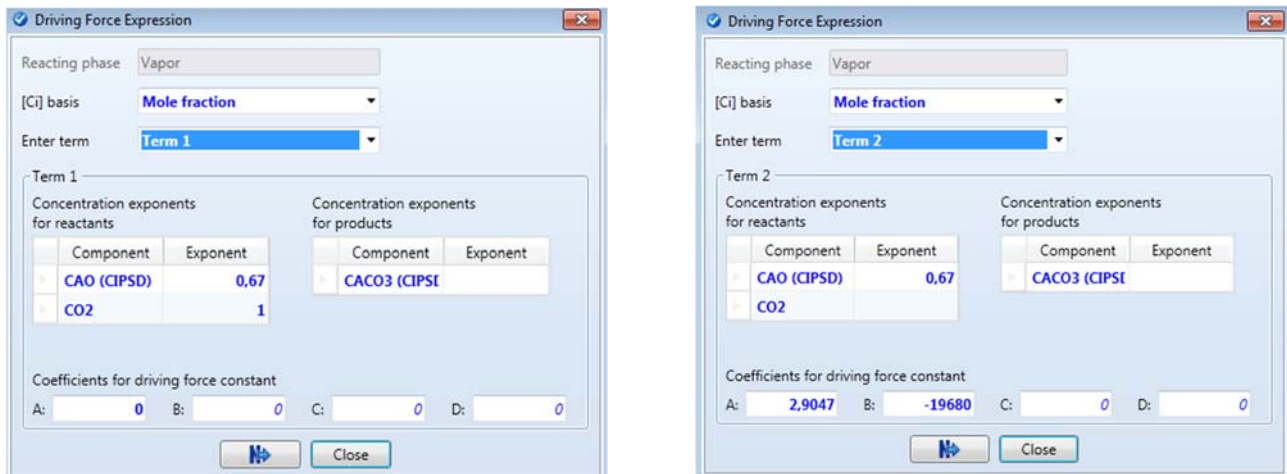


Figure 5.7 Driving force for Carbonation

For the characteristics of the two reactors constituting the looping scheme, the parameters used for the simulations, required by Aspen in the section of the input block, are summarized in Table 5.3.

REACTOR INPUT	Height (m)	Diameter (m)	Bed mass (Kg)	Solid discharge location (m)	Voilage at minimum fluidization (-)	Average solids particle size (mm)	Geldart classification
METH	5	0.26	50	0.5	0.5	0.5	B
REGEN	8	0.33	100	0.64	0.5	0.5	B

Table 5.3 Aspen specifications for the reactors

The heights of reactors were set to obtain a freeboard always higher than the calculated transport disengaging height, which was determined according to the George and Grace model.

Regarding the material flows entering the system, the CO₂ flow in the “GASIN” stream was fixed at 5.6 Nm³/h and the H₂ was made to vary (between 16.8 and 22.4 Nm³/h depending on the gas feed ratio α). The recirculating solid stream entering the Meth block, “FEED”, was kept fixed at a mass flow value of 100 kg/h. As far as the solid make-up “SIN” is concerned, to work with a given θ in the feed, a sensitivity analysis was performed on the molar flow rate of CaO in the make-up stream obtaining a relationship between the feed and make-up CaO flow rates for each gas supply condition at the methanator inlet. As for the REGEN block, the desorption operation was simulated in a N₂ flow of 40 Nm³/h. The gas superficial velocity was 0.3 m/s for the REGEN block and varied between 0.3 and 0.4 m/s for the METH block. The above data have been selected to have a maximum potentiality of the methanation plant of about 50 kW_{th} (based on the methane LHV). The methanation reactor dimensions and the operating conditions are comparable with those of a demonstration scale fluidized bed reactor on the GAYA plant located in France where CO₂ methanation tests were carried out over a wide range of conditions to investigate efficiency and flexibility needed to manage the fluctuations associated with a Power-to-Methane (PtM) process [80]. This reactor consists of a fluidized bed reactor with a total length of 5.4 m and a diameter of the fluidizing section of 0.30 m, including an internal heat exchanger. The different fluidization velocities, involved by different α and temperatures of the gas flow rates, for a fixed reactor diameter, did not impact the results of our simulations in the range considered (0.3-0.4 m/s). This is consistent with the results obtained by the experimental campaign on the GAYA plant in which fluidization velocities were varied in a quite wide range (u_f/u_{mf} from 2.9 to 7.2), demonstrating that performances are not affected by such variations and that thermodynamic conversion is nearly achieved regardless of the fluidization state [80].

5.2 CO₂ SEM using CaO as sorbent: results

First, an analysis of traditional CO₂ methanation was carried out in Aspen under stoichiometric conditions ($\alpha = 3$): in order to use the designed looping for conventional methanation, the hydration-dehydration and carbonation reactions were deactivated in the Aspen model. The compositions along the methanator height were evaluated and the following graph is shown, with the height along the bed on the X-axis and the mole fractions of the gases in the methanator on the Y-axis, for one of the temperatures considered, 300 °C (figure 5.8).

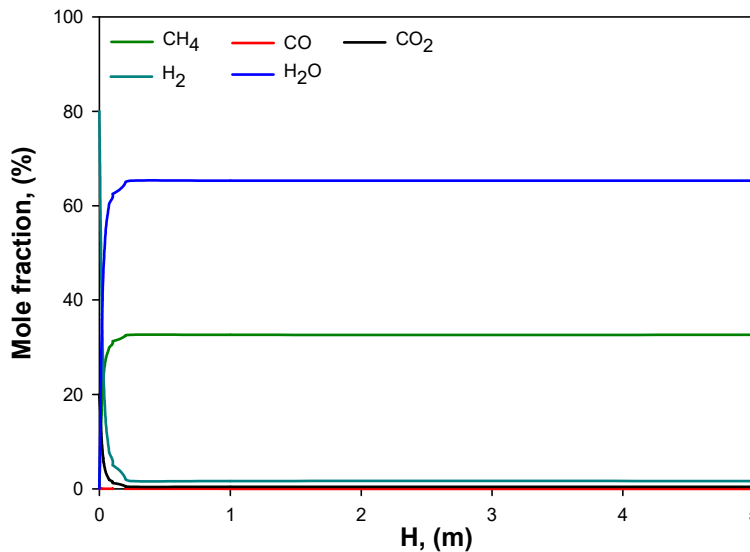


Figure 5.8 Gas mole fractions along the bed for traditional methanation at $\alpha=3$

With a stoichiometric gas feed ratio, at 300°C a good composition of the outlet gases is obtained, with most of the conversion occurring in the first part of the bed, which confirms a typical trend for this type of reactors. Although the methane yield is high, the gas leaving the methanator is not allowed to be fed into the grid. Specifications for the injection in the natural gas grid are, as described in the thermodynamic analysis, a crucial point with the critical amount being the H₂ content. The H₂ concentration on a dry basis reached at $\alpha = 3$ is 4.78 %, thus above the permitted limit of 2% on a dry basis. As with traditional methanation, the data for the SEM process were evaluated for $\alpha = 3$ and, in this case, varying θ and obtaining the trends by means of Aspen's sensitivity function. The SEM process was initially proposed for obtaining a high-grade methane to feed directly into the grid. This result, however, is not trivial given the complexity of the kinetic pathway to consider. The graph below (figures 5.9) shows the outlet mole fractions of various species as a function of the feed parameter θ for a METH block temperature fixed at 300 °C.

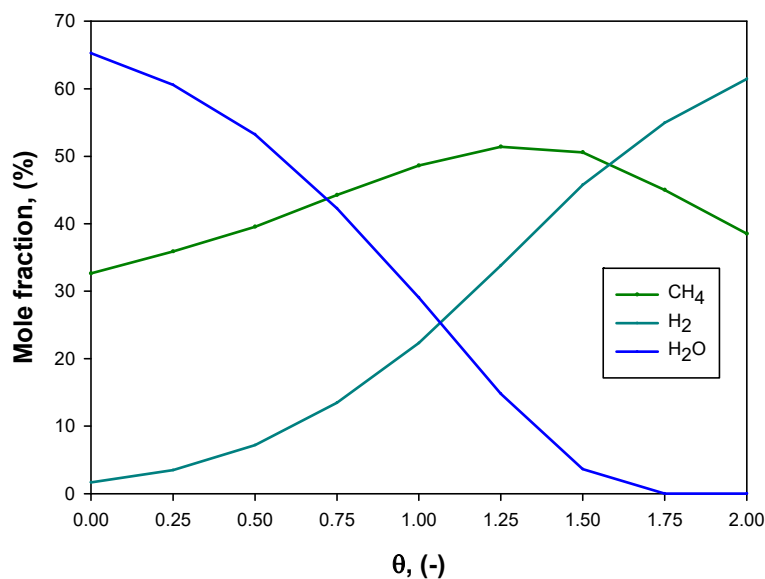


Figure 5.9 Outlet gas mole fractions at $\alpha=3$ and $T=300$ °C by varying θ

If considering, for example, the CH₄ mole fraction, as the amount of calcium oxide entering the system increases, i.e. θ increases, the methane mole fraction increases due to a higher water removal up to a θ value equal to 1.25 ($\theta > 1$ corresponds to a CaO feed higher than the stoichiometric value). To clarify this last result, water vapor mole fraction is also reported and it is clear that increasing θ , the mole fraction of H₂O decreases since the calcium oxide is absorbing more water. As far as H₂ is concerned, outlet hydrogen increases with a more accentuated trend with respect to the other species as θ increases: the H₂ trend shows that a significant fraction of CO₂, which would be destined for methanation and thus for hydrogen consumption and methane production, is actually reacting with calcium oxide. In general, increasing θ enhances both the amount of H₂O and CO₂ adsorbed. However, the sorbent reacts first with CO₂, immediately available in the reaction environment, and then with water, formed by the methanation reactions, which implies that the positive effect of water vapor capture on methanation reaction may fail to overcome the negative influence of CO₂ capture. Since CO₂ is adsorbed from the beginning of the process, both the reverse WGS reaction and the CO₂ methanation reaction are shifted toward the reactants and, due to the carbonation reaction, the gas supply, initially stoichiometric, eventually becomes over-stoichiometric as the SEM process takes place. To test this negative effect further, a fictitious process was carried out without carbonation, by deactivating the carbonation reaction in Aspen. Considering and reporting the methane yield as performance indicator, the effect of carbonation is evident in figure 5.10. Neglecting carbonation, an increase of the yield is obtained with the increase of θ : the CO₂, in this case, is completely destined to methanation, and increasing CaO more and more water is absorbed shifting the methanation equilibrium towards the products formation. In the same graph, the methane yield in the more realistic case in which carbonation occurs, is also reported: the trend shows a strong decrease with θ increasing: a decrease of about 8 percentage points with respect to traditional methanation if θ is equal to the stoichiometric value of 1 and even up to about 27 percentage points if considering a value of θ equal to 2.

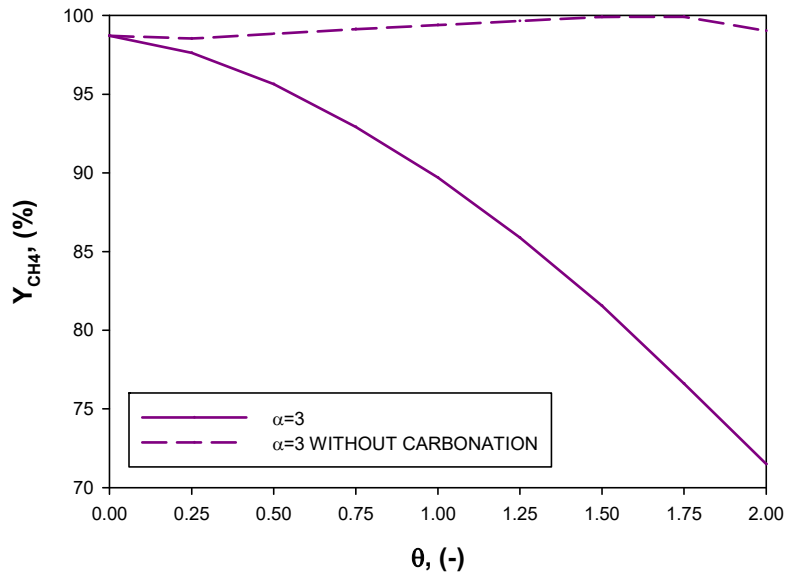


Figure 5.10 Methane yield for SEM process at 300 °C

Considering the important point of the methane purity in the stream leaving the methanator, the composition of the outlet gas (on dry basis) in terms of H_2 varies according to the trend shown in figure 5.11, for different values of the parameter θ . The figure shows that the percentage of H_2 at the outlet is always above the allowed limit (reported as a dash gray line in the graph), whatever condition is considered, and increases dramatically with θ , as already explained. Once again, the graph reports also the H_2 mole fraction when carbonation is deactivated: for values of $\theta \geq 1.25$, the outlet stream could be fed directly into the grid, as the percentage of hydrogen on a dry basis would be less than 2%.

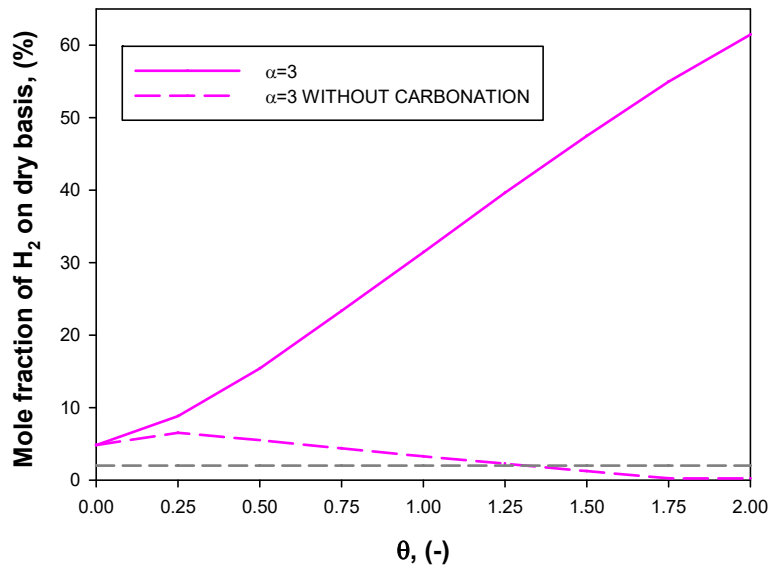


Figure 5.11 H₂ output from methanator for SEM process

Besides methanation at 300 °C, SEM conditions were evaluated for other temperatures in the range 250-350 °C and for a stoichiometric gas feed ratio, and compared to the conventional methanation case. The table below (table 5.4) reports the results in terms of outlet compositions on dry basis of the main components at 250, 275, 300, 325 and 350 °C.

$\alpha = 3$	T = 250 °C			T = 275 °C			T = 300 °C			T = 325 °C			T = 350 °C		
θ	H ₂ (%)	CO (%)	CO ₂ (%)	H ₂ (%)	CO (%)	CO ₂ (%)	H ₂ (%)	CO (%)	CO ₂ (%)	H ₂ (%)	CO (%)	CO ₂ (%)	H ₂ (%)	CO (%)	CO ₂ (%)
0	1.68	-	0.39	2.96	-	0.73	4.84	-	1.19	7.4	0.04	1.85	11.28	0.09	2.75
0.25	4.02	-	0.01	6.2	-	0.02	8.84	-	0.07	12.02	0.02	0.19	15.93	0.04	0.5
0.5	7.23	-	-	11.06	-	-	15.4	-	-	19.97	-	0.01	24.28	0.01	0.05
0.75	11.27	-	-	16.83	-	-	23.34	-	-	29.49	-	-	35.17	-	-
1	15.9	-	-	23.5	-	-	31.45	-	-	39.21	-	-	45.9	-	-
1.25	20.8	-	-	30.07	-	-	39.66	-	-	48.03	-	-	55.34	-	-
1.5	26.4	-	-	37.13	-	-	47.49	-	-	56.33	-	-	63.5	-	-
1.75	32.4	-	-	44.31	-	-	54.98	-	-	63.75	-	-	70.66	-	-
2	38	-	-	50.68	-	-	61.46	-	-	69.74	-	-	76.11	-	-

Table 5.4 H₂, CO₂ and CO molar concentrations on dry basis as function of θ and T for the simulations at $\alpha = 3$

In the table, the red and green areas refer to percentages, respectively, above the limit and allowed for injection in the natural gas grid. It is clear that for the entire range considered the critical species is represented by H₂ at the outlet, which presents the same trend, already highlighted at 300 °C, for all the temperatures: it drastically increases with θ , i.e. with the amount of injected CaO. Only one condition fulfills the requirements: if considering traditional methanation at 250 °C, the favored thermodynamic equilibrium at the lowest temperature enables to achieve a suitable H₂ concentration. However, 250 °C is merely a theoretical limit as operating temperature: the studies on active catalysts at low temperatures and most of the literature on commercial and demonstration scale methanation processes, identify higher temperatures as applicable for these reactions. For instance, the Ni-based catalyst developed by ENGIE for the already mentioned fluidized bed at the GAYA plant, reached the thermodynamic equilibrium showing optimized catalytic activity starting from 280 °C [80].

At this point, since the unconverted amount of hydrogen increases with θ , it was evaluated the possibility of working under SEM conditions with a sub-stoichiometric ($\alpha < 3$) gas supply to offset the excess hydrogen at the outlet and obtain streams that could be directly fed into the grid without a H₂ separation process. An analysis of CO₂ methanation for $\alpha < 3$, aimed at finding optimal operating conditions in terms of θ , was carried out. In figures 5.12 and 5.13 the outlet gas mole fractions of H₂ and CO₂ on dry basis obtained when varying θ , are reported for a temperature of 300 °C. For $\alpha = 2$ and $\theta \geq 1.25$ an optimal working condition is obtained, as the methane stream produced meets all network specifications. From this perspective, the analysis demonstrated that by working under sub-stoichiometric SEM conditions with respect to H₂ ($\alpha < 3$), using calcium oxide as sorbent, the excess H₂ obtained under stoichiometric feed conditions ($\alpha = 3$), can be compensated.

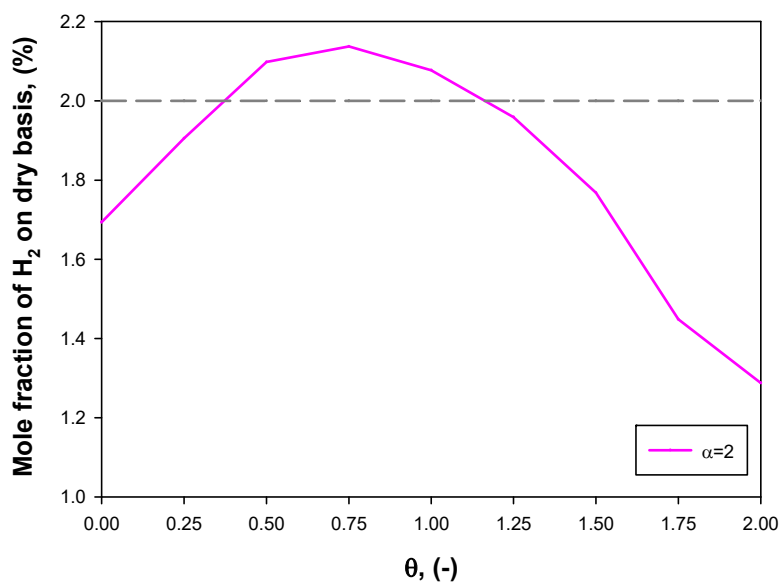


Figure 5.12 H₂ output from methanator for SEM process at 300 °C

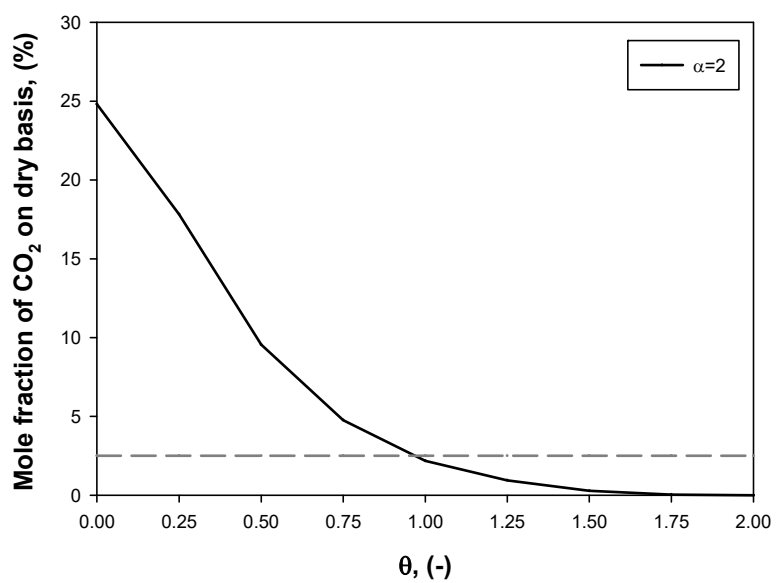


Figure 5.13 CO₂ output from methanator for SEM process at 300 °C

Also, for the case $\alpha=2$, a sensitivity on the temperature was carried out. Table 5.5 summarizes the results.

$\alpha = 2$	T = 250 °C			T = 275 °C			T = 300 °C			T = 325 °C			T = 350 °C		
θ	H ₂ (%)	CO (%)	CO ₂ (%)												
0	0.46	-	24.99	0.91	-	24.98	1.69	0.07	24.82	2.99	0.13	24.9	5.03	0.24	24.81
0.25	0.46	0.01	19.46	1.16	-	11.76	1.9	-	17.82	4.31	0.02	8.19	7.48	0.07	7.05
0.5	0.43	0.01	13.86	0.99	0.03	11.53	2.1	0.05	9.54	4.14	0.09	7.99	8.27	0.11	5.1
0.75	0.38	0.01	9.92	0.94	0.02	7.17	2.14	0.04	4.76	4.58	0.06	3.02	9.04	0.09	2
1	0.34	0.01	7.06	0.86	0.02	4.32	2.08	0.03	2.17	4.78	0.05	1.04	9.76	0.06	0.59
1.25	0.29	0.01	4.94	0.77	0.02	2.36	1.96	-	0.94	4.64	-	0.37	10.17	-	0.17
1.5	0.23	0.02	2.75	0.64	0.02	0.99	1.77	-	0.28	4.51	-	0.1	14.35	-	0.01
1.75	0.15	0.03	1.01	0.47	0.03	0.22	1.45	-	0.04	7.79	-	-	25.45	-	-
2	-	0.1	-	0.07	-	-	1.29	-	-	18.8	-	-	36.09	-	-

Table 5.5 H₂, CO₂ and CO molar concentrations on dry basis as function of θ and T for the simulation at $\alpha = 2$

For temperatures higher than 300 °C, even offsetting the hydrogen excess, no streams fulfilling the grid limitations can be found due to the high H₂ content. For a temperature of 275 °C, as already seen for 300 °C, a value of θ at which both CO₂ and H₂ output are below the network specifications can be found corresponding to a $\theta \geq 1.25$. In this case, i.e. with a CO₂ excess in the gas supply, the critical composition to comply with the limits is the CO₂ one. In fact, at 275 °C, the outlet H₂ is always below 2%.

It should be noted that for conditions in which H₂ is below its limit while CO₂ is above the limit, e.g. at 275 °C and for θ equal to 0 and 0.25 at 300 °C, the possibility of carrying out a process involving a final post-methanation CO₂ removal stage may be considered, since CO₂, unlike H₂, can be easily removed from the gas stream. In the case of a SEM process, where calcium oxide is already present, this sorbent could be also applied to remove CO₂ from the outlet stream. A technical-economic evaluation may determine the most suitable solution among the different conditions.

During the SEM process analysis, when optimal conditions in terms of removed water are detected, thermodynamic considerations, as discussed in the previous chapter, are also required. In particular, possible carbon formation was investigated for the values of $\theta \geq 1.25$ at 275 and 300 °C, and the amount of steam captured under these condition was compared with the maximum amount of water that is possible to remove without carbon formation (as calculated in the previous chapter). The use of ternary diagrams, to better visualize the thermodynamic behavior of the SEM system, can be helpful. In the diagram below (figure 5.14) the carbon formation isotherms (at 275 and 300 °C) are reported together with the most significant gas compositions: the feed for $\alpha=2$ ($\alpha 2$) and the compositions for two values of θ identifying the interval in which grid injection starts to be possible ($\theta 1$ and $\theta 1.25$) at the two temperatures.

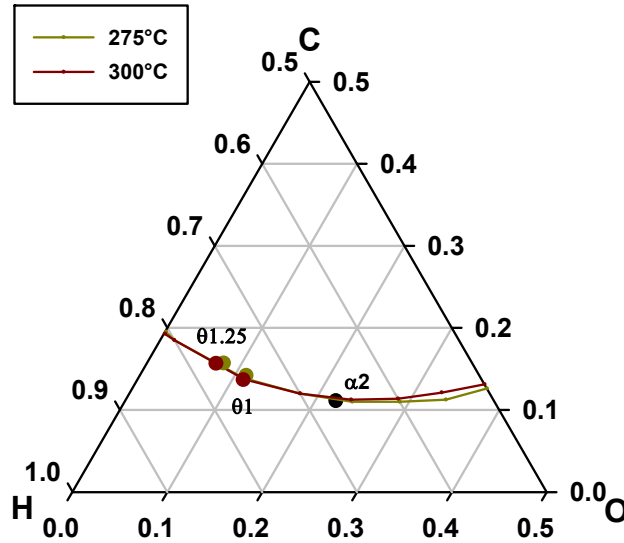


Figure 5.14 C-H-O ternary diagram with carbon deposition boundaries at 275 and 300 °C (at 1 atm) and three compositions of the gas: the feeding at $\alpha=2$ (α) and the outlet for $\theta=1$ and $\theta=1.25$ at 275 °C (dark yellow point) and 300 °C (dark red point)

The feeding condition for $\alpha=2$ is critical from a thermodynamic point of view: the gas composition in the ternary diagram is located close to the isotherms. During the process analyzed, the points representing the gas composition shift as H_2O and CO_2 are subtracted from the system, however, for both temperatures, they remain close to the isotherms, at least for the θ values of interest. At this point, a sensitivity on α between the two conditions $\alpha=3$ and $\alpha=2$, i.e. the stoichiometric and sub-stoichiometric cases, was carried out, to identify a possible intermediate behavior enabling both grid injection (found for $\alpha=2$) and outlet composition excluding, thermodynamically, carbon deposition as in the case of a stoichiometric gas feed. Under this latter condition, in fact, the gas composition always remains below the carbon formation boundaries when increasing θ , as shown in the ternary diagram below (figure 5.15). The diagram reports the stoichiometric gas feed point ($\alpha=3$) and the points corresponding to θ equal to 2, i.e. the maximum value considered, at 275 °C (dark yellow symbols) and 300 °C (dark red symbols).

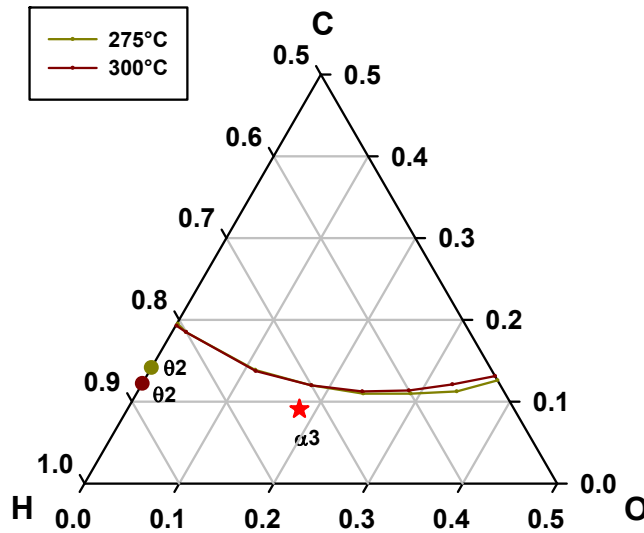


Figure 5.14 C-H-O ternary diagram with carbon deposition boundaries at 275 and 300 °C (at 1 atm) and three compositions of the gas: the feeding at $\alpha=3$ (α_3) and the outlet for $\theta=2$ at 275 °C (dark yellow point) and 300 °C (dark red point)

The sensitivity on the α value showed that for a temperature of 300 °C, only a value of α just slightly higher than 2, results in outlet mixtures whose H₂ content is above the limits for the SEM conditions evaluated. On the contrary, at 275 °C a wider range of possible feed ratios, giving outlet streams quality matching the specifications, was found. However, also in this case, the optimal SEM conditions in terms of stream quality are represented by points collapsing on the isotherm at 275 °C. The graph below (figure 5.15) shows this result for the maximum value of α allowed to permit gas grid injection when SEM is performed, i.e. $\alpha=2.3$.

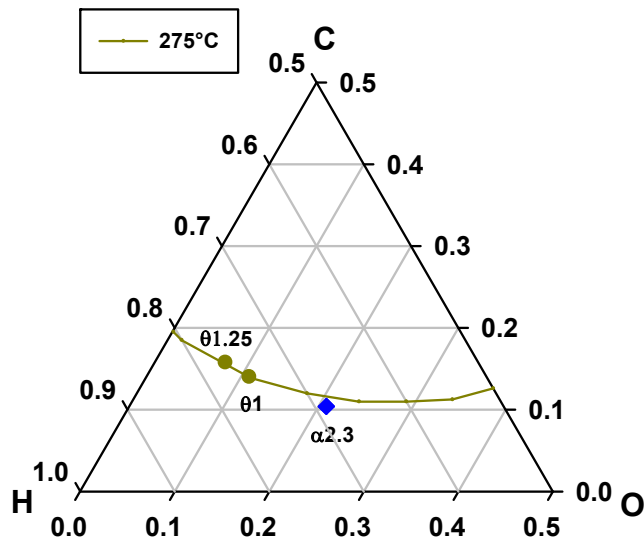


Figure 5.15 C-H-O ternary diagram with carbon deposition boundaries at 275 (at 1 atm) and three compositions of the gas: the feeding at $\alpha=2.3$ ($\alpha_{2.3}$) and the outlet for $\theta=1$ and $\theta=1.25$

To conclude, this analysis revealed that no conditions enabling both the direct injection into the gas grid of the outlet gas and preventing the possible carbon formation can be found. It can be highlighted, though, that SEM in fluidized bed may ensure a significant advantage with respect to other technologies due to the efficient temperature control, namely limiting the rate of carbon generation, which should be quite low for the chosen temperatures as reported elsewhere in the literature [81]. A specific experimental investigation would be, obviously, required to confirm this hypothesis, also considering that the presence of CaO and of the related products, Ca(OH)₂ and CaCO₃, may have an influence on carbon deposition.

As a final consideration, it must be highlighted that the results reported in this section should be carefully treated with regard to the output values reported. In fact, the kinetic expressions used for carbonation and hydration reactions are subject to a number of approximations: first, they have been obtained using specific limestones and specific operating conditions, and it is well known that different limestones and different operating conditions may determine a largely different behavior; second, they have been arbitrarily averaged along conversion degree to be inserted into Aspen, and they do not consider the evolution of diffusional resistances with particle conversion; finally, they do not consider mutual effects when both reactions are active at the same time. These approximations, together with the steady state nature of the Aspen simulations make impossible a comparison with the experimental results reported in Chapter 7, which have been obtained in batch tests.

Although the experimental investigations on water capture capacities also involved zeolites as a possible sorbent material, their behavior was not simulated with Aspen Plus in contrast to the case of CaO. This was due essentially to a lack of steam adsorption kinetic data on zeolites in the literature. However, it is reasonable to assume that, at least qualitatively, similar results as those found for the case in which the carbonation reaction was neglected, should be expected.

6 Experimental investigations: materials, apparatus and procedures

6.1 Sorbents evaluated to perform SEM

Three materials were studied as sorbents: calcium oxide (CaO), zeolites 3A and 4A. The CaO used was produced by calcination of the Italian Massicci limestone by means of a standard procedure. These limestones are rocks typically found in the central Appennines characterized almost entirely by formations of calcium carbonate. The mineral is quite pure with absence of discontinuity, making it suitable for many purposes in industries and to produce cements and filters. The lime was prepared in a laboratory-scale fluidized bed reactor loaded with 150 g of silica sand, heated up to 850 °C and fluidized at a velocity of 0.5 m/s. The bed of inert material (silica sand) used in these reactors acts as a buffer and thermal flywheel. For each preparation process, 20 g of fresh limestone, sieved in the size range 400-600 µm, was introduced into the reactor when the set-point temperature was reached. The complete calcination was achieved in about 10 min. The sorbent was separated and sieved again in the particle size range 400-600 µm, obtaining a yield of approximately 12 g of CaO (figure 5.1). Each prepared sample was subjected to a thermogravimetric analysis (LECO Thermogravimetric Analyzer model TGA701) to assess the degree of calcination. This analysis performs the measurement of the weight loss of a sample as a function of temperature in a controlled environment. The instrument used consists essentially of a multi-sample furnace and a balance, connected to a proper software to monitor the whole analysis. The weight, as well as the temperature and the change in weight percentage, are recorded continuously over time. The method used involved two heating steps (5 °C/min) in air: a first one from room temperature up to 500 °C to calculate the hydroxide contained in the sample and a second heating step up to 850 °C to obtain the CaCO₃ content. The hydroxide and carbonate fractions were always less than 1%. CaO is supposed to react reversibly with steam in the temperature range of interest for methanation resulting in a chemical absorption ($\text{CaO} + \text{H}_2\text{O} \rightarrow \text{Ca}(\text{OH})_2$). A sensitive aspect that may limit the use of CaO is represented by the reaction of carbonation in an environment with CO₂: $\text{CaO} + \text{CO}_2 \rightarrow \text{CaCO}_3$. This reaction, unlike the CaO hydration reaction, is irreversible in the temperature range of interest. In figure 6.1 the prepared CaO is depicted.



Figure 6.1 CaO sieved in the range 400-600 μm

On the other hand, zeolites form a large class of microporous minerals widely used in ion exchange applications, heterogeneous catalysis and as sorbents and molecular sieves. They are tectoaluminosilicates with crystalline structures of TO_4 tetrahedra (T=Si, Al, etc.): adjacent tetrahedra share the oxygen atoms. The general formula is $\text{MeAl}_m\text{Si}_n\text{O}_2(m+n) \cdot z\text{H}_2\text{O}$ where Me represents a metal cation of valence m. Figure 6.2 reports the general tetrahedral structure.

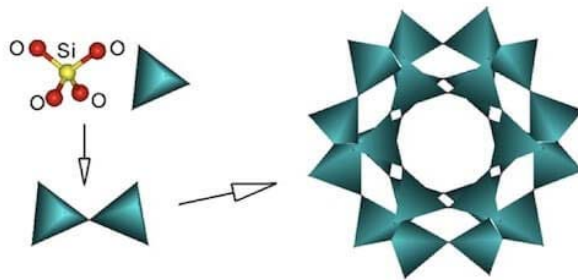


Figure 6.2 General zeolite structure [82]

The T/oxygen ratio results to be 1:2, like, for example, in SiO_2 . The three-dimensional structure is given by the combination of 4-, 6- and 8-membered rings resulting in different cages. By way of example, the sodalite cage is the main element of a series of zeolites that present rings with 4 or 6 members: this combination opens the structure and increases the cavities size (see figure 6.3).

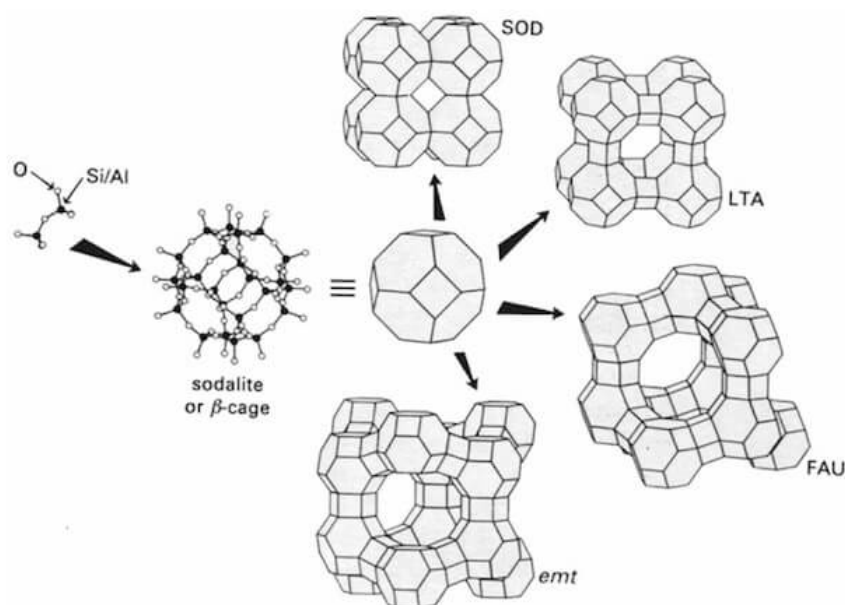


Figure 6.3 Examples of zeolites with sodalite cage [82]

The T-O-T angles vary from 125 to 180 ° so that the resulting materials can range from amorphous to crystalline zeolites. The crystallinity makes them considerably different from other microporous materials, enabling to achieve high selectivity in both catalytic and adsorption processes. The internal pores size is linked to the number of T and O atoms in the rings and can vary from 4 Å to 10 Å. A major characteristic of these materials is the extremely large surface area (typically from 300 m²/g to 700 m²/g) that ensures a wide range of possible catalytic applications. The net composition of the tetrahedron is [SiO₂] and [AlO₂]⁻: the structure has several negative charges equal to the number of Al atoms that need to be balanced by a corresponding number of cations. The Si/Al ratio is always greater than 1. By increasing this ratio, the cations, the density of acid sites and the hydrophilic characteristics decrease, whereas the strength of the single acid site and the hydrothermal stability increase. The zeolites are synthesized starting by aqueous solutions of silicate and aluminate anions mixed with alkali, from which a gel generates after a copolymerization process. The synthesis is often a hydrothermal process (e.g. with high-pressure water vapor) at relatively high pH and can last even several weeks, during which zeolite crystals form from the gel. The Si/Al ratio determines the water interaction and the maximum ion exchange capacity. Water strongly interacts with zeolites with a low Si/Al ratio essentially due to the coordination by cations.

A zeolite A has pore openings of about 4.7 Å: when sodium occupies the sites, the size reduces to 4 Å. The sodium ions can be exchanged with the more voluminous potassium and in such case, the pore size decreases further (3Å) and the zeolites become the 3A. Zeolites 3A pores accept water and ammonia but exclude larger molecules such as CO₂, the reason why they were tested in this work. The zeolite A with the maximum pore size is the 5A, where a partial exchange between sodium and calcium ions enlarges the openings up to 5 Å [82].

The commercial zeolites used are beads of 2-3 mm provided by KÖSTROLITH®: in particular a 4AK with formula $\text{Na}_2\text{O}\cdot\text{Al}_2\text{O}_3\cdot 2.0\text{SiO}_2\cdot n\text{H}_2\text{O}$ and a 3AK with formula $\text{K}_2\text{O}\cdot(1-x)\text{Na}_2\text{O}\cdot\text{Al}_2\text{O}_3\cdot 2\text{SiO}_2\cdot n\text{H}_2\text{O}$ and $x > 0.3$ (figure 6.4).



Figure 6.4 Commercial 3A-zeolites used in the tests

6.2 Catalysts to perform SEM

The chosen material to catalyze methanation was a Nickel based catalyst supported on alumina. As for the support, two commercial materials were used: spherical-shaped alumina of 1 mm (figure 6.5-left) and 600 μm (fig. 6.6-left), specifically purchased for fluidized bed application, having a significant attrition resistance (provided by Sasol). The active phase was obtained by a precursor salt, the Nickel nitrate exahydrate $\text{Ni}(\text{NO}_3)_2\cdot 6\text{H}_2\text{O}$ provided by Alfa Aesar. The preparation method, widely reported in literature for these type of catalysts [83], was the wetness incipient impregnation, also known as dry impregnation: the volume of the aqueous solution prepared is exactly the volume needed to fill the porous structure of the support. Each batch of synthesized material consisted of 10 g of alumina with a corresponding total pore volume of 4 ml: in this amount of water, the precursor was dissolved to obtain a 10%_{w/w} of Nickel after two cycles of impregnation-dehydration. The impregnation stage lasted 2 hours, followed by the dehydration, carried out by means of a heating plate at 95 °C (the materials after impregnation are reported in the figure 6.5-centre and 6.6-centre). The impregnated spheres were calcined (figure 6.5 and 6.6-right) to obtain Nickel oxide; the air calcination was carried out in a fluidized reactor for 1 h at 500 °C, temperature conditions commonly suggested by numerous other studies [83-85]. The active phase (Ni) for methanation is obtained after reduction, carried out in a stream of H_2 and N_2 (4%, 96%) for 1 h at 600 °C in a lab-scale fluidized bed reactor.

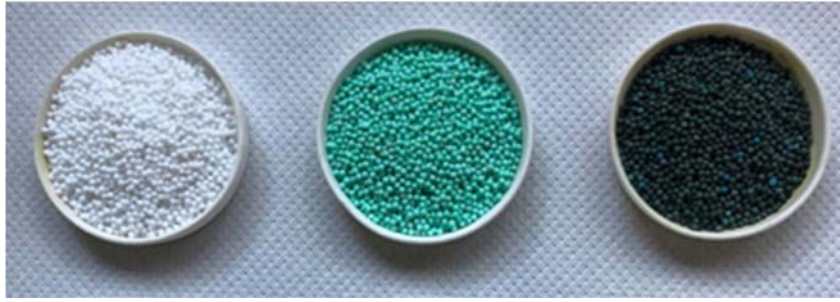


Figure 6.5 Catalysts of 1 mm: support (left); impregnated sample (centre); calcined sample (right)

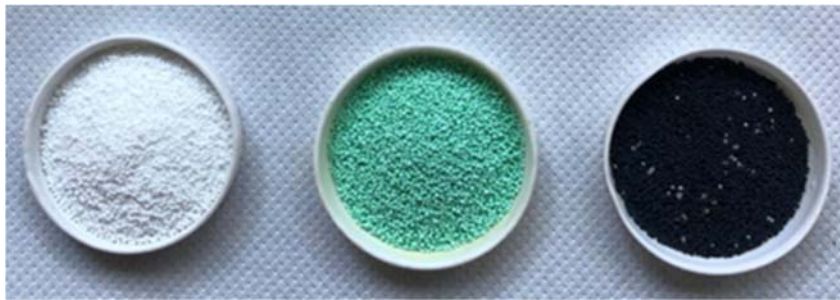


Figure 6.6 Catalysts of 600 μm : support (left); impregnated sample (centre); calcined sample (right)

6.3 Twin Beds experimental apparatus

The experimental apparatus used for the investigations consists of a system called Twin Beds (TB) [86], reported in figure 6.7: two identical reactors, East Bed (EB) and West Bed (WB), interconnected and equipped with flowmeters, steam generator, ovens, and analyzers.

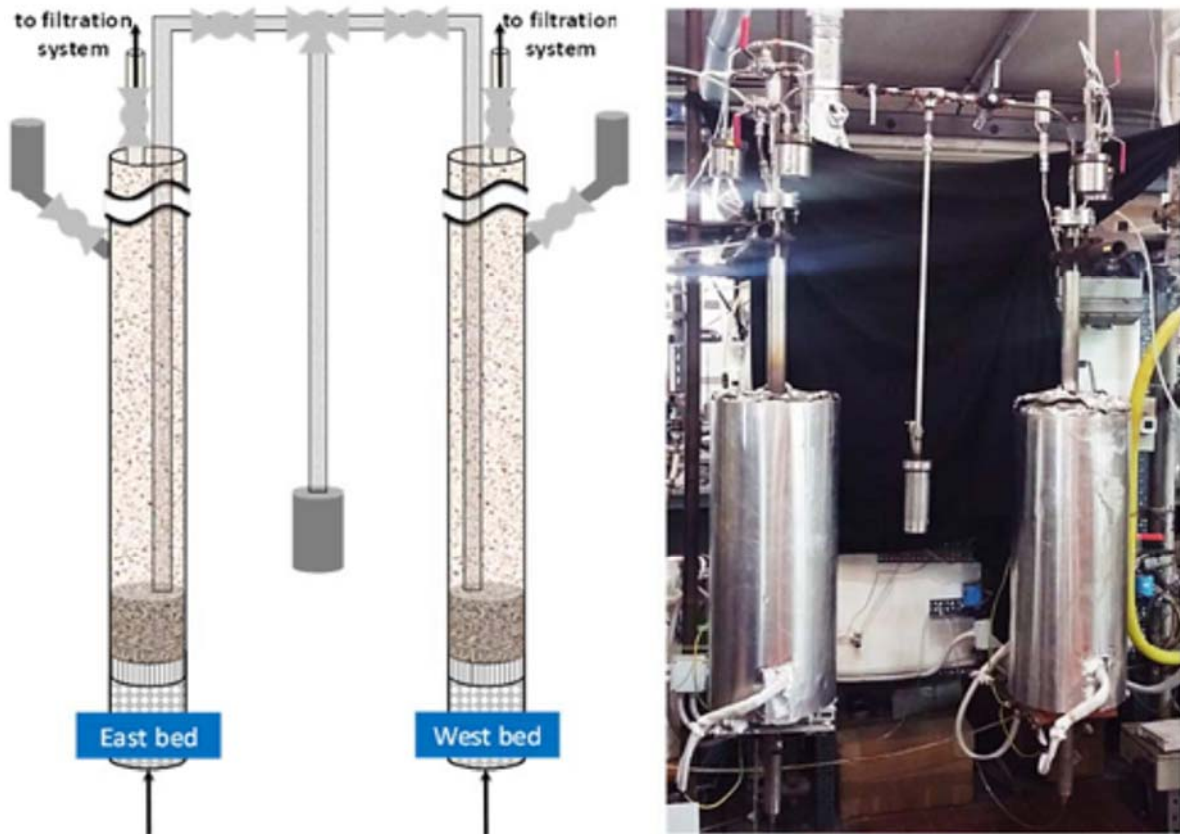


Figure 6.7 Twin Beds apparatus

Each reactor is composed of 3 sections: the wind-box, of 0.66 m, filled with metal elements and acting as a pre-heater/pre-mixer, the fluidization column of 1 m and, in the upper part, a system of a three-way valve that can be connected to the analyzers. This apparatus was conceived with the aim of studying looping processes: it enables the pneumatic transport of granular material in about 5 seconds between the two reactive environments by means of a connecting tube (ID 10 mm) immersed in both reactors. Conventional system such as single fluidized beds (SB) and thermogravimetric equipment (TG), are not able to realize realistic operation, since in these systems a material is subjected to either slow temperature ramps or to cooling and recovering processes at the end of each step. Through the TB and the pneumatic transport is possible to achieve:

- the real "thermal history" simulation of the particles in a looping process
- rapid batch tests

The fluidization column and the wind-box are composed by a tubular steel element (AISI 316) with an internal diameter of 40 mm. Between the two sections, connected by a flange, a perforated plate

is located to uniformly distribute the gas inside the reactor. The plate is made of 55 holes in a triangular pitch of 5 mm: the holes narrow from 1.5 mm to 0.5 mm in the direction in which the gas flows so that the pressure drops are reduced. The gas streams are fed from the bottom and come from Bronkhorst El-Flow controllers. A hopper is placed on each reactor to carry out the bed loading: it has a cylindrical body that narrows getting funnel-shaped, inclined at 120° respect to the horizontal to make the material slide downwards into the reactor. The electrical heating system consists of two semi-cylindrical furnaces on each reactor (Watlow, Ceramic Fiber Heaters) with a heating length of 457 mm and a power per semi-cylinder of 2100 Watts. A PID controller (Watlow, EZ-Zone ST) is connected to each bed via a K-type thermocouple (Cr-Al) inserted 40 mm above the distribution plate. A sleeve of rock wool, tightened with an aluminum sheet, insulates the fluidized zone to ensure the desired temperature. To measure the output concentrations there are different sampling systems. An infrared analyzer (ABBTM, NDIRA02020) is used to measure the CO₂ concentration in the output gas during the sorbents testing; the water vapor concentration can be measured by a humidity sensor (Sensirion SH71X RH/T). The signals from sensor and analyzer are processed using Labview™ acquisition software. An air assisted Bronkhorst CEM (Controlled Evaporator and Mixer) steam generator, shown in Figure 6.8, is connected to the system, producing superheated water vapor, mixed with air, at approximately 200°C. An air flow is supplied to the generator. As for the liquid water, contained in a tank of 4L, it is connected to a liquid flow controller reached using a second air flow that pushes the liquid from the tank against gravity.

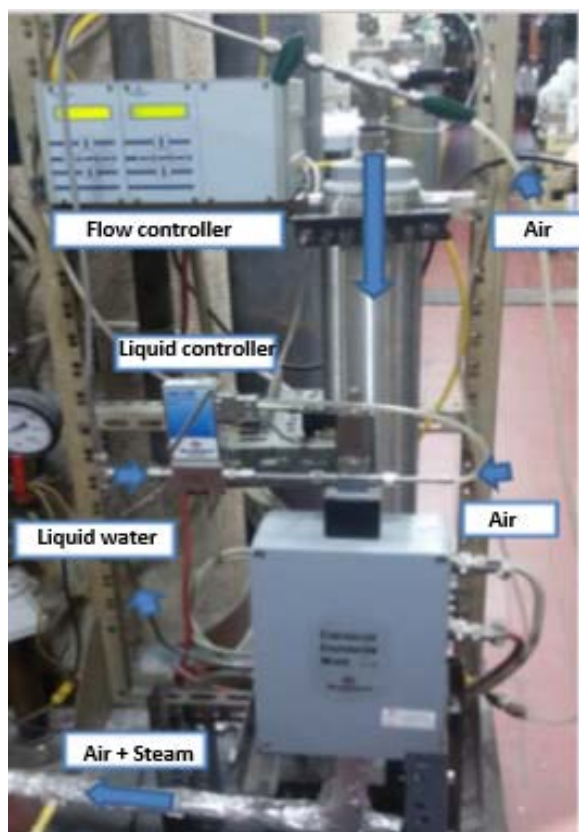


Figure 6.8 Steam generator system

During the methanation tests, the output concentrations of the species are measured by a mobile analyzer (MRU VARIO LUXX) able to detect CH₄, CO, CO₂ by means of a NDIR sensor and H₂ via a TCD sensor.

The pneumatic transport of the solids between the reactors is carried out generating an overpressure by means of a system of valves that enables and modulates the flow of the material. Specifically, as for the transport duct, three valves are present on it: two ball valves close to each reactor (valves 2), which modulate the flow through the duct and a centrally located three-way valve (valve 3) connected to a discharge duct, which allows to direct the material between the two reactors or towards the discharge vessel. Above each reactor, valves 1 allow the outlet gas to be sent to the analyzer system. During a Working Stage, i.e. when the chemical reaction proceeds in one of the two reactors, valves 1 are open and allow the gases to reach the analyzers, while valves 2 are closed (figure 6.9-A). In order to carry out the Transport Stage, valve 3 has to be oriented to allow the passage of the solids between the reactors, while, in sequence, valves 2 are opened and valve 1 of the Working Bed is closed (Figure 6.9-B): the overpressure created in this bed allows pneumatic transport towards the other reactor. After the transfer, valve 1 is opened again and valve 2 closed, starting a new Working Stage in the other reactor. For a Discharging Stage, valve 3 must be positioned so that the material can pass from the Working Bed to the container (Figure 6.9-C) and valve 2 and valve 1 have to be opened and closed, respectively.

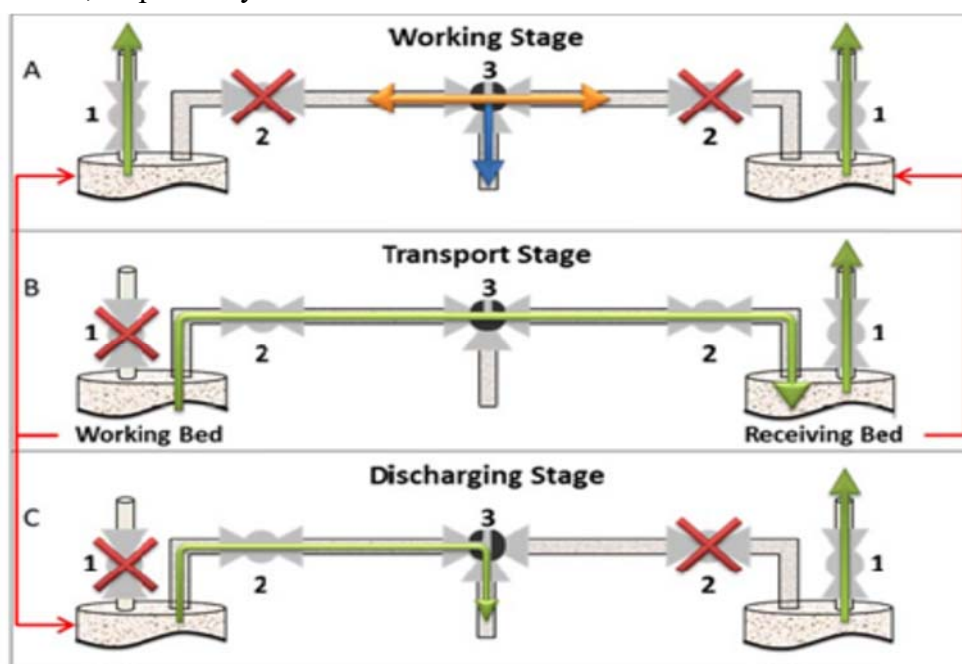


Figure 6.9 Valves relating to A) working stage; B) transport stage; C) discharging stage

6.4 Sorbent hydration testing procedure

The first experimental campaign was aimed at evaluating the water vapor capture and release capacity of the selected sorbents and was carried out varying temperature and reaction environment in the range of interest for methanation. The tests were carried out in the Twin Beds system. The temperature range investigated for hydration was 200-300°C, while that for dehydration was 300-450°C. For all the temperatures considered, two main operating conditions were investigated:

- hydration with 10% steam (balance air), indicated as low-CO₂ tests;
- hydration with 10% steam and 10% CO₂ (balance air), indicated as high-CO₂ tests.

The dehydration was carried out in air. Table 6.1 indicates the different temperature conditions adopted for each sorbent.

Dehydration Temperature (°C)	Hydration Temperature (°C)		
	200	250	300
300	-	-	Z4
350	M/Z3*	M/Z3	M/Z3/Z4
400	M/Z3	M/Z3	M/Z3
450	M/Z3	M/Z3	M/Z3

*M=Massicci lime; Z3=3A-Zeolite; Z4=4A-Zeolite

Table 6.1 Temperature conditions adopted in the tests

The steam concentration during a test of 10 hydration-dehydration cycles was measured at the outlet of the reactors by means of a calibrated humidity sensor (Sensirion-SHT75 Humidity and Temperature Sensor IC). Each step (hydration or dehydration) lasted 10 minutes and the fluidization velocity was set to 0.5 m/s. The steam capture capacity of the sorbent with the number of cycles was expressed as grams of captured H₂O per gram of initial sorbent: in each test 10 g of sorbent material was used. Both reactors were loaded also with silica sand in the size range of 900-1000 micron: 150 g in the hydrator and 100 g in the dehydrator. A different amount was loaded because about 50 g of sand was transported during the pneumatic passage of the sorbent from one reactor to the other, and in that way, the same quantity of sand, in each reactor for each step, was ensured. Sorbent material and sand have different size and density so that they could be easily separated at the end of each stage and could give the desired segregation during fluidization. However, it must be stressed that the presence of sand increases the sorbent attrition phenomena as discussed by Scala et al. [87]. The loaded reactors were heated while gases fluidized them and once the fixed temperature was reached, the sorbent particles were fed via the hopper.

The progress of the hydration was monitored by measuring the percentage of H₂O in the flue gas until the end of the reaction, i.e. when the inlet and outlet vapor concentrations were approximately equal: $C_{(H_2O)}^{IN} \cong C_{(H_2O)}^{OUT}$. The water vapor capture capacity can be expressed as follows:

$$\varepsilon_{H_2O} = \frac{\int_0^{t_f} [F_{H_2O}^{IN} - F_{H_2O}^{OUT}(t)] dt}{m_0} \quad (6.1)$$

where $F_{(H_2O)}^{IN}$ and $F_{(H_2O)}^{OUT}$ are the inlet and outlet mass flow rates of H₂O, respectively, m_0 is the initial mass of the sorbent and t_f is the total time of a single stage of hydration. The mass flow rates were calculated from the inlet and outlet concentrations of H₂O ($C_{(H_2O)}^{IN}$ and $C_{(H_2O)}^{OUT}$) and the volume flow rates (Q_{IN} and Q_{OUT}):

$$\int_0^{t_f} [F_{H_2O}^{IN} - F_{H_2O}^{OUT}(t)] dt = M_{H_2O} \int_0^{t_f} [Q_{IN} \cdot C_{H_2O}^{IN} - Q_{OUT} \cdot C_{H_2O}^{OUT}(t)] dt \quad (6.2)$$

with $M_{(H_2O)}$ the water molecular weight. In practice, the integral was discretized and replaced by the summation:

$$\int_0^{t_f} [F_{H_2O}^{IN} - F_{H_2O}^{OUT}(t)] dt \approx \sum_{i=0}^{t_f} [F_{H_2O}^{IN} - F_{H_2O}^{OUT}(i)] \cdot \Delta i \quad (6.3)$$

where i is the sampling time interval of the concentration signal (1s for all the tests). The amount of total CO₂ was calculated using the same procedure.

As for the tests with CaO, the fragmentation phenomena were investigated by particle size distribution (PSD) analysis, using a series of stacked sieves with aperture size: 0, 53, 112, 180, 212, 250, 300, 355, 400, 600, 710 μ m. The particle mass fraction x_i can be derived as follows:

$$x_i = \frac{m_i(d_i)}{m_{tot}} \quad (6.4)$$

with m_i mass of particles having mean diameter d_i , and m_{tot} the total mass of the sample. This allowed the absolute and cumulative particle size distributions to be obtained. Finally, a thermogravimetric analysis was carried out on the exhausted calcium oxide samples to assess carbonation degree of the treated sorbent with the analysis described in the previous paragraph.

6.5 SEM tests experimental procedure

The SEM experiments were carried out in the already described Twin Beds apparatus. Slightly different procedures were applied for the two sorbents used for SEM, CaO and zeolite 3A. As for the CaO, the methanation/adsorption cycles were performed in the East bed reactor, while the desorption of the hydrated sorbent in the West bed one. The regeneration step was carried out in N₂, lasting 5 minutes at a fixed temperature of 450 °C. Regarding the zeolites, the methanation/adsorption and desorption processes were carried out at the same temperature (300 °C), since a higher temperature (450 °C) would likely determine a degradation of the zeolite structure. For this reason, the cycles, when zeolites were investigated, were performed in the East bed reactor, at 300 °C, switching the gas flow compositions according to the step. This procedure allowed to use, during the process, larger amounts of materials (catalyst plus sorbent), not being subjected to the transfer limits between the Twin Beds imposed by the reactor configuration. In general, for both sorbents, the reactors were heated in air and then the flow was switched to N₂. Before each SEM test, traditional methanation was carried out to set the basis for comparison of the performance of SEM. To perform the conventional methanation in the East Bed reactor, once the temperature was reached, the reduced catalyst was loaded into the reactor, already fluidized with silica sand in the size 800-900 micron. The presence of silica sand is necessary to keep temperature variations to a minimum and to assure the segregation of both sorbent and catalyst to the top of the bed (to perform smooth solids transfer between the reactors). After the catalyst loading, the mixture H₂/CO₂ in the desired ratio, and diluted in N₂ (H₂ lower than 5%_{vol}), was fed to the East Bed. The first traditional methanation and the subsequent cycles of methanation/adsorption lasted 10 min, sufficient to achieve sorbent saturation. Once the first methanation took place, the sorbent material was introduced into the reactor and the cycles started. Four complete cycles of SEM/regeneration were carried out for each test, plus a last fifth SEM after which the materials were discharged and separated by means of sieving. The tables below summarize the operating conditions investigated for the SEM tests with the selected sorbents.

SORBENT MASS (g)	10
SORBENT SIZE (mm)	0.5
CATALYST MASS (g)	10
CATALYST SIZE (mm)	0.6
FLUIDIZATION VELOCITY (m/s)	0.5
SEM TEMPERATURE (°C)	300-350
$\alpha = (\text{H}_2\text{-CO}_2)/\text{CO}_2$ (-)	2-3

Table 6.2 Conditions adopted in the SEM tests for CaO sorbent

SORBENT MASS (g)	50
SORBENT SIZE (mm)	1.7
CATALYST MASS (g)	70
CATALYST SIZE (mm)	0.6
FLUIDIZATION VELOCITY (m/s)	0.5
SEM TEMPERATURE (°C)	300
$\alpha = (\text{H}_2\text{-CO}_2)/\text{CO}_2$ (-)	3

Table 6.2 Conditions adopted in the SEM tests for zeolite 3A sorbent

Velocity and catalyst size were fixed to perform SEM tests with the sorbent material: these two parameters had to be selected to ensure the good mixing of the sorbent with the catalyst. A preliminary test was carried out to investigate such fluid-dynamic aspects in a Plexiglas reactor of 40 mm ID. For CaO (0.5 mm) a good mixing was achieved with the 0.6 mm catalyst already for a fluidization velocity of 0.5 m/s, which was the velocity assessed to ensure the maximum sorbent transport efficiency. In the picture 6.10 it is shown the fluidization established in the above-mentioned conditions. It can be clearly appreciated that the CaO sorbent (white) and catalyst (black) are well mixed in the upper bed zone, while the sand (brown) is mostly segregated in the lower bed zone.



Figure 6.10 Fluidization conditions for a bed of CaO (0.5 mm) mixed with the catalyst (0.6 mm)

In the case of zeolites (1.7 mm), the picture shown in Figure 6.11 represents the mixing established between the catalyst (black) and the zeolite (white) under the fluidization conditions applied in the tests. The granulometry of sand, catalyst and sorbent were chosen to ensure, on the one hand, a good mixing between catalyst and sorbent and a condition of complete separation of them from the sand, and on the other, to ensure an easier separation of materials by sieving. A homogeneous mixing between catalyst and sorbent is essential to obtain a sorption-enhanced methanation, given by the simultaneous methanation reaction and adsorption of water.



Figure 6.10 Fluidization conditions for a bed of zeolites 3A (1.7 mm) mixed with the catalyst (0.6 mm)

The progress of the methanation process was monitored by measuring the concentration of the outlet gases. The mole flows of the species of interest were calculated as follows:

$$F_i^{OUT}(t) = c_i^{OUT}(t) \cdot F_{tot}^{OUT}(t) \quad (6.5)$$

$$F_{tot}^{OUT}(t) = \frac{F_{N_2}}{c_{N_2}(t)} \cdot 100 \quad (6.6)$$

where F_i^{OUT} indicates the molar flow of the outlet species ($i = \text{H}_2, \text{CO}_2, \text{CH}_4, \text{CO}$), c_i^{OUT} their concentration in the stream and F_{tot}^{OUT} the total molar flow exiting the reactor. This latter, from (6.6), is given by the nitrogen balance, with F_{N_2} its (constant) molar flow and c_{N_2} the outgoing nitrogen concentration.

The following performance indicators were calculated for the tests:

$$X_i(t) = \frac{F_i^{IN} - F_i^{OUT}(t)}{F_i^{IN}} \quad (6.7)$$

$$R_{CH_4}(t) = \frac{F_{CH_4}^{OUT}(t)}{F_i^{IN}} \quad (6.8)$$

$$S_i(t) = \frac{F_i^{OUT}(t)}{F_{CO_2}^{IN} - F_{CO_2}^{OUT}(t)} \quad (6.9)$$

where X_i , the conversion, and the methane yield R_{CH_4} , refer to both reactants, $i = \text{CO}_2, \text{H}_2$; the selectivity S_i refers to carbon-containing gas products ($i = \text{CH}_4, \text{CO}$). The total amount of the species could be calculated along a certain time interval ($0-t_f$) discretizing the following integral and replacing it by the summation:

$$\int_0^{t_f} F_i^{OUT}(t) dt \approx \sum_{j=0}^{t_f} F_i^{OUT}(j) \cdot \Delta j \quad (6.10)$$

with Δj the sampling time interval of the signal (1s).

7 Twin beds experimental campaign results

7.1 Performance of CaO sorbent hydration

The CaO steam capture capacity with the number of cycles in some selected conditions, expressed as grams of captured H₂O per gram of initial sorbent, is reported in Figure 7.1(a-c). The 2nd cycle is typically characterized by a higher value of steam capture than the 1st cycle. This is most likely due to the swelling of the particles during the 1st hydration that entails an alteration of the sorbent microstructure with the formation of highly porous CaO after the 1st dehydration step [88]. However, the general trend presents a capture capacity that decreases, after the 2nd cycle, with the number of cycles and reaches an asymptotic value after the 6th-7th cycle. The decay is the consequence of two effects: particle attrition, implying the removal of sorbent material which as fines leaves the reactor with the outlet gas and irreversible carbonation of CaO with the CO₂ contained in the air that consumes active CaO from the sorbent. Overall, in low-CO₂ tests, CaO showed a capture of H₂O in a range of values between 0.01 and 0.14 g(CapturedH₂O)/g(Initial Sorbent).

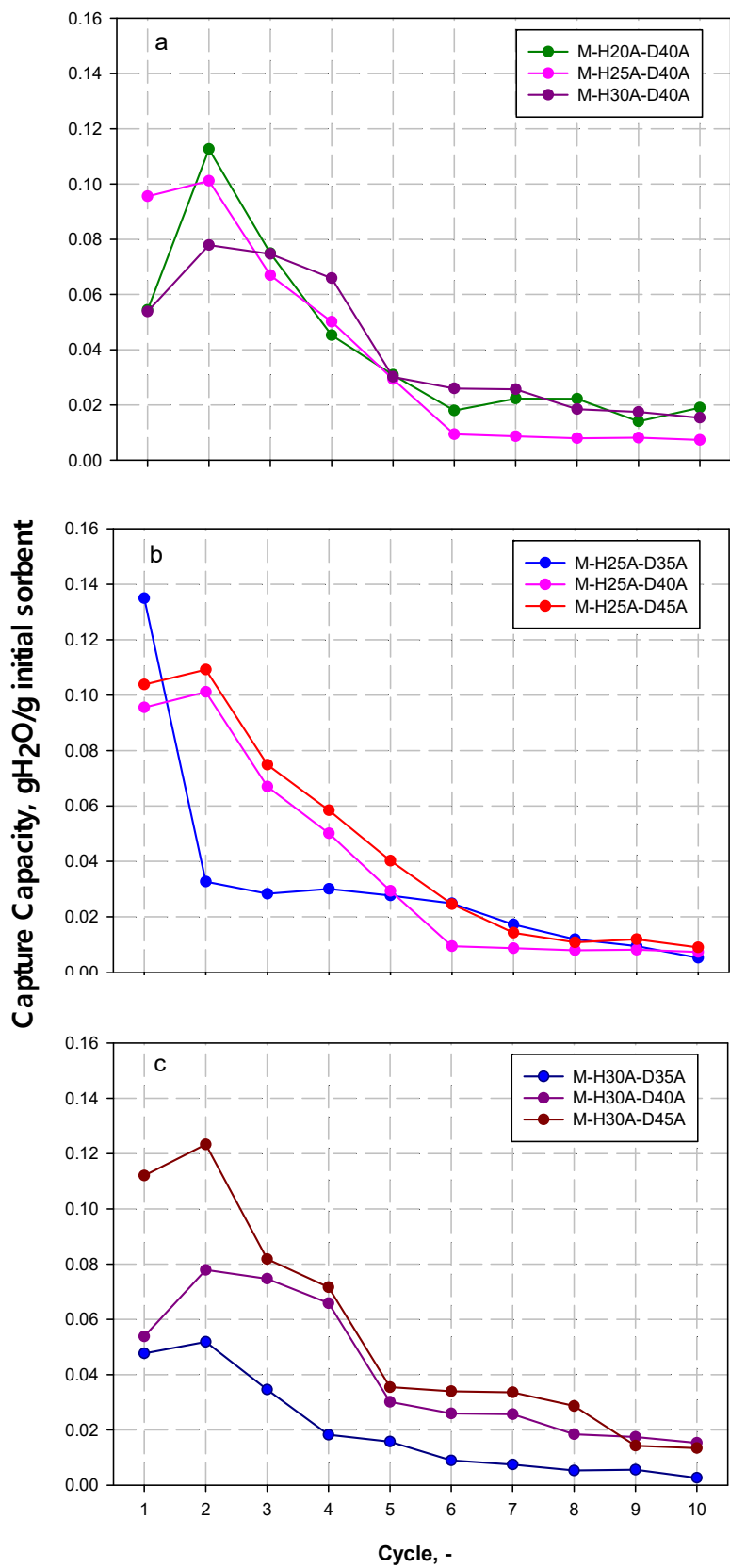


Figure 7.1 H₂O capture capacity of the sorbent with the number of cycles for Massicci CaO

In Figure 7.1-a, the capture capacities at the three hydration conditions (200, 250 and 300°C) are reported for a fixed dehydration temperature of 400 °C to summarize the effect of the hydration temperature. As an example, in the above figure, the acronym M-H25A-D40A identifies one test where the first letter specifies the sorbent Massicci, H25A indicates the hydration step at 250°C in air, while D40A indicates the dehydration step at 400°C in air. The steam capture capacity decreases with the hydration temperature but this difference, evident during the first cycles, tends to vanish with the number of cycles. This behavior may be related to the higher hydration (and carbonation) kinetics which determines the formation of a plugging layer of $\text{Ca}(\text{OH})_2$ and CaCO_3 , hindering the diffusion of steam into the core of the particles. The asymptotic capture capacity values are quite similar among the samples and range around 0.008-0.019 $\text{g}_{\text{H}_2\text{O}}/\text{g}_{\text{sorbent}}$. As regards the effect of the dehydration temperature, two hydration temperatures, 250 and 300°C, were set varying the dehydration ones (350, 400 and 450°C). Results are reported in Figure 7.1 b and c. Generally, increasing regeneration temperatures enhances the steam capture capacity but only during the first cycles. Probably, this is due to the fact that regeneration at higher temperature, implying faster dehydration, determines larger overpressures and induces a more severe breakage of the particles with the formation of new exposed surface for hydration [96]. However, these effects appear to be more relevant at the highest hydration temperature, in particular during the first cycles: in order to show that, Figure 7.1 b and c can be compared.

The effect of the presence of CO_2 was also analyzed, since carbonation reaction may decrease the capture capacity, irreversibly. As for the steam capture capacity, the following trend is observed: a decay (cycles 1-3) is followed by a slight increase that brings to more stable values for the last cycles. This increase is likely due, again, to the occurrence of fragmentation that generates smaller particles with a higher surface area exposed to hydration and carbonation. Likewise, CO_2 capture capacities, in fact, show a similar trend. Figure 7.2 reports the H_2O water capacity for all the dehydration temperatures considered, fixing the hydration temperature at 250 °C, confirming what was discussed above on the qualitative behavior of CaO in presence of CO_2 .

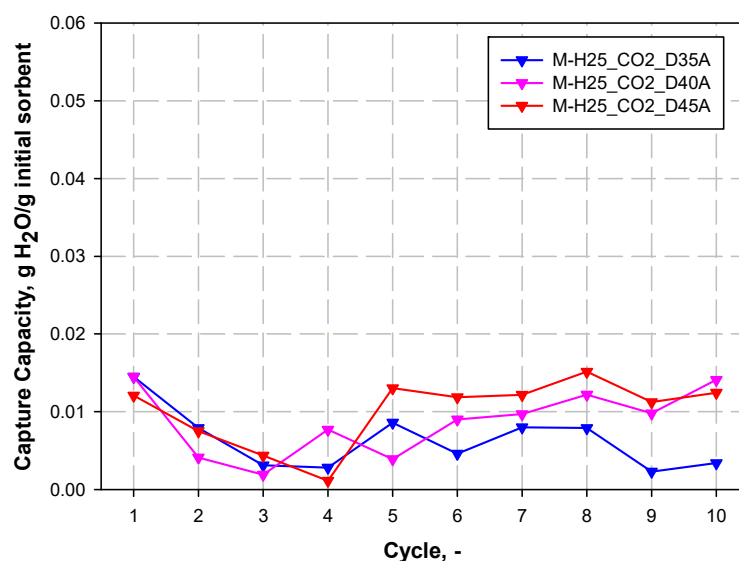


Figure 7.2 H_2O capture of CaO for high- CO_2 tests

Still, for direct comparison, Figure 7.3 reports the steam capture capacity of the CaO for the tests at 10% inlet CO₂ concentration during the hydration and the tests performed in air at a fixed dehydration temperature of 400 °C. High concentration of CO₂ depresses the hydration capacity of the sorbent, especially during the first 5 cycles: the relative curves are essentially flat with a value of the hydration capture which is around 0.015 gH₂O/g_{sorbent}. This is most probably due to the fact that the carbonation of the particle determines a compact external layer which limits the microstructural changes upon the first hydration/dehydration cycles. However, the asymptotic capacity appears to be stable and only slightly lower than the one found in the low-CO₂ tests.

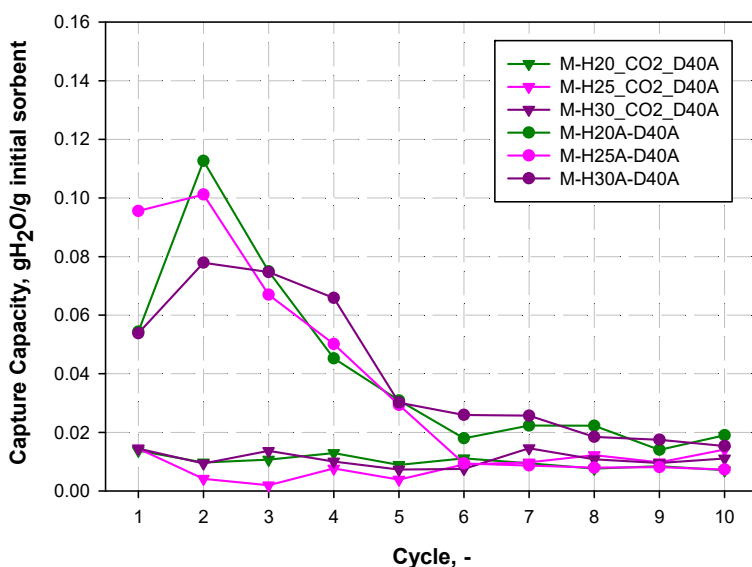


Figure 7.3 Comparison of the H₂O capture capacity for low-CO₂ and high-CO₂ tests

Besides the steam removal capacity, also the CO₂ capture capacity of Massicci CaO with the number of cycles was measured during high-CO₂ steam capture tests and it is reported in Figure 7.4 for the different hydration temperatures. The effect of temperature appears to be significant only in the first cycle, after which the CO₂ captured per cycle was not appreciably influenced by the hydration condition and was slowly decreasing with the number of cycles. This result can be explained considering kinetics: in particular, the carbonate layer growth affects the carbonation reaction rate and this rate may be progressively driven by the CO₂ diffusion resistance in the layer which does not depend on temperature and decreases as the carbonate layer thickness increases.

In Figure 7.5 the cumulative amounts of CO₂ captured at the end of the tests at low-CO₂ and high-CO₂, measured by the TG apparatus, are compared. In this figure, also the residual amount of H₂O in the sorbent is reported. In this last case, however, it is needed to recall that the exhausted sorbent analyzed is the material discharged after the dehydration stage: the mass fraction just includes the non-released H₂O or possibly the H₂O captured by ambient air during the discharge stage, since, despite the rapid procedure, it is not possible to completely avoid any contact with ambient air.

As for the CO₂, the amount captured during high-CO₂ tests was one order of magnitude larger than that captured during low-CO₂ tests, however, the effect on the steam capture capacity was not as dramatic as expected (see figure 7.3).

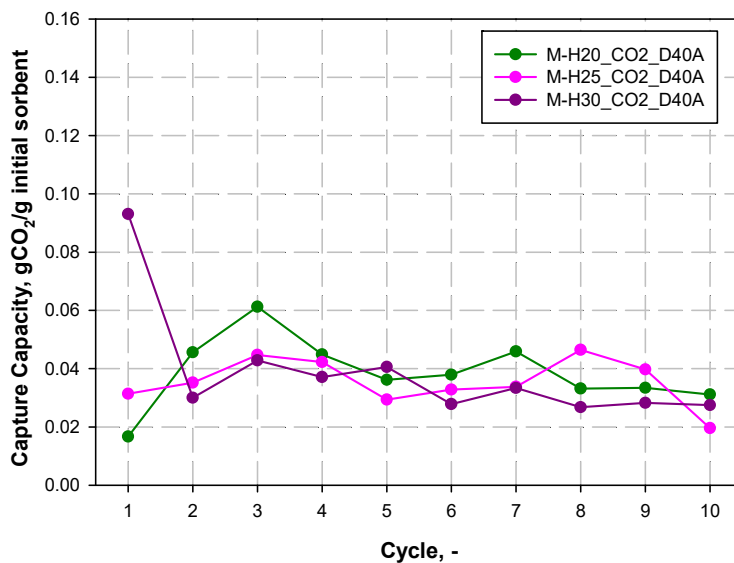


Figure 7.4 CO₂ capture capacity of Massicci CaO for high-CO₂ tests

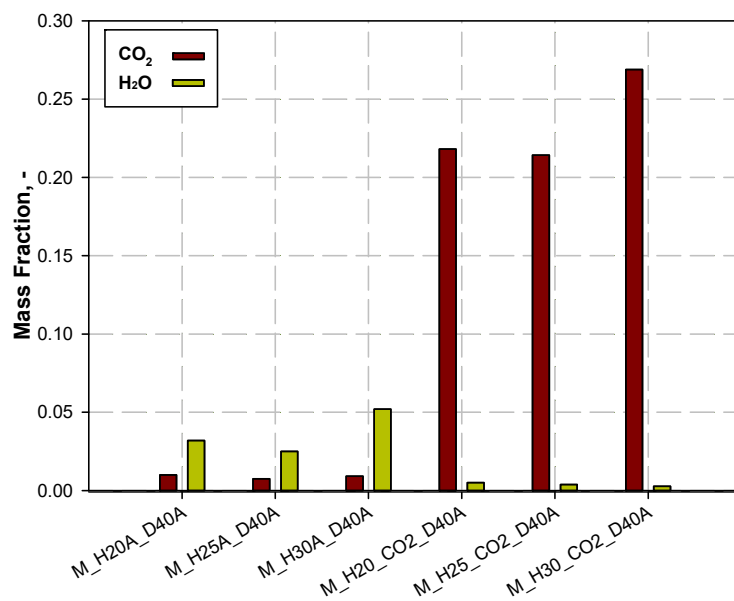


Figure 7.5 Comparison of the CO₂ and H₂O mass fractions at the end of the cycles for low-CO₂ and high-CO₂ tests

The particle size distribution of CaO particles at the end of the tests at low-CO₂ and high-CO₂ was measured and shown in Figure 7.6: the clear bimodal distribution indicates the occurrence of particle fragmentation during the tests. The first peak, always much higher than the second one, corresponds to the initial particle size (0.5 mm), the second peak corresponds to the average fragments size (0.33 mm). This difference between the peaks suggest that fragmentation is not negligible but limited in extent. Comparing the two series, i.e. tests at low and high-CO₂, it can be noticed that fragmentation is significantly depressed under high-CO₂ conditions due to the formation of a tough carbonate surface layer. Instead, the hydration temperature seems to have a very limited effect on the results.

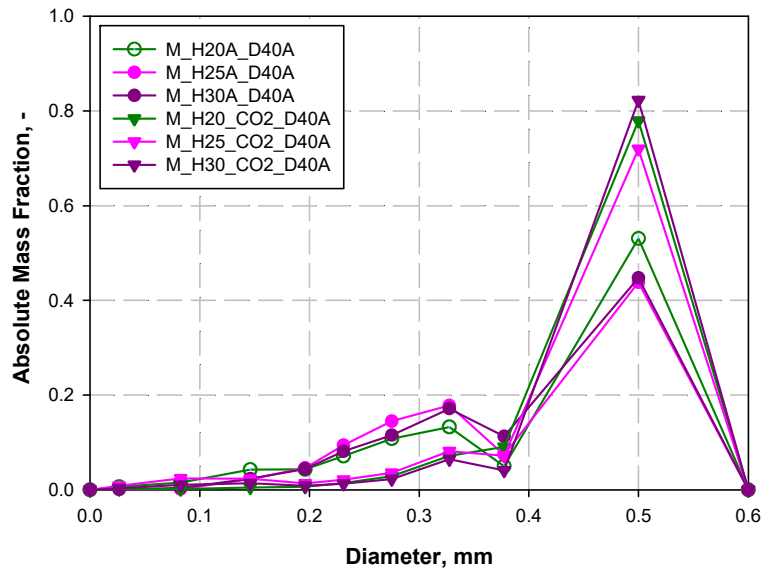


Figure 7.6 PSD of Massicci CaO particles at low-CO₂ and high-CO₂ tests

7.2 Performance of zeolite sorbent hydration

As for zeolites, they present a quite stable H₂O capture behavior along the cycles: a very small increase of the capture capacity during the first cycles indicates a sort of slight activation. Similar to CaO, the influence of the hydration temperature was observed when reporting three tests at a fixed dehydration temperature of 400°C in Figure 7.7-a. Physical absorption of H₂O worsens at higher temperatures, therefore a negative influence of hydration temperature can be observed: in particular, for the test Z-H30A-D40A, which shows an average capture value of about 0.022 g/g, compared with 0.044 and 0.049 g/g for Z-H20A-D40A and Z-H25A-D40A, respectively. In Figure 7.7-b and 7.7-c, the dehydration temperature effect was examined for two different fixed hydration temperatures, 250 and 300 °C. For hydration temperature set to 250 °C (Fig. 7.7-b), the increase of the dehydration temperature seems to have a limited effect until 400 °C (average values of 0.046 and 0.049 g/g for ZH25A-D35A and Z-H25A-D40A, respectively). The chemical degradation of the sorbent, probably related to the release of the structural water contained in the zeolite, most likely causes a remarkable decay of the capture capacity at 450°C (average value of 0.022 g/g for Z-H25A-D45A). As for the highest hydration temperature considered of 300°C, it can be seen in Figure 7.7-c that the capture capacity recorded a decay for all investigated dehydration temperatures: the average capacity values were 0.017, 0.022, and 0.024 g/g for the tests Z-H30A-D35A, Z-H30A-D40A, and Z-H30A-D45A, respectively. Probably, the hydration temperature limits from a thermodynamic point of view the physisorption of water as detected for the tests at different hydration temperatures (see Figure 7.7-a): this effect is more pronounced when the difference between the hydration temperature and the dehydration one, decreases.

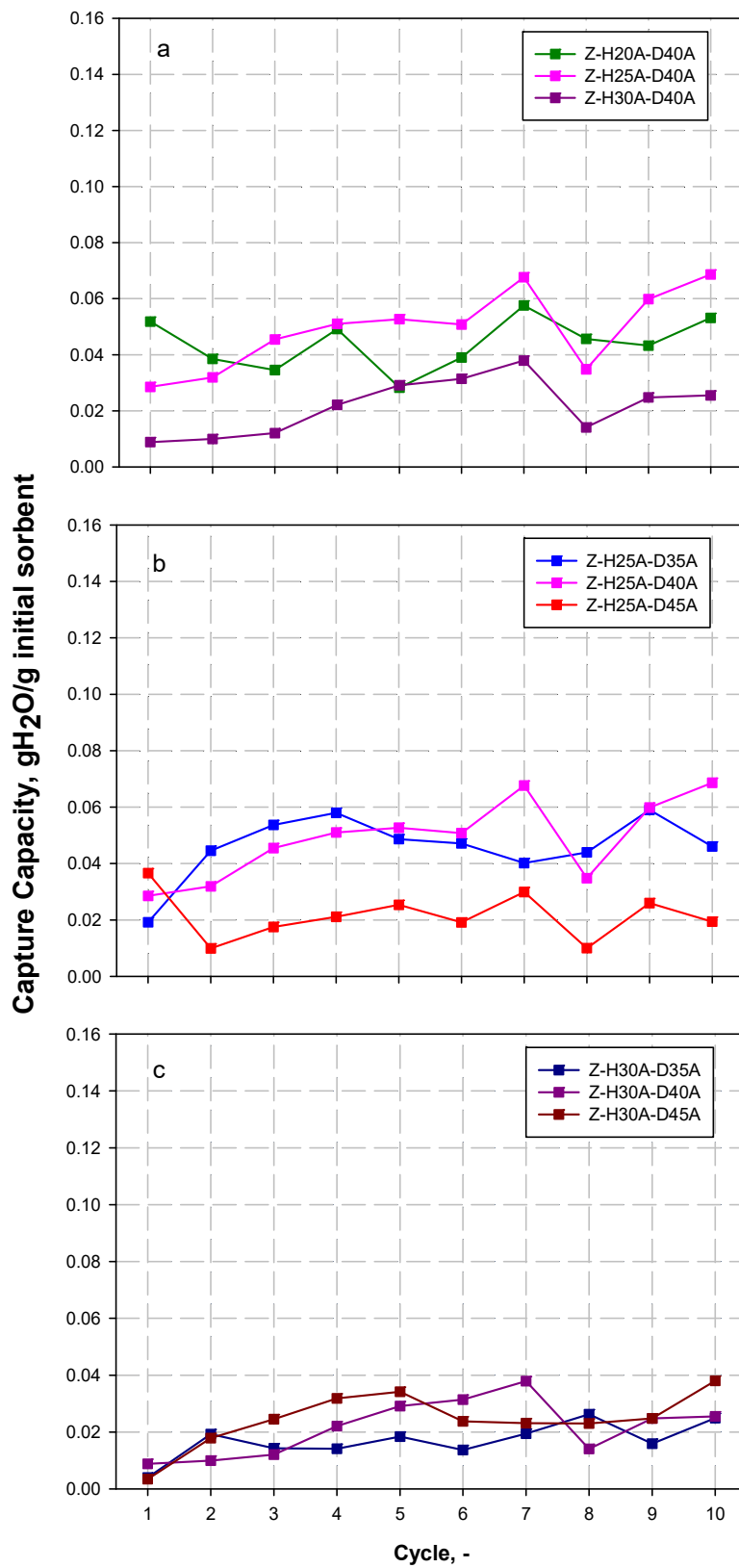


Figure 7.7 H₂O capture capacity for 3A-zeolite

The same investigation at high-CO₂ concentration (10%) also for 3A-zeolite was carried out. Firstly, although the 3A-zeolite pore size should prevent the CO₂ sorption, from 2nd cycle a slight CO₂ removal is observed probably due to a change in the zeolite structure. From the 2nd cycle, water capture capacity slightly decreases due to the competitive CO₂ sorption. Figures 7.8 and 7.9 depict this trend, by way of example, reporting steam and CO₂ capture capacity, respectively: the former reports three tests at a fixed hydration temperature of 300 °C, while the latter three tests at a dehydration temperature equal to 400 °C.

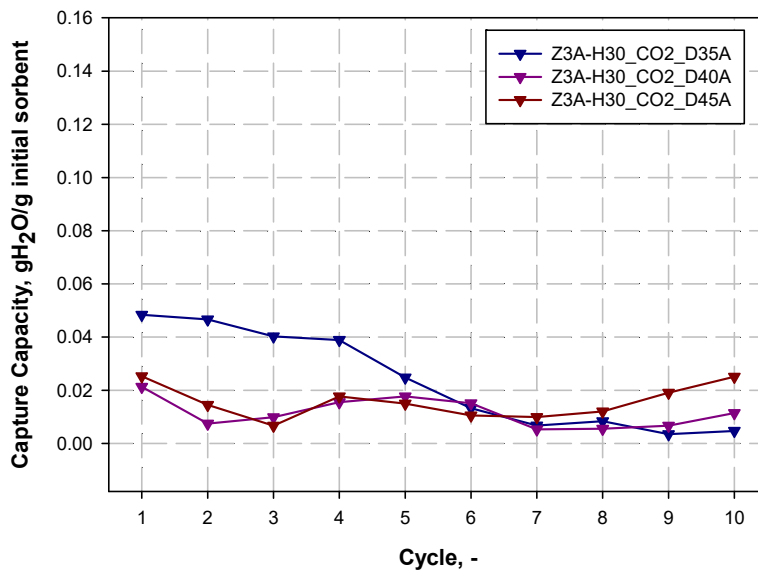


Figure 7.8 H₂O capture capacity of 3A-zeolite for high-CO₂ tests

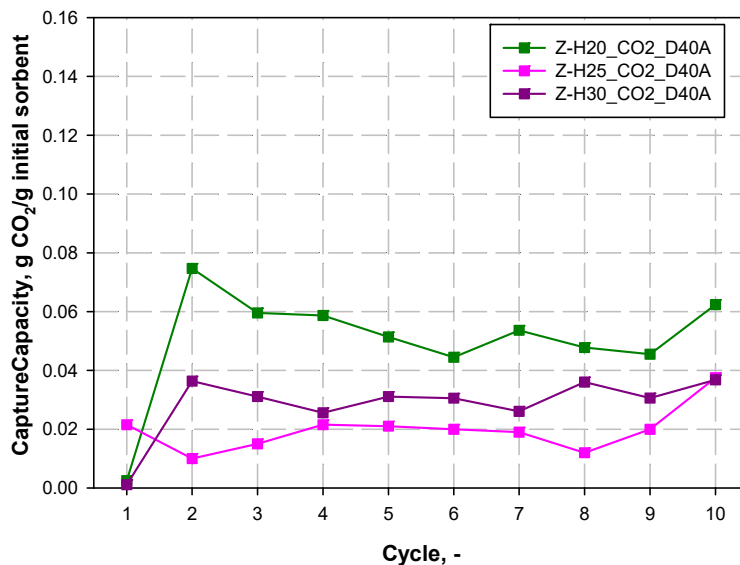


Figure 7.9 CO₂ capture capacity of 3A-zeolite for high-CO₂ tests

Finally, in Figure 7.10 the steam capture capacity with the number of cycles for such tests compared with the tests in the same conditions but at low-CO₂ concentration, is reported.

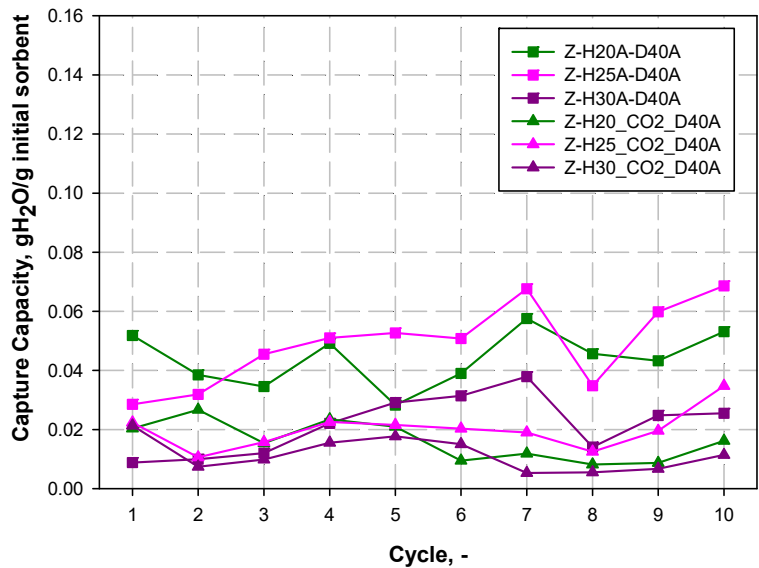


Figure 7.10 Comparison of the H₂O capture capacity of 3A-zeolite for low-CO₂ and high-CO₂ tests

It can be concluded from the Figure 7.10 that the effect of CO₂ on the steam capacity is evident also for the zeolite even if not as dramatic as for the CaO sorbent. This result shows that CO₂ may affect the diffusion of H₂O towards the zeolite surface or even may compete with H₂O for adsorption.

This latter possibility may be confirmed by mentioning again Figure 7.9, where the amount of captured CO₂ per cycle, mostly constant with the number of cycles but not negligible, appeared to decrease with temperature as expected for an adsorption process.

Lastly, the 4A-zeolite was tested for a comparison with the 3A-zeolite. Based on the results achieved with the other two materials, only two conditions were investigated for 4A-Zeolite: in particular, besides the already tested dehydration temperature of 350 °C, dehydration at 300 °C was performed with a hydration temperature of 300°C. This choice was also due to the fact that the commercial Ni-based catalyst starts to be active at about 300°C and the regenerator reactor needs energy, hence low temperatures involve a lower energy consumption for the system. The 4A-zeolite shows a stable behavior with an average value of H₂O capture slightly higher than that of the 3A-zeolite: indeed, for the tests Z4-H30A-D30A and Z4-H30A-D35A values of about 0.022 and 0.021 g/g were recorded, respectively, while for the Z3-H30A-D30A and Z3-H30A-D35A these were 0.017 and 0.018 g/g, respectively. The presence of CO₂ decreases also in this case the H₂O capture capacity. However, the two zeolites present the same capture capacity during the last cycles. Figure 7.11 reports the H₂O capture capacity for all the conditions considered for the 4A-zeolites.

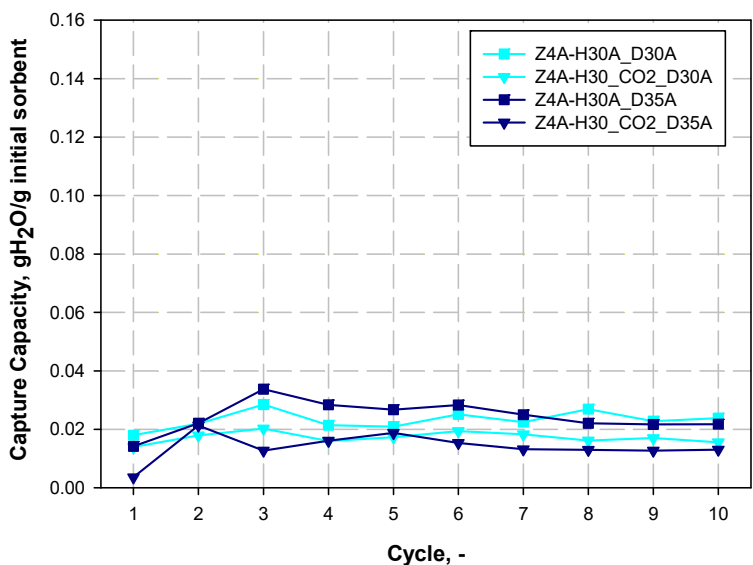


Figure 7.11 H₂O capture capacity of 4A-zeolite

7.3 Conventional methanation

Before conducting SEM tests, conventional methanation was investigated to define baseline results with the used catalyst, and to select feasible conditions to study the sorption enhanced process. Methanation was characterized in terms of the main performance indicators by varying bed temperature and mass and particle size of the catalysts. The analysis was performed for a stoichiometric gas feed ratio, i.e. for a value of the previously introduced parameter α equal to 3. To clarify the behavior of the synthesized catalysts and their activity with temperature, tests were carried out in the lab-scale fluidized reactor (EB of the Twin Beds) evaluating the performance at different temperatures in the range 250-450 °C for different amounts of catalyst (10, 50 and 100 g). The CO₂ and H₂ conversion (X_{CO_2} , X_{H_2}), yield (Y_{CH_4}) and selectivity to methane (S_{CH₄}) and CO (S_{CO}) are reported in figures below (from 7.12 to 7.16) for the Ni-based catalysts on spherical alumina support at two different diameters (0.6 and 1 mm). The catalyst showed to be active from 250 °C, in line with the typical behavior found for most Ni-based catalysts. However, for the lowest amount of catalyst, 10 g, the reactants conversion was negligible at 250 °C. Increasing the catalyst amount, conversion improved quite significantly, reaching a value around 50% at 250 °C when 100 g of catalyst were loaded in the reactor. Above 350 °C equilibrium condition was achieved with 50 g of catalyst: conversion was the same of that obtained with 100 g of catalyst (figures 7.12 and 7.13). The difference between the conversion reached in the reactor and the theoretical equilibrium curve reported in the graphs (for comparison) remains constant in the range 350-450 °C and it is most likely due to gas bypass phenomena occurring in the fluidized beds, as reported in the literature for similar tests [89]. Another possible explanation for this conversion difference might be a slight temperature difference between the bed temperature at the thermocouple location and the top bed surface. The methane yield reached the maximum when the highest mass of catalyst was used, at 300 °C, favored by the thermodynamics of the exothermic reaction (figure 7.14).

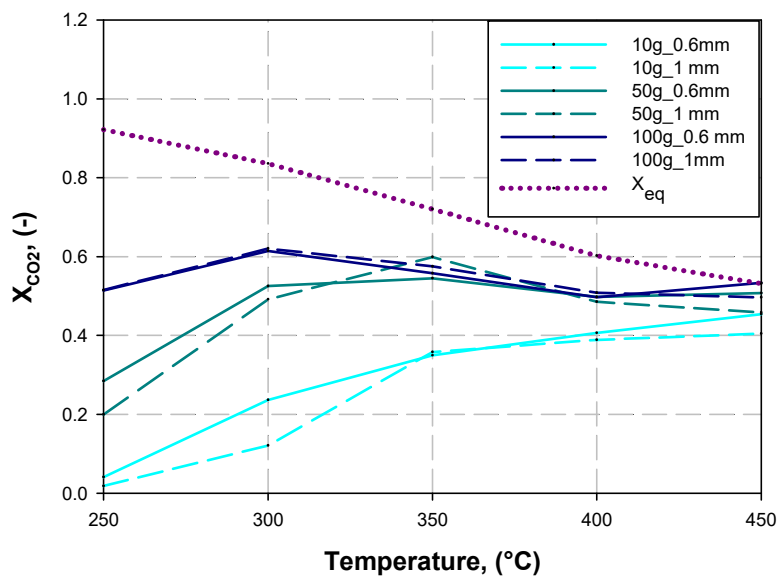


Figure 7.12 CO₂ conversion as a function of temperature for different mass of catalyst (dp 1.0 and 0.6 mm) at $\alpha=3$

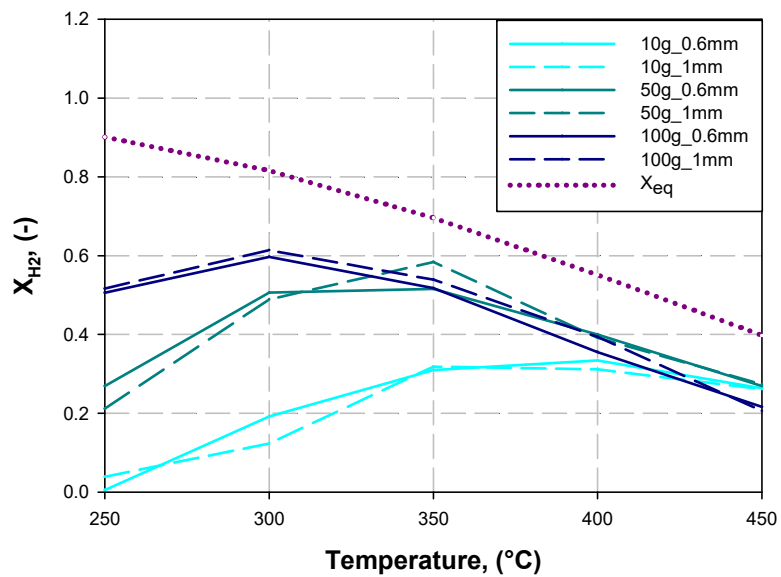


Figure 7.13 H₂ conversion as a function of temperature for different mass of catalyst (dp 1.0 and 0.6 mm) at $\alpha=3$

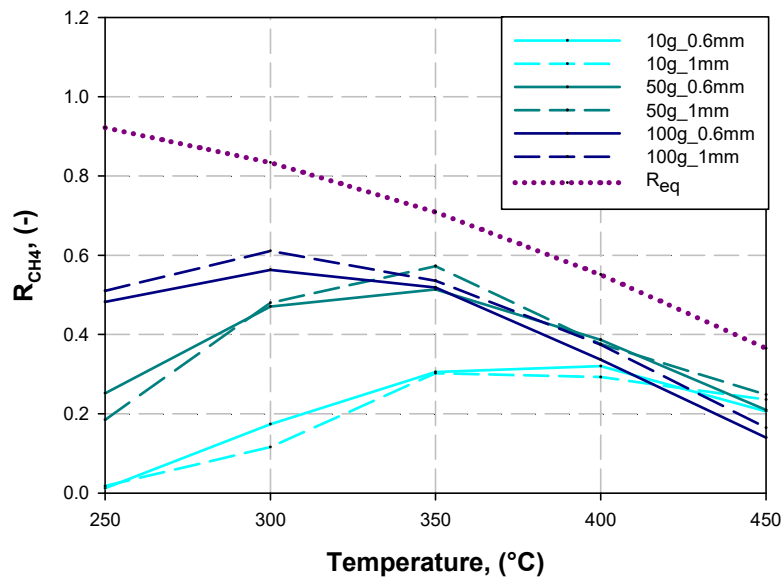
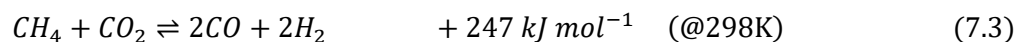


Figure 7.14 CH₄ yield as a function of temperature for different mass of catalyst (dp 1.0 and 0.6 mm) at $\alpha=3$

If considering the catalyst selectivity, when a proper amount of catalyst was used (already for 50 g), negligible quantities of CO were detected in the temperature range of interest (300-350°C) (figure 7.16). The selectivity to methane decreased drastically above 350 °C due to the thermodynamics of the highly exothermic methanation reactions (7.15). Since CO₂ methanation reaction can be schematized as the combination of Reverse Water Gas Shift (7.1) and CO methanation (7.2), the effect of the former, endothermic, starts to affect more and more the equilibrium composition as the temperature increases.



Different side reactions should be taken into account during a methanation process as mentioned and reported in table 4.1 of chapter 4. Among them, coke generation has been found to occur only above 500 °C [80] when a Nickel catalyst is applied. On the contrary, Dry Methane Reforming (7.3) can be promoted by the aforementioned catalyst even at temperature lower than 400 °C and is favored at low pressure [80].



The RWGS and the Dry Methane Reforming may explain the CO production increase at temperatures above 350 °C. In particular, the results showed a more pronounced effect when 100 g, i.e. the maximum amount investigated, of catalyst were used: under these conditions the selectivity to methane was around 70% at 400 °C and dropped to about 30% at 450 °C. If considering only CH₄ and CO as the generated carbon-containing species, the carbon balance closure for the selectivity was quite good in all the test (less than 10% error).

The significant effect of the catalyst mass on selectivity decrease may be explained by a change of fluidization regime. In fact, a higher bed height could generate slugging phenomena with a worsening of the fluidization conditions and an enhancement of the reactions that can occur in the homogeneous phase such as the RWGS. However, it must be highlighted that in the temperature range of interest for SEM (up to 350 °C), the catalyst ensured a high selectivity, close to the equilibrium values. S_{CH_4} turned out to be lower only for the test with 10 g of catalyst: this may be due to insufficient contact times with the catalyst. Finally, it can be pointed out that the two alumina support sizes show basically the same behavior indicating limited diffusive resistances.

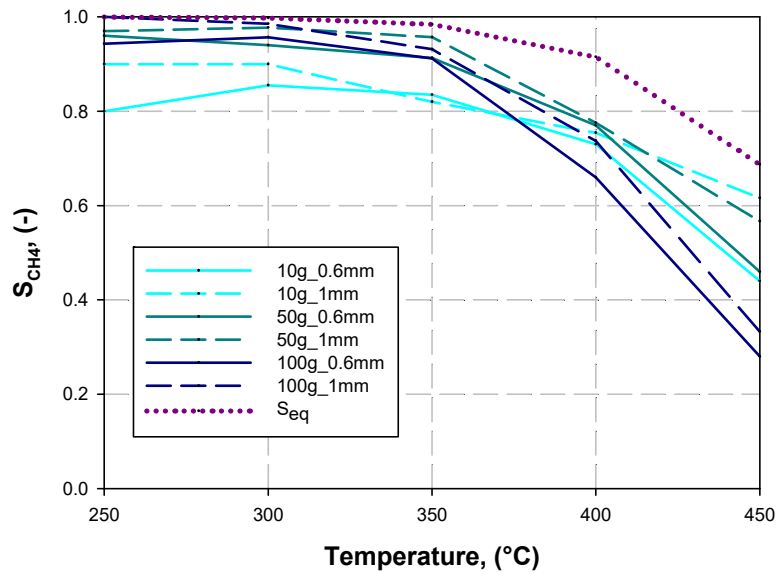


Figure 7.15 Selectivity to CH_4 as a function of temperature for different mass of catalyst (dp 1.0 and 0.6 mm) at $\alpha=3$

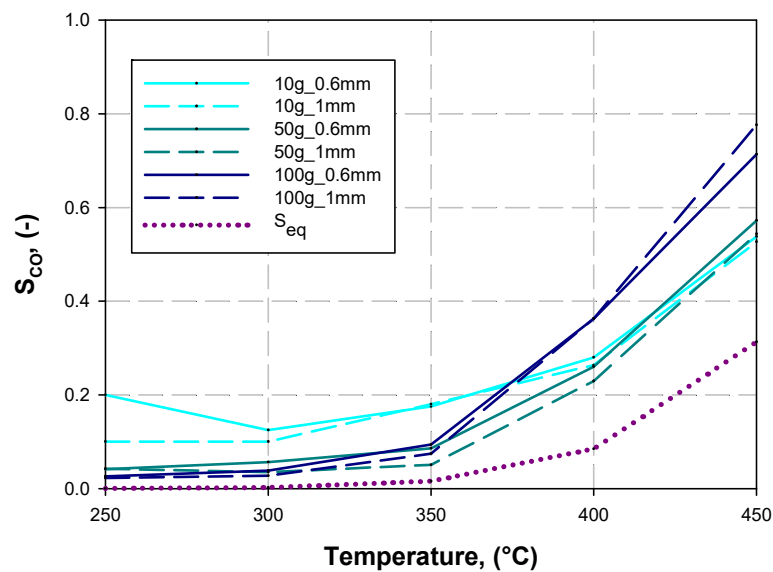


Figure 7.16 Selectivity to CO as a function of temperature for different mass of catalyst (dp 1.0 and 0.6 mm) at $\alpha=3$

7.4 SEM with CaO as sorbent

The results of the methanation tests, expressed as the ratio between the molar flows (mol/h) of outlet CH₄ and of inlet H₂, for a bed temperature of 300°C, are reported in Figure 7.17 (a-b) for different feed ratios ($\alpha = 2$ and $\alpha = 3$, a and b respectively) as a function of time. All the cycles constituting a complete SEM test are depicted: the curves indicated with MET refer to traditional methanation performed before the 5 SEM cycles. Basically, three distinct qualitative behaviours of the curves along the cycles can be identified: 1) the first trend corresponding to conventional methanation; 2) the curve characterizing the first cycle under SEM conditions; and, finally, 3) the behaviour from the second to the last SEM cycles. The black line (traditional methanation) shows an increasing of the CH₄ production with an initial transient behaviour that reaches a stable value after about 240 s. The first SEM cycle (grey line) reproduces a similar trend, which however presents a distinct slowing down in reaching the asymptotic value with respect to conventional methanation. The first SEM cycle behaviour can be explained by the irreversible carbonation that immediately starts, when feeding fresh CaO, and subtracts CO₂ reactant from the desired reaction. As the CaO carbonates, a CaCO₃ shell is gradually formed around the sorbent particles and the reaction rapidly slows down. As early as the second SEM cycle, the “enhanced-behaviour” due to water vapor capture is visible and becomes even more evident in the subsequent three cycles. This trend is characterized by the achievement of a maximum in the CH₄ outlet molar flow that occurs within approximately the first 90 s of the cycle, during which the produced steam is captured by CaO.

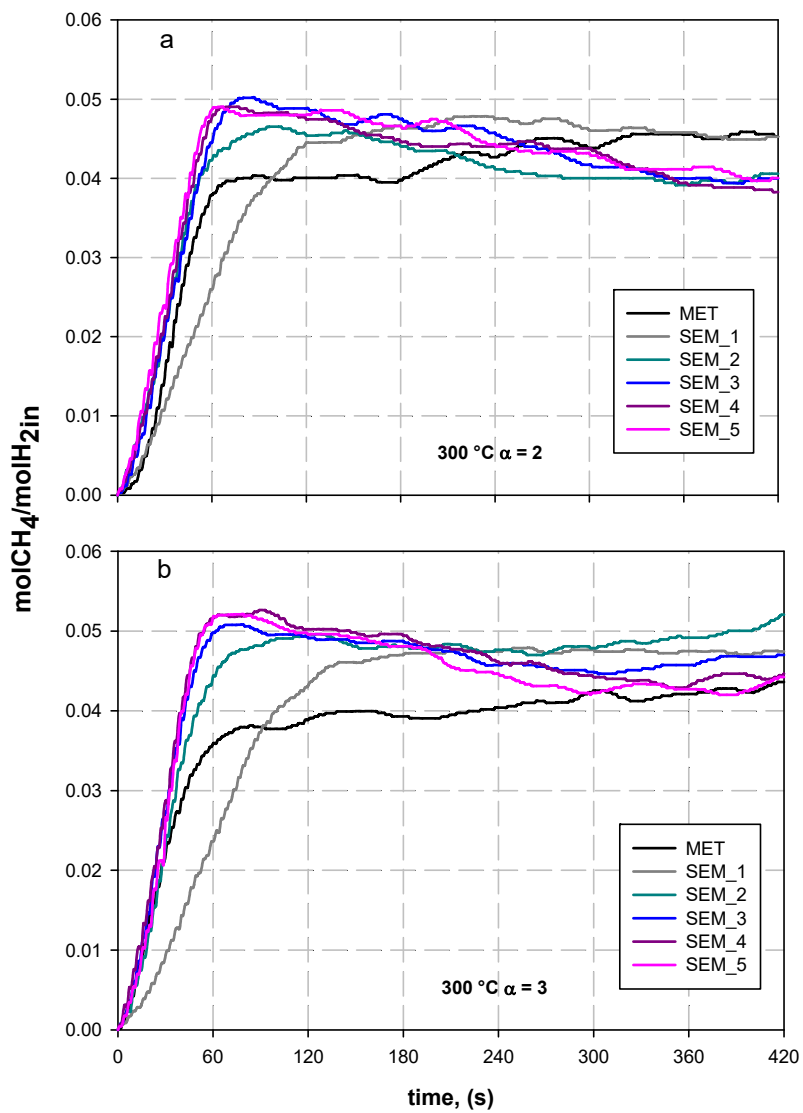


Figure 7.17 Molar flow ratio between outlet CH₄ and inlet H₂ at 300°C for $\alpha=2$ (a) and $\alpha=3$ (b) as a function of time. Catalyst mass = 10g.

The integral amount of the CH₄ produced (with respect to the H₂ fed) in terms of moles, was calculated to quantify the “enhanced-behaviour” effect. For the two α values, Table 7.1 reports the cumulative CH₄ moles calculated at two characteristic times corresponding to the peak of the “enhanced-behaviour” (t_{90}) and the complete saturation of the sorbent and stabilization of the curves to the asymptotic value (t_{210}). The percentage variation in the produced methane with respect to the “MET” case is reported in brackets for both characteristic times. If considering the different gas feed ratios, the largest CH₄ amount was found for $\alpha = 3$, i.e. for the stoichiometric case (H₂/CO₂=4): the higher H₂ concentration effect on kinetics may explain this result.

		$n\text{CH}_{4\text{out}}/n\text{H}_{2\text{in}}$											
		MET		SEM_1		SEM_2		SEM_3		SEM_4		SEM_5	
		t_{90}	t_{210}	t_{90}	t_{210}	t_{90}	t_{210}	t_{90}	t_{210}	t_{90}	t_{210}	t_{90}	t_{210}
$\alpha = 2$		0.0237	0.0331	0.0182 (-23%)	0.0333 (0.34%)	0.0285 (20%)	0.038 (14.6%)	0.0295 (24.6%)	0.04 (20.4%)	0.03 (29.5%)	0.0396 (19.4%)	0.0317 (34%)	0.0408 (23%)
$\alpha = 3$		0.0252	0.0332	0.0165 (-34%)	0.0327 (-1.4%)	0.03 (18.6%)	0.04 (22.3%)	0.0336 (33.3%)	0.0423 (27.5%)	0.035 (39%)	0.0435 (31.3%)	0.0339 (34.5%)	0.0425 (28.3%)

Table 7.1 Ratio of total CH₄ produced to H₂ fed (mol/mol) in each cycle at 300°C, and relative percentage variation with respect to standard methanation (MET).

During the first cycle, the CaO carbonation clearly prevailed over hydration; in fact, a dramatic decrease in the produced CH₄ took place: -23% and -34% at t_{90} for $\alpha = 2$ and $\alpha = 3$, respectively. It can be seen that for $\alpha = 2$, i.e. feeding CO₂ in excess with respect to the stoichiometric value, the negative effect of carbonation in the first cycle was partly compensated. For both α considered, the effect of H₂O sorption was evident, involving a higher amount of CH₄ produced, in all the cycles following the first one: during these cycles, the sorbent was saturated with respect to carbonation and concurrently the hydration effect became stronger. In particular, for $\alpha = 2$ and considering the last cycles, the SEM effect produced an increase of methane formation at t_{210} of around 20%. Moreover, the enhancement corresponding to the maximum CH₄ productivity (t_{90}) was around 30% higher than the increase corresponding to t_{210} . For a stoichiometric feed ($\alpha = 3$), the “overall” enhancement (t_{210}) was even higher than in the previous case, with an average value over the last three cycles equal to about 30%.

The results for the other methanation temperature investigated, 350°C, are reported in Figure 7.18 a-b and Table 7.2, for both gas feed ratios. From the figure, it can be noted that the qualitative trend of the curves presents some differences from that observed at 300°C. Primarily, at 350°C the SEM curves reach more smoothly the asymptotic value with no pronounced maximum in the first part of the cycle. Moreover, in the first SEM cycle, the sorbent needed more time, compared with 300°C, to saturate with respect to the carbonation reaction.

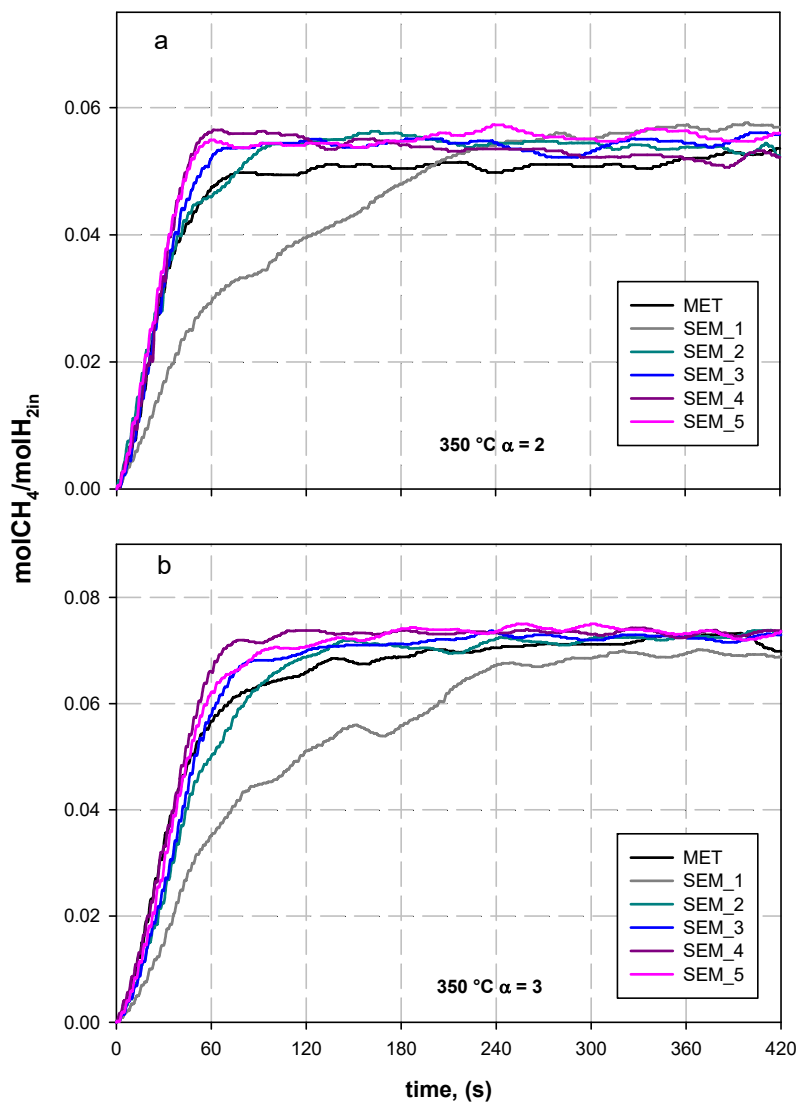


Figure 7.18. Mole flow ratio between outlet CH₄ and inlet H₂ at 350°C for $\alpha=2$ (a) and $\alpha=3$ (b) as a function of time for CaO SEM. Catalyst mass = 10g.

		$n\text{CH}_{4\text{out}}/n\text{H}_{2\text{in}}$											
		MET		SEM_1		SEM_2		SEM_3		SEM_4		SEM_5	
		t ₉₀	t ₂₁₀	t ₉₀	t ₂₁₀	t ₉₀	t ₂₁₀	t ₉₀	t ₂₁₀	t ₉₀	t ₂₁₀	t ₉₀	t ₂₁₀
$\alpha = 2$		0.0339	0.0434	0.0209 (-38.5%)	0.0337 (-22.3%)	0.035 (2.7%)	0.0464 (7%)	0.0364 (7.3%)	0.0468 (7.8%)	0.0389 (14.7%)	0.0479 (10.4%)	0.0387 (14%)	0.0477 (10%)
$\alpha = 3$		0.0397	0.0555	0.0238 (-39.9%)	0.0406 (-26.8%)	0.0345 (-12.9%)	0.0545 (-1.8%)	0.0383 (-3.2%)	0.0567 (2.1%)	0.0443 (11.8%)	0.0608 (9.6%)	0.041 (3.4%)	0.0588 (5.9%)

Table 7.2 Ratio of total CH₄ produced to H₂ fed (mol/mol) in each cycle at 350°C, and relative percentage variation with respect to standard methanation (MET).

At this point, it should be highlighted that SEM tests with CaO were performed using a limited amount of material (sorbent and catalyst) to ensure an optimal transfer between the reactors during the chemical looping. The amount of catalyst was insufficient to reach chemical equilibrium; therefore, the visible effect was linked to an increase of the reaction kinetics. Such effect led to a greater CH₄ production during each cycle at 350 °C with respect to the 300 °C case. For example, the total amount of CH₄ produced at $\alpha = 3$ in the last two cycles amounted to 0.0074 moles and to 0.0057 moles at 350 and 300°C, respectively. On the contrary the increase during the last cycles in CH₄ productivity due to the SEM effect was found to be lower than that found at 300°C. The maximum enhancement, around 10%, was reached for $\alpha = 2$. Different reasons may concur to this result, which can most likely be explained as due to a stronger influence of the carbonation reaction coupled with the thermodynamic limit on the hydration reaction of CaO that worsens by increasing temperature. However, the influence of the operating conditions on the kinetics and thermodynamics of both the carbonation and hydration reactions of CaO and the related results, calls for a more in-depth analysis in future work.

7.5 SEM with zeolite as sorbent

The SEM test results using the zeolite 3A are shown below. The process was conducted only at a temperature of 300 °C, since this sorbent ability to capture water strongly decreases with increasing temperature and hydration tests showed that already above 300 °C a worsening occurred. Moreover, with this sorbent carbonation does not occur, so that has no sense to operate under sub-stoichiometric feeding. So the investigation with zeolites was only carried out at stoichiometric conditions, $\alpha = 3$. From the following graph, Figure 7.19, is possible to distinguish two principal trends which correspond to simple methanation (MET), and SEM cycles. The simple methanation curve shows the usual initial transient behaviour, reaching a stable value after about 180s. The other curves instead reach a maximum in the production of methane, after about 75s. During this phase, the zeolite adsorbs the water vapor produced until its saturation. The SEM curves reproduce an almost identical trend during the first three cycles, whereas the peak value slightly decreases in the last two ones. In table 7.3, the "enhancement effect" due to the addition of the zeolite can be quantitatively appreciated; in detail the effect is evaluated at two characteristic times: 75s, when the peak takes place, and 180s, when a stable value is reached. The enhancement corresponding to the peak is on average equal to 20% along the first three SEM cycles. This percentage slightly decreases in the last two cycles (16.8% and 14.4%): this may be due either to a decay of the sorption activity or to an incomplete water removal in the dehydration phase.

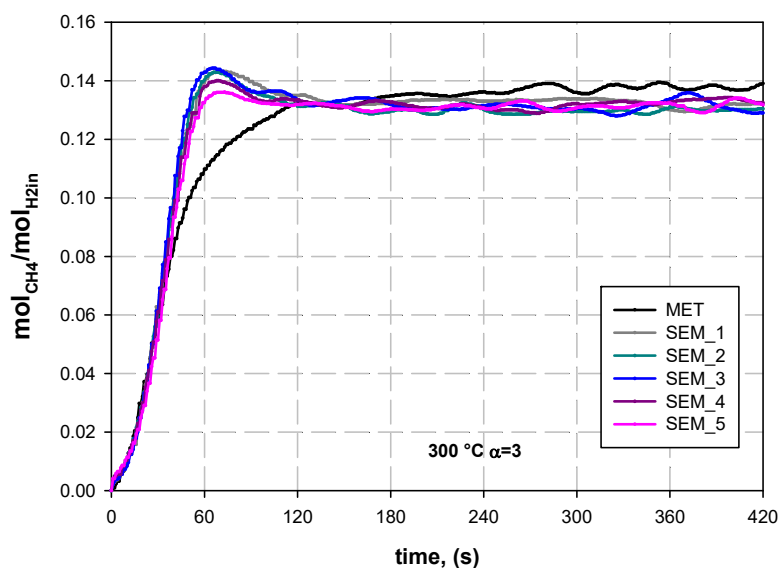


Figure 7. 19 Mole flow ratio between outlet CH₄ and inlet H₂ as a function of time at 300°C for zeolite 3A SEM. Catalyst mass = 70g.

$n\text{CH}_{4\text{out}}/n\text{H}_{2\text{in}}$											
MET		SEM_1		SEM_2		SEM_3		SEM_4		SEM_5	
t75	t180	t75	t180	t75	t180	t75	t180	t75	t180	t75	t180
0.0655	0.1028	0.0779 (18.8%)	0.1113 (8.3%)	0.0787 (20.1%)	0.1104 (7.4%)	0.08 (22.2%)	0.112 (8.9%)	0.0765 (16.8%)	0.1097 (6.7%)	0.0784 (14.4%)	0.1096 (5.2%)

Table 7.3 Ratio of cumulative CH₄ produced to H₂ fed (mol/mol) in each cycle at 300°C, and relative percentage variation with respect to standard methanation (MET).

8 Conclusions

In this work, the CO₂ sorption-enhanced methanation in interconnected fluidized bed reactors was studied from different perspectives and compared to traditional methanation. The investigations involved:

- the study of thermodynamics under sorption-enhanced conditions;
- AspenPlus simulations of the fluidized bed chemical looping process in which methanation and adsorption simultaneously occur in one reactor interconnected to a second fluidized bed where the regeneration of the sorbent takes place;
- the experimental evaluation of the steam capture capacity of different sorbent materials selected to perform SEM;
- a preliminary experimental testing of CO₂ SEM.

In the thermodynamic analysis, equilibrium compositions were calculated applying the Gibbs free energy minimization technique using a MATLAB code for two pressure levels (1-10 atm) and a range of temperatures from 200 to 600 °C. All the possible different SEM conditions were simulated introducing a water removal factor ranging from 0 (traditional methanation case) to 1 (SEM case where all the water is removed). Carbon deposition was verified: the calculations showed that if a stoichiometric feed is employed ($H_2/CO_2 = 4$), only partial steam capture can be performed to avoid carbon formation. At each temperature and pressure, the optimal H₂O removal fraction, which maximizes performance, was computed: it ranged from 28% to 94% of the maximum amount of H₂O that theoretically could be produced. This result also led to conclude that a dual fluidized bed system, unlike a fixed bed reactor, may guarantee flexible steady operation with partial H₂O removal, by varying the sorbent circulation rate or the ratio sorbent/catalyst in the system. SEM conditions do not affect appreciably CO concentrations whereas they can extend the range for acceptable outlet CO₂ for the injection in the natural gas grid: at 1 atm, for example, the limit specification can be fulfilled up to 310 °C. Unlike CO and CO₂, the H₂ limit resulted to be respected only at 10 atm but considering a temperature below 290 °C, which is hardly applicable due to catalytic constraints. The critical issue of the outlet gas purity was further examined with the AspenPlus software simulations. In this work, the chemical looping process was modeled considering the main reaction kinetics involved in the process and also the effect of one of the selected sorbents, CaO, on the chemical equilibrium. The Aspen “FluidBed” blocks simulated the methanator in a range of temperature from 250 °C to 350 °C and the regenerator, in which the continuous sorbent dehydration takes place, at 450 °C, in a plant at atmospheric pressure. The analysis was carried out varying parameters that characterize the gas and the solid sorbent feeds. In particular, two parameters were introduced:

- a parameter α indicating the gaseous supply in terms of H₂ and CO₂: for an $\alpha = 3$ the gaseous inlet reactants are in a stoichiometric ratio for methanation; for $\alpha < 3$ there is a sub-stoichiometric H₂ feeding;
- a parameter θ related to the amount of CaO fed to the methanation process with respect to the stoichiometric amount required for a total removal of the steam generated by the methanation reactions.

For a stoichiometric gas feed ratio ($H_2/CO_2 = 4$), the calculations pointed out that introducing CaO worsens the performance with respect to traditional methanation, highlighting the strong negative

effect of the undesired CaO carbonation reaction. Moreover, the CaO supply drastically increased the unconverted H₂ at the outlet, which was always far beyond the allowed limits for the injection in the grid. The analysis for a sub-stoichiometric gas feed ($H_2/CO_2 < 4$) identified an optimal condition in terms of CaO feeding ($\alpha=2$ and $\theta \geq 1.25$) under which the outlet stream met the network specifications. However, under these conditions, thermodynamic results pointed out the possible carbon formation, which is, thus, required to be confirmed by further experimental tests involving the real system conditions, such as the presence of CaO and related products.

The first experimental campaign of the work included the evaluation of the calcium oxide and commercial zeolites hydration/dehydration capacity under different operating conditions compatible with the methanation reactions. Water retention occurs by different mechanisms in these materials: CaO, obtained from natural limestone, is able to react reversibly with H₂O to form Ca(OH)₂. The second sorbent tested, a 3A zeolite, was an attrition-resistant spherical zeolite, which is capable of physically adsorb/desorb H₂O: due to its pore size, this material should act as a molecular sieve, accepting, for example, water but preventing the adsorption of larger molecules such as CO₂.

The tests consisted of 10 complete cycles of hydration/dehydration; the temperature range studied for hydration was 200-300°C, while that for dehydration was 350-450°C. Experiments were carried out in a system (Twin Beds), consisting of two identical laboratory-scale fluidized beds that can operate separately in batch mode as hydrator and dehydrator, specifically designed to study looping processes. Tests were conducted in 10% steam (balance air; low-CO₂ tests) and, to evaluate the effect of carbon dioxide, in streams with steam and CO₂, both at 10% (high-CO₂ tests). In low-CO₂ tests, CaO showed a capture of H₂O in a range of values between 0.01 and 0.14 $\frac{g(\text{Captured H}_2\text{O})}{g(\text{Initial Sorbent})}$, with the maximum value between the second and third cycle and a lower asymptotic value, reached around the sixth cycle. The decay with the number of cycles was caused by both the deactivation due to the irreversible CaO carbonation with CO₂ contained in the air and the attrition phenomena with possible elutriation of fines. Zeolites maintained a quite stable trend, with an asymptotic capture capacity (0.017-0.049 g/g) higher than CaO (0.006-0.025 g/g) and not being affected by deactivation during the cycles. Moreover, another important factor is the attrition resistance of the sorbent in a fluidized bed environment. However, these are not the only considerations to make for the choice of the best sorbent because, for example, the cost of the sorbent is in favor of CaO since zeolites can be even 100 times more expensive than CaO. Considering the high-CO₂ tests, calcium oxide showed a much lower capture capacity especially in the early stages: in fact, the value in the last cycle was comparable with that of the tests in air. The effect of hydration temperature, in the range investigated of 200-300 °C, was negative for all the sorbents analyzed. In the case of CaO, in the presence of CO₂, high temperatures favor the carbonation reaction that causes the irreversible deactivation of the sorbent. As for zeolites, physical adsorption is, as well known, disadvantaged by an increase of temperature. On average, for calcium oxide, tests at higher dehydration temperatures corresponded to higher capture values, but the effect vanished with the cycles due to the sorbent carbonation. As for zeolites, on the other hand, the highest dehydration temperature investigated of 450 °C may likely generate a structural change in the sorbent that significantly worsens the capture capacity as the number of cycles increases. In addition to zeolite 3A, another commercial zeolite was considered, the 4A zeolite. By comparing the two zeolites, it was found that the 4A zeolite presented an average value of H₂O capture only slightly higher than that of the 3A zeolite. As for the CO₂ effect, the two zeolites showed the same steam capture capacity during the last cycles, though zeolite 3A should prevent CO₂ adsorption due to its pores size.

Before investigating SEM in the Twin Beds, a study of conventional methanation in the fluidized bed reactor was carried out in order to obtain a reference behavior. The tests involved a 10%_wt catalyst on alumina supports with diameter of 600 and 1000 μ m, prepared by dry impregnation according to procedures reported in the literature, varying their quantity from 10 to 100g and the working temperature from 250 to 450°C. For both particle diameters significant methane productivities were reached only above 50g of catalyst used, and the maximum values were found between 300 and 350 °C. Above 400°C, the selectivity to methane, which was around 90% up to 350 °C, strongly decreased due to unwanted reactions leading to a higher CO production. These results suggested to carry out SEM at the lowest possible temperatures, which also favor the sorption process.

The last experimental campaign involved the study of the CO₂ sorption-enhanced methanation process using CaO and commercial zeolite 3A as sorbents. As for the CaO, the performance was evaluated at two different temperatures compatible with both methanation and chemical sorption of H₂O, 300°C and 350°C. In this case, also two different feed ratios were investigated: a stoichiometric feed (H₂/CO₂=4) and an over-stoichiometric feed in terms of CO₂ (H₂/CO₂=3). The latter was considered to verify the possibility of counteracting the influence of the undesired CaO carbonation reaction on SEM, as already investigated in Aspen simulations. The amount of methane with respect to the H₂ fed, was measured during 5 SEM cycles and compared to traditional methanation: the effect of the fresh CaO fed to the system was dramatic during the first SEM cycle, leading to a significant decrease in the methane productivity if considering the conventional case. When CO₂ was fed in excess with respect to the stoichiometric value, this negative effect seemed to be partly compensated. As the carbonation contribution decreased along the cycles, a clear enhancement of the methane productivity was observed from the second SEM cycle. This enhancement, with respect to traditional methanation, was around 20-30% and 8-10% at 300°C and 350°C, respectively, if considering the time within the sorbent saturation. The highest increase was found at the lowest temperature considered, 300°C, for both feed conditions: the stoichiometric gas feed ratio provided the best performance with the average increase of around 30%. The same performance parameters were evaluated using the zeolite 3A. For this sorbent the tests were performed at a fixed temperature of 300 °C, the maximum compatible with the sorption process. In addition, only stoichiometric feeding was investigated, since no carbonation occurs with the zeolite. During the SEM cycles methane production tended to rapidly reach a peak, occurring within the first 75s, during which the production increased of about 20% with respect to conventional methanation, and subsequently the curves approach the conventional methanation one with a stable trend. The lower quantitative enhancement effect of zeolites with respect to the CaO SEM at 300 °C, may be due to the effect of temperature on the zeolite physical adsorption, which is already disadvantaged at this temperature.

Overall, these preliminary results show a promising SEM effect when using water vapor sorbents, which however needs to be optimized in terms of operating conditions in future work. Particular attention should be paid to possible carbon formation since SEM operation might enhance such effect with respect to conventional methanation. There appears to be room for significant research on water vapor sorbents, with particular attention to bifunctional materials, i.e. particles combining both a methanation catalyst and a water vapor sorbent in their structure. Selectivity towards water vapor adsorption with respect to carbon dioxide appears to be a crucial aspect for such sorbents, which suggests that engineered zeolites might be preferable for the SEM technology.

References

- [1] NASA: Climate Change and Global Warming, <https://climate.nasa.gov>
- [2] Russo, A., “Confronto delle performance di tre sorbenti per la Sorption Enhanced Methanation in letti fluidizzati”, Master’s Degree Thesis (2019).
- [3] PBL Netherlands Environmental Assessment Agency 2020 report “*TRENDS IN GLOBAL CO₂ AND TOTAL GREENHOUSE GAS EMISSIONS*”
- [4] IEA, International Energy Agency, <https://www.iea.org/data-and-statistics/data-products>
- [5] Rönsch, S., Schneider, J., Matthischke, S., Schlüter, M., et al., “Review on methanation -From fundamentals to current projects”, *Fuel* 166: 276-296 (2016).
- [7] Sabatier, P., Senderens, J.-B., “New methane synthesis”, *J. Chem. Soc.* 82: 333-337 (1902).
- [8] Mills, G. A., Steffgen, F.W., “Catalytic methanation”, *Catal. Rev.* 8:159-210 (1974).
- [9] Bartholomew, C. H., “Mechanisms of catalyst deactivation”, *Appl. Catal. A* 212:17-60 (2001).
- [10] Seemann, M.C., Schildhauer, T.J., Biollaz, S.M.A., Stucki, S., Wokaun, A., “The regenerative effect of catalyst fluidization under methanation conditions”, *Appl. Catal. A* 313: 14–21 (2006).
- [11] Kopyscinski, J., Schildhauer, T.J., Biollaz, S.M.A., “Production of synthetic natural gas (SNG) from coal and dry biomass -a technology review from 1950 to 2009”, *Fuel*, 89:1763-1783 (2010).
- [12] Hashimoto, K., Yamasaki, M., Fujimura, K., Matsui, T., Izumiya, K., Komori, M., et al., “Global CO₂ recycling – novel materials and prospect for prevention of global warming and abundant energy supply”, *Mater Sci Eng A*, 267:200-6 (1999).
- [13] Van der Laan, G.P., Beenackers, A.A.C.M., “Kinetics and selectivity of Fischer-Tropsch synthesis: a literature review”, *Catal Rev – Sci Eng.* 41:255-318 (1999).
- [14] Saito, M., Anderson, R.B., “The activity of several molybdenum compounds for the methanation of CO”, *J. Catal.* 63:438-46 (1980).
- [15] Qin, H., Guo, C., Wu, Y., Zhang, J., “Effect of La₂O₃ promoter on NiO/Al₂O₃ catalyst in CO methanation”, *Korean J. Chem. Eng.* 31:1168-73 (2014).
- [16] Liu, Q., Gu, F., Lu, X., Liu, Y., Li, H., Zhong, Z., “Enhanced catalytic performances of Ni/Al₂O₃ catalyst via addition of V₂O₃ for CO methanation”, *Appl Catal A* 488:37-47 (2014).
- [17] Liu, H., Zou, X., Wang, X., Lu, X., Ding, W., “Effect of CeO₂ addition on Ni/Al₂O₃ catalysts for methanation of carbon dioxide with hydrogen”, *J Nat Gas Chem* 21:703-707 (2012).
- [18] Nguyen, T.T.M., Wissing, L., Skjøth-Rasmussen, M.S., “High temperature methanation: catalyst considerations”, *Catal Today* 215:233-238 (2013).
- [19] Van Herwijnen, T., Van Doesburg, H., De Jong, W. A., “Kinetics of the methanation of CO and CO₂ on a nickel catalyst”, *Journal of Catalysis* 28:391-402 (1973).
- [20] Araki, M., Ponec, V., “Methanation of carbon monoxide on nickel and nickel-copper alloys”, *J Catal* 44:439-48 (1976).
- [21] Weatherbee, G.D., Bartholomew, C.H., “Hydrogenation of CO₂ on group VIII metals: II. Kinetics and mechanism of CO₂ hydrogenation on nickel”, *J Catal* 77:460-472 (1982).
- [22] Xu, J., Froment, G.F., “Methane steam reforming, methanation and water-gas shift: 1.intrinsic kinetics”, *AIChE .J.* 35: 88-96 (1989).
- [23] Kopyscinski, J., “Production of synthetic natural gas in a fluidized bed reactor”, PhD Thesis, (2010).
- [24] Riedel, T., Schulz, H., Schaub, G., Jun, K. W., Hwang, J. S., Lee, K. W., “Fischer-Tropsch on iron with H₂/CO and H₂/CO₂ as synthesis gases: the episodes of formation of the Fischer-Tropsch regime and construction of the catalyst”, *Topics in Catalysis* 26: 41-54 (2003).
- [25] Kowalczyk, Z., Stołeccki, K., Rarog-Pilecka, W., Miskiewicz, E., Wilczkowska, E., Karpinski, Z., “Supported ruthenium catalysts for selective methanation of carbon oxides at very low CO_x/H₂ ratios”, *Applied Catalysis A: General* 342: 35-39 (2008).

- [26] Jacquemin, M., Beuls, A., Ruiz, P. “Catalytic production of methane from CO₂ and H₂ at low temperature: Insight on the reaction mechanism” *Catalysis Today* 157: 462-466 (2010).
- [27] Gao, J., Liu, Q., Gu, F., Liu, B., Zhong, Z., Su, F., “Recent advances in methanation catalysts for the production of synthetic natural gas”, *RSC Advances* 5: 22759-22776 (2015).
- [28] Frontera, P., Macario, A., Ferraro, M., Antonucci, P., “Supported Catalysts for CO₂ Methanation: A Review”, *Catalysts* 7 (2017).
- [29] Hubble, R.A., Lim J. Y., Dennis, J. S., “Kinetic studies of CO₂ methanation over a Ni/g-Al₂O₃ catalyst”, *Faraday Discuss.* 192: 529-544 (2016).
- [30] <https://www.dakotagas.com/about-us/index>
- [31] HaldorTopsoe, “Methanation catalyst PK-7R”, Technical report, Haldor Topsoe, (2008).
- [32] HaldorTopsoe, “From coal to substitute natural gas using TREMP”, Technical report, Haldor Topsoe, (2008).
- [33] Deurwaarder, E.P., Boerrigter, H., Mozaffarian, M., Rabou, L.P.L.M., Drift Avd. “Methanation of Milena product gas for the production of bio-SNG”, Technical report, ECN Report, 14th European biomass conference and exhibition, Paris, France (2005).
- [34] Seemann, M.C., “Methanation of biosyngas and simultaneous low-temperature reforming: First results of long duration test at the FICFB gasifier in Güssing”, Proceeding of the fourth european biomass conference and exhibition biomass for energy, industry and climate protection, Paris, France (2005).
- [35] Vaccaro, G.A., “CO₂ utilization from fermentation processes for the catalytic production of methane”, Master’s Degree Thesis (2020).
- [36] Castellani, B., Gambelli, A.M., Morini, E., Nastasi, B., Presciutti, A., Filipponi, M., Nicolini, A., Rossi, F., “Experimental Investigation on CO₂ Methanation Process for Solar Energy Storage Compared to CO₂-Based Methanol Synthesis”, *Energies* 10:855 (2017).
- [37] Biswas, S., Kulkarni, A.P., Giddey, S., Bhattacharya, S., “A Review on Synthesis of Methane as a Pathway for Renewable Energy Storage With a Focus on Solid Oxide Electrolytic Cell-Based Processes”, *Frontiers in Energy Research* 8:229 (2020).
- [38] Golling, C., Heuke, R., Seidl, H., Uhlig, J., “Roadmap power-to-gas”, Berlin (2017).
- [39] IEA (2021), *Global Energy Review 2021*, IEA, Paris
<https://www.iea.org/reports/global-energy-review-2021>
- [40] Thema, M., Bauer, F., Sterner, M., “Power-to-Gas: Electrolysis and methanation status review”, *Renewable and Sustainable Energy Reviews* 112: 775-787 (2019).
- [41] Thema, M., Sterner, M., Lenck, T., Götz, P., “Necessity and Impact of Power-to-gas on Energy Transition in Germany”, *Energy Procedia* 99: 392-400 (2016).
- [42] Om, K., Sathans, S., “An updated review of energy storage systems: classification and applications in distributed generation power systems incorporating renewable energy resources”, *International Journal of Energy Research* 43: 6171-6210 (2019).
- [43] Moore, J., Shabani, B., “A Critical Study of Stationary Energy Storage Polices in Australia in an International Context: The Role of Hydrogen and Battery Technologies”, *Energies* 9:674 (2016).
- [44] Buttler, A., Spliethoff, H., “Current status of water electrolysis for energy storage, grid balancing and sector coupling via power-to-gas and power-to-liquids: a review” *Renew Sustain Energy Rev* 82: 2440-2454 (2018).
- [45] <https://en.wikipedia.org/wiki/Energystorage>
- [46] Figueroa J.D., Fout, T., Plasynski, S., McIlvried, H., Srivastava R.D., “Advances in CO₂ capture technology” *The U.S. Department of Energy’s Carbon Sequestration Program* (2008).
- [47] Padurean, A., Cormos, C.C., Agachi, P.S., “Pre-combustion carbon dioxide capture by gas-liquid absorption for Integrated Gasification Combined Cycle power plants”, *International Journal of Greenhouse Gas Control* 7: 1-11 (2012).

- [48] Karimi, M., Hillestad, M., Svendsen, H.F., “Capital costs and energy considerations of different alternative stripper configurations for post combustion CO₂ capture”, *Chem Eng Res Des* 89: 1229-1236 (2011).
- [49] Bui, M., Adjiman, C.S., Bardow, A., Anthony, E.J., Boston, A., Brown, ., Fennell, P.S., Fuss, S., Galindo, A., Hackett, L.A., Hallett, J.P., Herzog, H.J., Jackson, G., Kemper, J., Krevor, S., Maitland, G.C., Matuszewski, M., Metcalfe, I.S., Petit, C., Puxty, G., Reimer, J., Reiner, D.M., Rubin, E.S., Scott, S.A., Shah, N., Smit, B., Trusler, J. P. M., Webley, P., Wilcox, J., Mac Dowell, N., “Carbon capture and storage (CCS): the way forward”, *Energy Environ. Sci.* 11: 1062:1176 (2018).
- [50] MacKenzie, A., Granatstein, D.L., Anthony, E.J., Abanades, J.C., “Economics of CO₂ capture using the calcium cycle with a pressurized fluidized bed combustor”, *Energy & Fuels* 21: 920-926 (2007).
- [51] Coppola, A., Scala, F., Salatino, P., Montagnaro, F., “Fluidized bed calcium looping cycles for CO₂ capture under oxy-firing calcination conditions: Part 1. Assessment of six limestones.”, *Chemical Engineering Journal* 231:537-543 (2013).
- [52] Dean, C.C., Dugwell, D., Fennell, P.S., “Investigation into potential synergy between power generation, cement manufacture and CO abatement using the calcium looping cycle”, *Energy & Environmental Science* 4: 2050-2053 (2011).
- [53] Coppola A., Salatino P., Montagnaro F., Scala F., “Reactivation by Water Hydration of the CO₂ Capture Capacity of a Calcium Looping Sorbent”, *Fuel* 127: 109-115 (2014).
- [54] <https://www.linde-engineering.com/en/process-plants/co2-plants/carboncapture/oxyfuel>
- [55] Leung, D.Y.C., Caramanna G., Maroto-Valer, M., “An overview of current status of carbon dioxide capture and storage technologies”, *Renewable and Sustainable Energy Reviews* 39: 426-443 (2014).
- [56] Metz B., Davidson O., de Coninck H., Loos M., Meyer L., “IPCC Special Report on Carbon Dioxide Capture and Storage”, Intergovernmental Panel on Climate Change (2005).
- [57] <https://www.researchgate.net/figure/Options-for-the-geological-storage-of-carbon-dioxide>
- [58] <https://www.netl.doe.gov/coal/carbon-storage/advanced-storage-r-d>
- [59] Shiva Kumar, S., Himabindu, V., “Hydrogen production by PEM water electrolysis – A review”, *Materials Science for Energy Technologies* 2: 442-454 (2019).
- [60] Götz, M., Lefebvre, J., Mörs, F., Koch, A., Graf, F., Bajohr, S., Reimert, R., Kolb, T., “Renewable Power-to-Gas: A technological and economic review”, *Renewable Energy* 85: 1371-1390 (2016).
- [61] Luo, M., Yang Yi, Y., Wang, S., Wang, Z., Du, M., Pan, J., Wang, Q., “Review of hydrogen production using chemical-looping technology”, *Renewable and Sustainable Energy Reviews* 81: 3186-3214 (2018).
- [62] Carvill, B.T., Hufton, J.R., Anand, M., Sircar, S., “Sorption-enhanced reaction process” *AIChE J.*, 42: 2765-2772 (1996).
- [63] Borgschulte, A., Gallandat, N., Probst, B., Suter, R., Callini, E., Ferri, D., Arroyo, Y., Erni, R., Geerlings, H., Züttel, A., “Sorption enhanced CO₂ methanation”, *Phys. Chem. Chem. Phys.* 15: 9620-9625 (2013).
- [64] Walspurger, S., Elzinga, G.D., Dijkstra, J.W., Saric, M., Haije, W.G., “Sorption enhanced methanation for substitute natural gas production: Experimental results and thermodynamic considerations”, *Chem. Eng. J.* 242: 379-386 (2014).
- [65] Delmelle, R., Duarte, R.B., Franken, T., Burnat, D., Holzer, L., Borgschulte, A., Heel, A., “Development of improved nickel catalysts for sorption enhanced CO₂ methanation”, *International Journal of Hydrogen Energy* 41: 20185-20191 (2016).
- [66] Delmelle, R., Terreni, J., Remhof, A., Heel, A., Proost, J., Borgschulte, A., “Evolution of Water Diffusion in a Sorption-Enhanced Methanation Catalyst”, *Catalysts* 8:341 (2018).

- [67] Agirre, I., Acha, E., Cambra, J.F., Barrio, V.L., “Water sorption enhanced CO₂ methanation process: Optimization of reaction conditions and study of various sorbents”, *Chemical Engineering Science* 237 (2021).
- [68] Wei, L., Azad, H., Haije, W., Grenman, H., de Jong, W., “Pure methane from CO₂ hydrogenation using a sorption enhanced process with catalyst/zeolite bifunctional materials”, *Applied Catalysis B: Environmental* 297 (2021).
- [69] Gao, J., Wang, Y., Ping, Y., Hu, D., Xu, G., Gu, F., et al., “A thermodynamic analysis of methanation reactions of carbon oxides for the production of synthetic natural gas”, *RSC Adv.* 2: 2358-68 (2012).
- [70] Silveira, J.L. (Ed.), “Sustainable Hydrogen Production Processes”, Springer Cham (2017).
- [71] Cairns, E.J., Tevebaugh, A.D., “CHO gas phase compositions in equilibrium with carbon, and carbon deposition boundaries at one atmosphere”, *J. Chem. Eng. Data* 9: 453-462 (1964).
- [72] Koytsoumpa, E.I., Karellas, S., “Equilibrium and kinetic aspects for catalytic methanation focusing on CO₂ derived Substitute Natural Gas (SNG)”, *Renew. Sust. Energy Rev.* 94: 536-550 (2018).
- [73] Catarina Faria, A., Miguel, C.V., Madeira, L.M., “Thermodynamic analysis of the CO₂ methanation reaction with in situ water removal for biogas upgrading”, *J. CO₂ Util.* 26: 271-280 (2018).
- [74] Swapnesh, A., Srivastava, V.C., Mall, I.D., “Comparative study on thermodynamic analysis of CO₂ utilization reactions”, *Chem. Eng. Technol.* 37: 1765-1777 (2014).
- [75] Werther, J., “Fluidized-bed reactors”, *Ullmann's encyclopedia of industrial chemistry*, (2000).
- [76] Kunii, D., Levenspiel, O., “Fluidization engineering”, Butterworth-Heinemann (1991).
- [77] Yang, W., “Handbook of Fluidization and Fluid-Particle Systems”, *CRC press* (2003).
- [78] Schaube, F., Koch, L., Wörner, A., Müller-Steinhagen, H., “A thermodynamic and kinetic study of the de- and rehydration of Ca(OH)₂ at high H₂O partial pressures for thermo-chemical heat storage”, *Thermochimica Acta*, 538: 9-20 (2012).
- [79] Li, Z., “General rate equation theory for gas–solid reaction kinetics and its application to CaO carbonation”, *Chemical Engineering Science*, 227: 115902 (2020).
- [80] Hervy, M., Maistrello, J., Brito, L., Rizand, M., Basset, E., Kara, Y., Maheut, M., “Power-to-gas: CO₂ methanation in a catalytic fluidized bed reactor at demonstration scale, experimental results and simulation”, *Journal of CO₂ Utilization* 50 (2021).
- [81] Gardner, D.C., Bartholomew, C.H., “Kinetics of Carbon Deposition During Methanation of CO”, *Industrial & Engineering Chemistry Product Research and Development* 20:80–87 (1981).
- [82] <https://www.chimica-online.it/materiali/zeoliti.htm>
- [83] Lechkar, A., Barroso Bogeat, A., Blanco, G., Pintado, J.M., Soussi el Begrani, M., “Methanation of carbon dioxide over ceria-praseodymia promoted Ni-alumina catalysts. Influence of metal loading, promoter composition and alumina modifier”, *Fuel* 234: 1401-1413 (2018).
- [84] Rahmani, S., Rezaei, M., Meshkani, F., “Preparation of promoted nickel catalysts supported on mesoporous nanocrystalline gamma alumina for carbon dioxide methanation reaction”, *Journal of Industrial and Engineering Chemistry* 20: 4176-4182 (2014).
- [85] Abate, S., Mebrahtu, C., Giglio, E., Deorsola, F., Bensaid, S., Perathoner, S., Pirone, R., Centi, G., “Catalytic Performance of γ -Al₂O₃–ZrO₂–TiO₂–CeO₂ Composite Oxide Supported Ni-Based Catalysts for CO₂ Methanation”, *Industrial & Engineering Chemistry Research* 55: 4451-4460 (2016).

- [86] Coppola, A., Scala, F., Gargiulo, L., Salatino, P., “A twin-bed test reactor for characterization of calcium looping sorbents”, *Powder Technology* 316: 585-591 (2017).
- [87] Scala, F., Cammarota, A., Chirone, R., Salatino, P., “Comminution of limestone during batch fluidized-bed calcination and sulfation”, *AIChE Journal* 43:363-373 (1997).
- [88] Coppola, A., Palladino, L., Montagnaro, F., Scala, F., Salatino, P., “Reactivation by steam hydration of sorbents for fluidized-bed calcium looping”, *Energy Fuel* 29:4436–4446 (2015).
- [89] Jia, C., Dai, Y., Yang, Y., Chew, J.W., “Nickel-cobalt catalyst supported on TiO₂-coated SiO₂ spheres for CO₂ methanation in a fluidized bed”, *International Journal of Hydrogen Energy* 44:13443-13455 (2019).